6-29-2021

A Study of Magnetism and Possible Mixed-State Superconductivity in Phosphorus-Doped Graphene

Julian E. Gil Pinzon
Florida International University, jgil044@fiu.edu

FLORIDA INTERNATIONAL UNIVERSITY

Miami, Florida

A STUDY OF MAGNETISM AND POSSIBLE MIXED-STATE SUPERCONDUCTIVITY IN PHOSPHORUS-DOPED GRAPHENE

A dissertation submitted in partial fulfillment of

the requirements for the degree of

DOCTOR OF PHILOSOPHY

in

ELECTRICAL AND COMPUTER ENGINEERING

by

Julian Esteban Gil Pinzon

2021

To: Dean John L. Volakis
College of Engineering and Computing

This dissertation, written by Julian Esteban Gil Pinzon, and entitled A Study of Magnetism and Possible Mixed-State Superconductivity in Phosphorus-Doped Graphene, having been approved in respect to style and intellectual content, is referred to you for judgment.

We have read this dissertation and recommend that it be approved.

_____
Jean H. Andrian

_____
Yuriy Vlasov

_____
Nezih Pala

_____
Pete E. Markowitz

_____
Grover L. Larkins, Major Professor

Date of Defense: June 29, 2021

The dissertation of Julian Esteban Gil Pinzon is approved.

_____
Dean John L. Volakis
College of Engineering and Computing

_____
Andrés G. Gil
Vice President for Research and Economic Development
and Dean of the University Graduate School

Florida International University, 2021

ABSTRACT OF THE DISSERTATION

A STUDY OF MAGNETISM AND POSSIBLE MIXED-STATE SUPERCONDUCTIVITY IN PHOSPHORUS-DOPED GRAPHENE

by

Julian Esteban Gil Pinzon

Florida International University, 2021

Miami, Florida

Professor Grover L. Larkins, Major Professor

Evidence of superconducting vortices, and consequently mixed-state superconductivity, has been observed in phosphorus-doped graphene at temperatures as high as 260 K. The evidence includes transport measurements in the form of resistance versus temperature curves, and magnetic measurements in the form of susceptibility and magnetic Nernst effect measurements. The drops in resistance, periodic steps in resistance, the appearance of Nernst peaks and hysteresis all point to phosphorus-doped graphene having a broad resistive region due to flux flow as well as a Berezinskii-Kosterlitz-Thouless (BKT) transition at lower temperatures.

The observation of irreversible behavior in phosphorus-doped graphene under the influence of a thermal gradient and an orthogonal applied magnetic field is a direct sign of mixed-state superconductivity, as it demonstrates the presence of vortices. The observations are based on cyclic Nernst measurements that show clear hysteresis that diminishes as the sample is warmed to temperatures higher than 200 K; voltage steps and anomalous structures related to field screening are observed at temperatures below 70 K;

and finally, smaller Nernst peaks are seen at temperatures near 230 K pointing to vortex stacks having high depinning and thermal energies.

TABLE OF CONTENTS

CHAPTER PAGE

LIST OF FIGURES

FIGURE PAGE

I. INTRODUCTION

Since the discovery of superconductivity, the search for practical high-temperature superconductors has been of significant importance to research for engineering and industrial purposes. The use of high-temperature practical superconductors would have a significant impact in the electronics industry as it can replace current devices and practices, or potentially be the beginning of a new generation of electronic devices.

One of the many issues that this search faces is the fragility of the superconductive state. Ever since the first superconductors were experimented on, it was found that low current densities and magnetic fields quenched superconductivity and reverted the material to its normal state. As research progressed, high-temperature superconductors have been found, though their complex structures and preparations hinder their use in industrial applications. Several newer materials require high amounts of pressure, or complicated, and often dangerous, fabrication procedures. As a result, a material with a simple enough structure, preparation, and high transition temperature is required.

Carbon is an element with a large number of allotropes with relatively simple or well-understood structures. Most carbon allotropes can become superconductors; however, their critical temperatures are low. Carbon has a low electron density which does not allow for a high probability of pairing. As a result, doping and the injection of carriers can potentially solve the problem of low critical temperatures. This work aims to study the possibility of superconductivity, with focus on the mixed state region, in phosphorus-doped graphene.

A. Problem statement

The mixed state of high-temperature superconductors is characterized by the appearance of flux quanta or vortices. Most high-temperature superconductors are layered or two-dimensional materials that have strong anisotropy. The anisotropy and two-dimensional nature of such materials contributes to a broad resistive region below the critical temperature and between the two critical applied magnetic fields H_{c1} and H_{c2}. This resistive region is a result of the interactions between the vortices, carriers, applied currents and/or thermal gradients. The mechanism of superconductivity in low dimensional materials is also affected by the Berezinskii-Kosterlitz-Thouless (BKT) transition, where below a threshold temperature known as the BKT temperature, the vortices and antivortices present in the material are effectively bound to each other causing freezing or the formation of a vortex lattice that reduces the resistivity of the material due to the vortex interactions. This leads the way to a transition to the full Meissner state, where the magnetic field is expelled from the material. In addition to the binding of vortex pairs in the BKT transition, pinning is an important effect in the mixed state due to the reduction in resistivity and the creation of vortex stacks that melt at much higher temperatures than the BKT temperature.

The mixed state is a transition to a region where irreversibility and hysteresis are known to appear. In the case of doped graphene, it is expected that the high electron correlation, doping, high Debye temperature, high anisotropy among other properties, would give rise to mixed-state superconductivity. As a result, Nernst peaks and hysteresis loops are expected to be observed in the material in a standard magnetic Nernst effect measurement setup.

B. Hypotheses:

- A major tilted hill-shaped peak is expected to appear in the measurements, as there is an imbalance of vortices, and core quasiparticles, in the sample due to the cross product between the applied thermal gradient and applied magnetic field.
- Smaller tilted-hill peaks are observed at higher temperature due to the high anisotropy and pinning in the graphene samples. The anisotropy and pinning sites allow vortex stacking and different melting temperatures for different stacks of vortices.
- As the phosphorus-doped graphene sample is cyclically cooled and warmed, the hysteresis loops become smaller as flux is being expelled and the imbalance of vortices becomes smaller.
- Donor-doped graphene is a high-temperature superconductor as mixed state superconductivity occurs at temperature in excess of 200 K.

II. PROPERTIES OF GRAPHENE

A. Structure and Mechanical Properties

Carbon is an element with six electrons, four of which are valence electrons. The valence electrons in carbon are responsible for bonding. When forming its different allotropes, carbon promotes one 2s electron to the $2p_z$ orbital to hybridize the orbitals. Graphite, a carbon allotrope, has sp^2 hybridization orbitals with three sp^2 orbitals forming an in-plane structure separated at a 120-degree angle, while the remaining orbital is out of plane. The in-plane bonds that make up the structure are called σ-bonds, while a π-bond is directed to the c-direction, or the direction that is perpendicular to the plane. The π-bonds are symmetric lobes along the c-direction forming π and π^* bands, which are mostly responsible for the electronic properties of graphene. The π bands originate from the overlap of $2p_z$ orbital from adjacent atoms. The overlapping orbitals are perpendicular to the in-plane orbitals, or the 2s, $2p_x$ and $2p_y$ orbitals. The latter orbitals are known as the valence orbitals. The in-plane bonding energy in graphite is 615 kJ mol^{-1}, making graphite an extremely strong material.

Graphene is defined as the quasi-two-dimensional isolated layer of carbon [1]. In 2004, a group from Manchester University directed by Andre Geim first isolated this carbon allotrope. Graphene was generated via mechanical exfoliation from its bulk counterpart, graphite [2]. In graphene, carbon forms a hexagonal lattice where each carbon atom is at a= 0.142 nm from its neighbor. The lattice itself can also be seen as two triangular lattices layered in an alternating composition labeled A and B, as in figure 1.

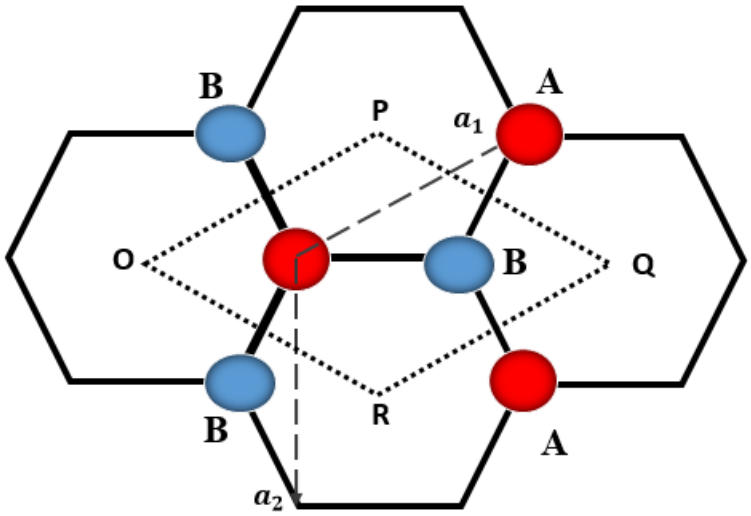

Figure 1 The graphene lattice is composed of hexagonal bonds. The area OPQR depicts the unit cell enclosing the two triangular lattices with vertices A and B, respectively. $\boldsymbol{a_1}$ and $\boldsymbol{a_2}$ are the translation vectors.

The section OPQR of the lattice enclosing atoms A and B, as well as the branches opening at 120 degrees on either side, is the unit cell of graphene with translation vectors $\boldsymbol{a_1}$ and $\boldsymbol{a_2}$. The lattice in reciprocal space of graphene is shown in figure 2 with its corresponding translation vectors. The reciprocal lattice is perpendicular to its counterpart in real space. From the translation vectors of the reciprocal lattice, it follows that its first Brillouin zone is a hexagon.

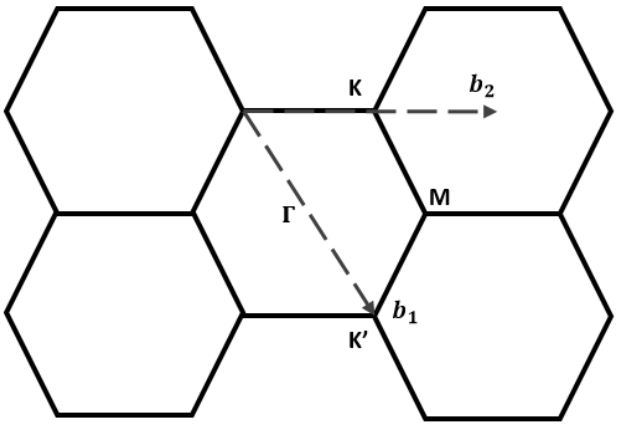

Figure 2 Reciprocal lattice of graphene. Γ is the zero momentum region while K and K' are the Dirac points. The reciprocal vectors are represented by b_1 and b_2.

Graphene can be classified based on the number of layers that compose a specific sample. Monolayer and bilayer graphene are zero-bandgap semiconductors, as their conduction and valence bands make contact at the Dirac points. Graphene specimens ranging from 3 to 10 monolayers are known as multilayer or few-layer graphene, while specimens with higher number of layers are simply graphite thin films. The successful isolation of graphene monolayers had been considered to be impossible as long-range order in two-dimensional crystals is limited by thermal fluctuations. Thermal fluctuations are known to affect long-range coherence and, as a result, melt the crystal. The stability of graphene, a purely two-dimensional crystal, is due to corrugations or out-of-plane ripples that are present in the material. A number of electron diffraction (ED) studies [3] have shown the presence of these ripples in graphene. The ripples are approximately 1 nm in size perpendicular to the plane, and between 5 nm to 20 nm laterally. Both the structure and the out-of-plane distortions in graphene are important contributing factors in its superior strength.

The strength of a material is often found by testing the how much stress σ_{st} can the material withstand without breaking. The engineering stress, denoted by σ_{st}, is the force per unit

area applied to the material. As a result, it has units of Newtons per meter per meter or N/m^2. Stress can be tensile stress, wherein the force is applied perpendicular to cross-sectional area of the material, or shear stress where the forces are applied parallel to the area of the material in a shear fashion. The two types of stress are shown in figure 3.

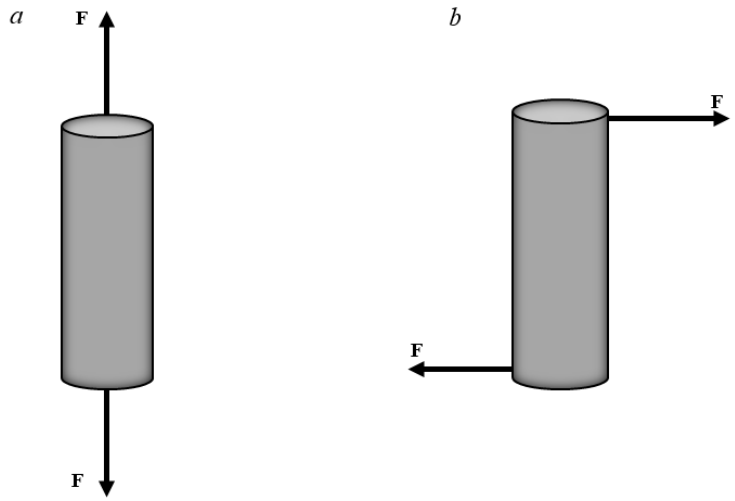

Figure 3 a) Tensile stress, b) Shear stress

Another important quantity that relates to the mechanical properties of a material is the unitless quantity called engineering strain ϵ_{st}. It is defined as the normalized length difference caused by an applied stress. The strain versus stress plot is a useful tool used to determine the different regions that a material can fall into when stress is applied. A generic strain versus stress diagram is shown in figure 4. The ratio of the stress-to-strain represents the slope of the line in the elastic region; the ratio is known as young's modulus E_{yn}, and the equivalency is often known as Hooke's law.

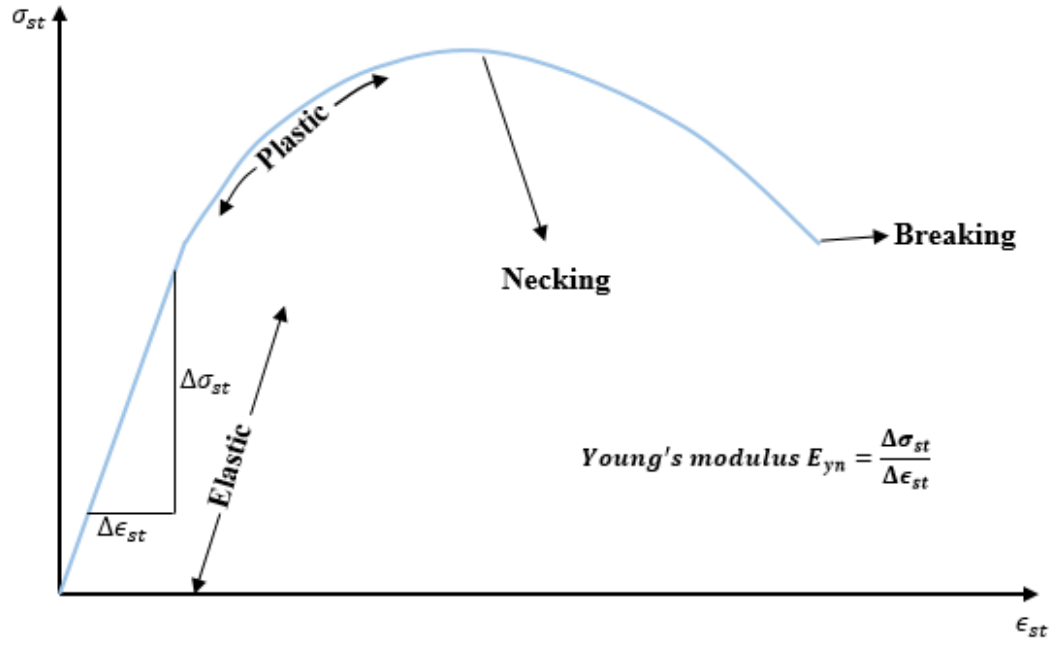

Figure 4 Engineering stress versus strain diagram showing the elastic region, the plastic region, the point where "necking" begins, and finally the breaking point of the material.

There are many tests used to determine mechanical quantities in different materials; however, the atomic force microscope (AFM) is a standard tool used in materials at the nanoscale and, as such, in carbon nanostructures like graphene. Carbon-carbon bonds, sp^2 hybrids, are one of the strongest known bonds in existence. For that reason, graphene was, early on, expected to be a very strong material. Due to the difficulty of fabricating thin layers of graphite as well as the uncertainty of the geometry, no exact measurements on the strength of graphene were done before 2007. Nevertheless, theoretical calculations suggesting that it was a very strong material were made in 1999 and 2000 [4,5]. The first concrete experimental measurement regarding the strength of graphene came in 2007 [6]. A notion of the force graphene can withstand comes from the effective spring constant of the material k_{sp}. The spring constant is approximated by:

$$k_{sp} = 16.230E_{yn}(width)\left(\frac{thickness}{Length}\right)^3 + 4.93\left(\frac{tension}{Lenght}\right)$$

Where graphene and the probe used are accounted for using Young's modulus, the tension and length of deflection. The setup in figure 5 shows, schematically, the experiment used to determine the spring constant of graphene, which amounted to 1 to 5 N/m in graphene sheets of thicknesses ranging from 2 to 8 nm.

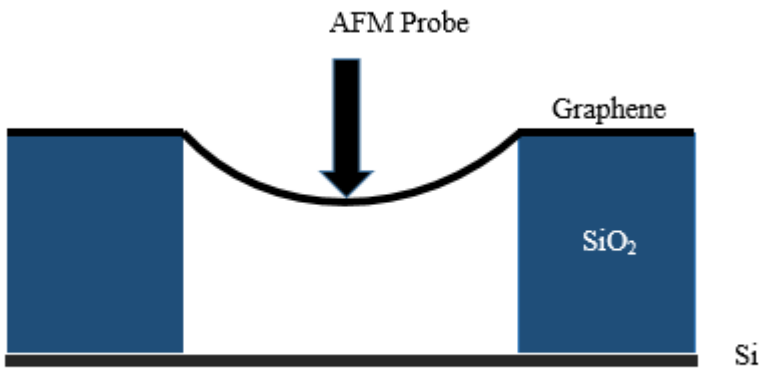

Figure 5 Setup used to approximate the spring constant of graphene by measuring the deflection of the AFM probe.

In 2008, the work done by Lee [7] provided the community with more accurate measurements. The breaking strain came at 25% of graphene's length, almost in agreement with 20% calculated in prior works [8,9]. The intrinsic tensile strength of graphene was found to be 130 GPa; this is the highest value in any known material. Young's modulus was found to be 1 terapascal (TPa). The discrepancies between the theoretical and experimental values are often attributed to defects, specifically vacancies, as the defects in the lattice affect the way the stress is carried.

In addition to the in-plane bonds, which make graphene strong, there is a significant contribution of the Van der Waals forces (VDW) in adhesion. Van Der Waals bonds arise

due to a slight polarization in atoms causing the charges to be attracted to the opposite charge of the neighboring atoms. In general, Van Der Waals interactions are very weak; however, they become significant at the nanoscale. In the case of graphene, the Van Der Waals interaction is responsible for the adhesion perpendicular to the plane or, in other words, the interlayer adhesion. The sample's roughness is proportional to the strength of the VDW interaction as there is more contact with the adjacent layer. The adhesion energy in graphene was found to be 0.45 J/m^2 for single layer graphene and 0.31 J/m^2 [10] for multilayer graphene. The high adhesion energy of graphene causes its flexibility, as it allows graphene to be a pliable material that can mold to take the shape of the substrate's surface.

B. Electronic Properties

Although many of the most important and unique properties of graphene come from its physical lattice structure and layer number, its dispersion relation is directly involved in how electrons conduct in graphene. The dispersion relation, or *E* versus *k* relation, can be described with a tight-binding approach and assuming a single π electron per atom [11] by:

$$E(k_x, k_y) = \mp t\sqrt{3 + \gamma(k_x, k_y)} - 0.2t\gamma(k_x, k_y)$$

Where $\gamma(kx, ky) = 2\cos(\sqrt{3}k_y a) + 4\cos\left(\frac{\sqrt{3}}{2}k_y a\right)\cos\left(\frac{3}{2}k_x a\right)$

The dispersion equation produces the electronic band structure seen in figure 6. From the band structure, some key points about the electronic properties of graphene can be observed.

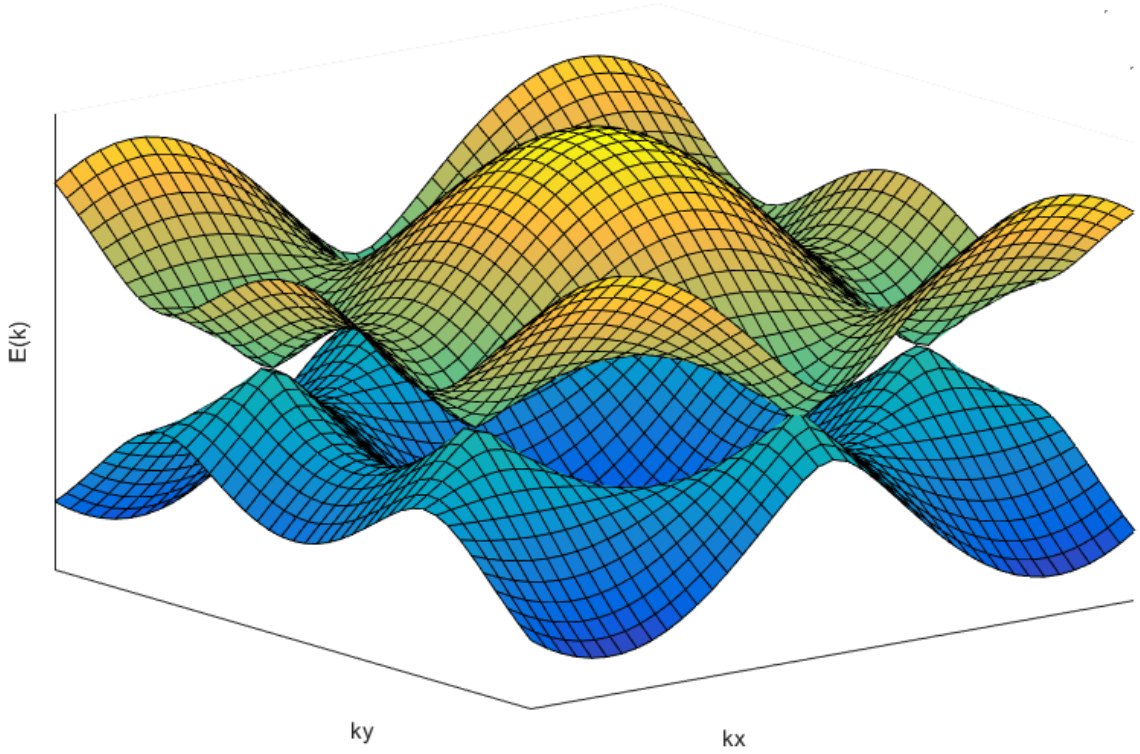

Figure 6 Energy versus momentum relation

First, the density of states (DOS) at the points of contact of conduction and valence band, or Dirac points, is zero. As a result, graphene is effectively a zero-band gap semiconductor material.

The Dirac points are grouped in two sets labeled K_D and $K_D{}'$ containing three points per group. Near the Dirac points the energy versus momentum relation becomes linear, which is one of the main reasons why graphene has such interesting electronic properties. A linear relation implies Fermions and quasiparticles having zero effective mass due to their relativistic nature. The energy versus momentum relation for the Dirac electrons can be approximated by:

$$E(k) \sim \frac{h}{2\pi} v_F |k - K_D|$$

where v_F is the Fermi velocity, here approximately equal to 10^6 m/s. These Fermions and massless quasiparticles are found within 1 eV of the Dirac energy.

Since the valence and conduction bands meet at the Dirac points, the energy at this region is often called the Dirac energy, which, in the case of graphene, coincides with the Fermi energy. However, in non-ideal graphene, such as in graphene-based devices, the Fermi and Dirac energies generally do not correspond with each other.

Second, the energy versus momentum relation of graphene is chiral. The chirality of graphene's dispersion relation also results in important transport properties such as Klein tunneling [12-15]. Chirality in graphene occurs in the individual branches of the energy versus momentum relation. Roughly, every triangular sub lattice in graphene corresponds to a branch in the curve. These branches have a very weak interaction with one another. The dispersion relation can shed light on two important transport phenomena in graphene.

The first property is the ambipolar field effect; this effect concerns the tuning of carriers in graphene by an applied gate voltage. The application of a gate voltage through a doped substrate can tune the Fermi level of the graphene sheet and, as a result, the carrier type and density. The closer the position of the Fermi level to the Dirac points the less carriers are available. In other words, a Fermi level above the Dirac point indicates majority electron carrier, while below the Dirac point indicates majority hole presence.

In the general sense, ambipolar transport refers to the drift of both excess electrons and excess holes in the presence of an electric field. In order to keep charge neutrality, the flux of excess carriers drift together in the direction of the applied field. However, in the case of graphene the ambipolar effect has to do with the application of a gate voltage to either raise the Fermi level to the conduction band or to lower it to the valence band; thus,

effectively changing the majority carrier. Unlike graphene, bandgap semiconductors in the presence of an electric field have a cycle of generation and recombination of carriers that are measured through the carrier lifetime τ_{lt}. In graphene such recombination rates are in the order of 10^{15} s^{-1} corresponding to a lifetime τ_{lt} of 1 fs [16]. The pronounced electro-hole effects result in strong Coulomb interactions from electrons seeking recombination. Such effects combined with the bonding strength are signs of strong electronic correlation is graphene that also result in a long electronic mean-free path.

Another signature property of strongly correlated materials is the measurement of the quantum Hall effect (QHE). The quantum Hall effect is the quantization of the Hall resistivity in the presence of strong out-of-plane magnetic field. Two-dimensional electron systems in the presence of a perpendicular magnetic field tend to form quantized orbits of motion because of the cyclotron motion developed. The orbits are known as Landau levels. In graphene, the quantum Hall effect can be observed at liquid Helium temperatures and the application of 1 Tesla (T). However, the effect is also observable at room temperature with the application of fields as high as 45 Tesla [17]. The quantum hall effect manifests itself differently from more conventional materials. In the case of graphene, there is a Landau level at zero energy, half integer values of conductance and the Landau level energy spacing varies as a square root [1].

The second phenomenon is graphene's finite conductivity. Graphene, unlike other semiconductors, has a zero band-gap structure that meets at the Dirac points. The result is a density of states of zero at the tip of the cones. Nevertheless, a minimum conductivity is still measured at those points. The reason of the finite conductivity is found in the presence of defects, impurities and the scattering mechanisms of graphene. Scattering in graphene

consist of the effects that impurities and defects can have on the transport properties. The effects are not limited to the Dirac energy, as effects on the carrier density are also dominant near this energy.

The theoretical framework used in analyzing scattering comes from the Landauer formalism, where the electrical conductivity can be computed based on the regime the material operates in [18]. The mean free path l_{mfp} determines the regime for transport purposes. If the mean-free path is greater than the total sample length that is l_{mfp} > L, the regime is ballistic, in which case the ballistic conductivity is computed by:

$$\sigma_{ball} = \frac{4Le^2}{Wh}\sum_{n=1}^{\infty} T_n$$

where the sample length and sample width are denoted by L and W, respectively. The transmission probabilities are denoted by T_n, e is the electron charge and h is planck's constant [17].

The minimum conductivity can be computed as σ_{min}= $4e^2(\pi h)^{-1}$ = $4.92\times10^{-5}\ \Omega^{-1}$.

In the case of the mean-free path being smaller than the sample's length, that is $l_{mfp} < L$, the regime is called diffusive, and the electrical conductivity depends on the mechanisms that are dominant in the system. The electrical conductivity can be computed [17] by :

$$\sigma_d = \frac{2\pi e^2 v_F \tau}{h}\sqrt{\frac{n}{\pi}}$$

where τ is the relaxation time, which is heavily dependent on the type of scattering taking place in the sample.

The types of scattering that occur in graphene are phonon, Coulomb and short-range scattering. Phonons, specifically longitudinal acoustic phonons, have a strong interaction

with the electrons in the lattice due to the phonon energy being less than the Fermi energy. As a result, there are quasi-elastic collisions of electrons with the lattice. The threshold or baseline used to study the collisions is the Bloch-Gruneissen temperature, defined as $k_B T_{BG} = 2k_F v_{ph}$, where the Fermi wavevector is $k_F = \sqrt{n\pi}$, and n is the electron density at the conduction band [19]. The resistivity ρ has different proportionalities based on whether the temperatures involved in the process are below or above T_{BG}. In the case of $T \ll T_{BG}$, or degenerate regime, the resistivity has a nonlinear behavior in the order of T^4 [20]. On the other hand, ρ has a linear temperature dependent relation for the equipartition case where $T \gg T_{BG}$.

A second source of scattering in graphene involves the presence of charged impurities. The effect of the charge impurities, often modeled as trapped ions, is the screening of electrons. This type of scattering is called Coulomb scattering. By using a semi-classical approach [21] the charge scattering impurity is proportional to $\sqrt{n/n_i}$ and the conductivity of this type of scattering is given by:

$$\sigma_i = \frac{C_{SS} e^2 n}{h n_i}$$

assuming $n \gg n_i$ with C_{SS} being a material specific parameter associated with scattering strength. In the case of silicon oxide, the parameter C_{SS} ~20.

Finally, graphene is also subjected to short-range scattering. This kind of scattering corresponds to defects or vacancies in the material. Defects in the lattice structure of graphene often result in midgap states [22]. The effect on the transport properties resembles

the linear relation of the conductivity and the charge density, and a mobility inversely proportional to the donor density. The conductivity can be computed:

$$\sigma_d = \frac{2e^2 n}{\pi h n_d} \ln^2 \sqrt{\pi n R}$$

Where R is the radius of a circular potential well.

The theoretical approaches help model the transport properties of graphene; however, graphene is a highly anisotropic material. For that reason, it is more practical to obtain the conductivity using direct measurements. The conductivity σ, of monolayer graphene can be found via the Hall bar geometry, shown in figure 7, and standard Hall measurements. The conductivity of a material is related to the material's mobility μ_e and carrier density n by $\sigma = ne\mu$ [23]. Hence, in order to obtain the carrier density and the mobility, the transverse resistivity is required. The transverse resistivity, ρ_{xy}, can be computed from measurements of transverse voltage and applied longitudinal current. As a result, the carrier density is $n = B/e\rho_{xy}$ where B is the perpendicular applied magnetic field. Finally, the Hall mobility is $\mu_H = 1/ne\rho_{xx}$. This Hall mobility in suspended monolayer graphene is in the 200,000 cm^2/Vs range [24].

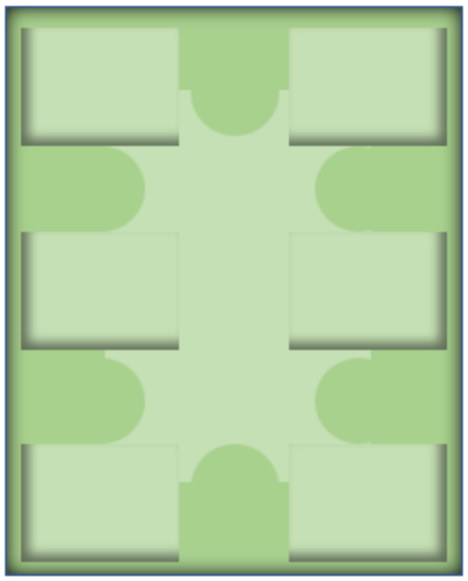

Figure 7 Hall Bar measurement setup

Another way of computing the electrical conductivity is by taking advantage of the ambipolar field effect. By applying a gate voltage to graphene on a silicon oxide substrate, the carrier concentration (electron or hole) can be tuned. At the moment of gate voltage application, a surface charge density is electrostatically introduced in the material. The charge density is given by:

$$n = \frac{\epsilon \epsilon_0 V_g}{de}$$

where e is the electron charge, V_g is the applied gate voltage, d is the substrate thickness, while ϵ and ϵ_0 represent the electrical permittivity of the substrate and of free space, respectively.

The key ingredient in calculating the electrical conductivity σ is the mobility. The field effect mobility can be computed by:

$$\mu_{FE} = \frac{d\sigma}{C_g dV_g}$$

where C is the capacitance defined as $C = ne\left(V_g - V_{gD}\right)^{-1}$, with V_{gD} being the gate voltage at the Dirac energy [25].

The value of the mobility of graphene changes based on the substrate as well as the technique used to produce the graphene.

In conclusion, graphene is a material whose unique electron band structure allows for several interesting properties. High mobility values as well as conductivity can be found in graphene which imply high electron mean free path. These electronic properties, in turn, have significant implications in phenomena such as that of superconductivity given the tunability of electron density, the density of states at the Fermi level as well as a long mean free path.

C. Thermal Properties

Heat flow in a material is described by Fourier's law of heat conduction. The law is stated in the following form: $\boldsymbol{j_q} = -\kappa \nabla \boldsymbol{T}$, where $\boldsymbol{j_q}$ is the local heat flux, $\boldsymbol{\nabla T}$ is the thermal gradient and κ is the thermal conductivity. The thermal conductivity is a material-dependent quantity that gives a measure of the ability of a material to conduct heat. At the mesoscopic range, a common way of calculating this quantity is using a Landauer approach to thermal conductivity, which considers the phonons and vibrational properties involved in heat transfer.

Vibrational properties in graphene are of high importance, given that they tend to produce high values of thermal conductivity. Graphene is composed of light carbon atoms with very sturdy and strong in-plane σ bonds. As a result, they have a high in-plane sound velocity

(20 km/s) [17]. Moreover, the strong bonding energy, found to be 5.9 eV, makes it difficult for structural defects to break bonds and form within the lattice. It is also expected that graphene's low dimensionality lowers the number of states that phonons can scatter with, resulting in a strong material with a long phonon coherence length, in excess of 200 nm, due to the lack of phonon scattering involved.

In order to analyze the vibrational properties and, consequently, the thermal properties of graphene, it is often imperative to look at the dispersion relation of the phonons in the system.

The vibrational properties or the modes involved in graphene are: transverse acoustic, transverse optical, longitudinal acoustic and longitudinal optical for in-plane vibrations. In the case of the out-of-plane vibrations the acoustic (ZA) and optical (ZO) modes are decoupled [17]. The most known and obvious ones are the longitudinal mode (LA) in the direction of the wave propagation and two transverse acoustic (TA) perpendicular to the wave propagation for in-plane phonon propagation. The most important phonon mode involved in heat conduction in graphene is the flexural mode (ZA) which is perpendicular to the plane and has a quadratic dispersion relation [26]. The flexural mode can carry high amounts of heat due to a higher heat capacity than the other modes involved for temperatures close to 360 K; it also has a larger scattering time.

In practice, a common method for measuring the thermal conductivity of materials is the use of the 3ω method. This method consists of calculating the thermal behavior of a film by using Joule heating. For this purpose, a metal strip is place on top of the substrate, and a sinusoidal current of the form $I = I_0 \cos(\omega t)$ is run through it. From the current the Joule heat per unit length per unit time can be computed, as well as the resistance per unit length.

From those parameters the root-mean-square voltage drop across the stripe can then be deduced, as well as the average oscillatory temperature. Finally, the oscillatory temperature and the current frequency are related to each other via the thermal conductivity of the substrate. A key point in the utilization of the method is the fact that the thickness of the material has a high degree of uncertainty in the power dissipated across the *c*-axis [27]. As a result, the thermal conductivity of low-dimensional materials is difficult to measure using the 3ω method.

In order to measure the thermal conductivity of low dimensional materials, Balandin and his team used what is now known as optothermal Raman thermometry. The method was first used on graphene of thickness less than 2 μm [28]. The reason the method was used was the observation that the Raman sensitive G mode, or Carbon to carbon bond elongation, was sensitive to heat, varying linearly over temperature. Therefore, shifts in the G mode can arguably be taken to be due to anharmonicity, and; therefore, a Raman spectrometer can be used as an optical thermometer [29]. The technique works by heating up the suspended sample with a laser, and measuring the heat dissipated through the G peak shift. Then, through the heat-diffusion equation, and a known geometry, the thermal conductivity can be extracted from the data. By using this technique Balandin's team found thermal conductivities of 3000 W $m^{-1}K^{-1}$ at room temperature from mechanically cleaved graphene. Figure 8 shows the setup of the optothermal technique schematically.

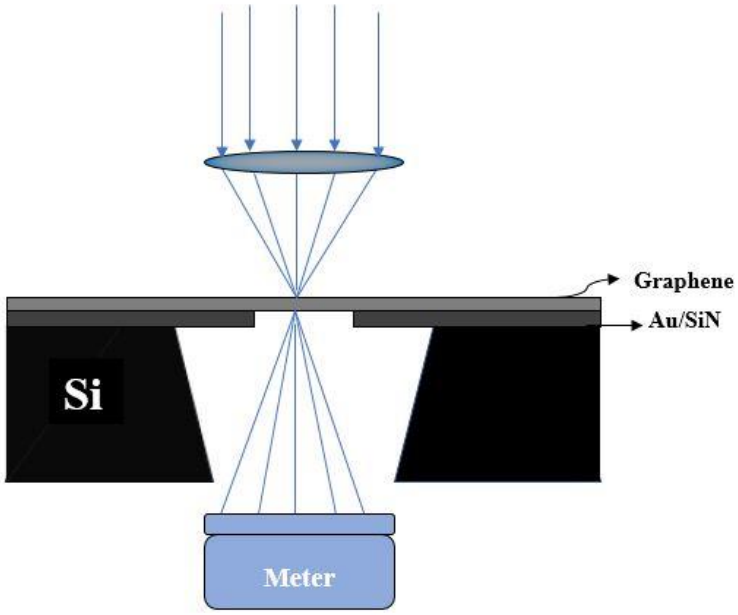

Figure 8 Schematic of a thermal Raman spectroscopy setup. A laser beam is focused at a lens to heat up a graphene sample. The heat dissipation is measured by a meter placed below the sample.

In order to determine and analyze the thermal conductivity in graphene, it is important to look at the kinetic theory of gases. Using the model, the thermal conductivity is the product of the in-plane sound velocity, the specific heat per unit volume and the phonon mean-free path, or mathematically: $\kappa = v_s C_V(T)\lambda_{mfp}$. Due to the very high sound speed of graphene, the material is also expected to have a high thermal conductivity. An experiment in sets of graphene flakes [30] found thermal conductivities as high as 5150 W $m^{-1}K^{-1}$ at room temperatures with phonon mean free path as high as 775 nm. The measurements were made using confocal micro Raman spectroscopy techniques.

Other important results in monolayer graphene include an intrinsic, that is only phonon scattering involved, thermal conductivity ranging from 2000 W $m^{-1}K^{-1}$ to 4000 W $m^{-1}K^{-1}$ at room temperature for suspended monolayers and from 700 W $m^{-1}K^{-1}$ to 1500 W $m^{-1}K^{-1}$ at 500 K. The reason for the decrease in thermal conductivity, as compared to its bulk counterpart having a thermal conductivity of 2000 $Wm^{-1}K^{-1}$ at room temperature, is the

steep temperature dependence of graphene; it is mainly due to second-order three phonon scattering, that is $\tau \sim T^{-2}$, because of the flexural modes in graphene.

It is commonly understood that rigidity is a damper for vibrations, and, thus, for thermal conductivity. Monolayer graphene, when in a suspended setting, can reach values as high as 4000 W $m^{-1}K^{-1}$. In the case of bilayer graphene, thermal conductivities often reach 2800 W $m^{-1}K^{-1}$, but the thermal conductivity is reduced to 1300 W $m^{-1}K^{-1}$ as the layer number goes from 2 to 4. However, adding layers to graphene as a form of substrate, take for instance SiO_2 in a SiO_2/Graphene/ SiO_2 structure, produces a thermal conductivity of 1000 $Wm^{-1}K^{-1}$ at room temperature and a thickness of 8 nm. This effect can bleed over to silicon oxide substrates for 2.5 nm or around 7 layers of material, due to phonon leakage [31]. Recent studies have also confirmed the high phonon mean free path of graphene even on metal substrates. By use of the Helium Atom Scattering method (HAS), the electron-phonon coupling constant increased with decreasing substrate interaction, implying the increase in the displacement of the vibrations. In other words, systems that where weakly bonded (with substrate separations of 0.3 nm) had a high measured electron-phonon constant of 0.89, with free standing graphene having an electron-phonon constant of 0.32 [32].

Extrinsic effects also play an important role in the thermal conductivity of graphene. In practice, graphene is not often free of impurities or defects. As a result, they can present a significant interaction with graphene's vibrational properties, and, thus, on the thermal conductivity. In addition, the composition of graphene, whether monolayer or few-layer graphene, can lead to strain. Strain, whether compressive or tensile, can produce stiffing of the lattice, and of phonons. The stiffening of phonons leads to a decrease in the thermal

conductivity. More specifically, tensile strain will lead to the softening of modes while compressive strain will lead to buckling which, in turn, will cause more phonon scattering [33,34]. Other effects such as vacancies, via molecular dynamics, lead to broad phonon dispersion relations which decrease the phonon mean-free path as well as an increase in phonon density [35]. Finally, graphene is also subject to isotopic effects. Changes in mass and size decrease the thermal conductivity, as these parameters are inherent to phonon scattering mechanisms, leading to a decrease in κ from 4000 W $m^{-1}K^{-1}$, for isotopically pure graphene, to less than half in other carbon isotopes [36,37].

D. Magnetic Properties

In carbon-based materials, paramagnetic signals are generally thought to come from metallic impurities found in the material. In the case of graphene, magnetic moments that are present in the material ultimately come from impurities as well as vacancies [38]. The study of magnetic signals in graphene results quite difficult, given that the weak signals generated are not necessarily, or conclusively, inherent to the carbon allotrope. Instead, several studies, discussed here, agree that metallic impurities, vacancies, and dislocations are responsible for magnetic moments.

Ideal graphene is purely diamagnetic; that is, it does not become magnetized when subject to an applied magnetic field. Nevertheless, several factors can tune graphene to become magnetized. Such factors include single-atom defects forming odd-membered rings, as well as structures forming pentagons and heptagons [39]. Some theoretical work [40] has also hypothesized that the stacking pattern, specifically A-B, must also contribute to magnetism: The zigzag edging in graphene becomes significant as the thickness decreases

[41], or as the number of layers is reduced, the edges of graphene can take different geometries, which contribute to unpaired electrons, and; consequently, magnetic moments [42]. The use of graphene nano-flakes has allowed for some interesting predictions in the magnetic behavior of graphene. For instance, it has been hypothesized that spin polarization can be a stabilizing mechanism in graphene nano-flakes, as it can potentially counter the effect of zig-zag edges [43]. Many conflicting conclusions have also been drawn given the purity, or lack thereof, of some graphene and highly oriented pyrolytic graphite (HOPG) samples. Although graphene flakes obtained via chemical exfoliation [44] have shown signs of ferromagnetism at room temperature with superconducting quantum interference device (SQUID) measurements, other studies involving chemical exfoliation of high purity HOPG [45] show no signs of ferromagnetism down to 2 K. Nevertheless, the addition of layers can potentially induce paramagnetism in the sample. Thus, those studies show that the structure of monolayer graphene and graphene flakes as a source of magnetism is inconclusive.

The study of edges and structures as a source of magnetism in graphene continued to show interesting results. Another study showed that the introduction of vacancies, and adatoms, by high energy protons and fluorine with xenon decomposition [46], showed no ferromagnetism whatsoever. Nevertheless, some of their samples from different grades (ZYA, ZYB and ZYH) did show ferromagnetism, though it was later attributed to iron impurities via dispersive X-ray spectroscopy. As a result, graphene's magnetic signals, in general, tend to come from metallic impurities even in the purest samples.

There seems to be, however, some agreement in the sources of magnetic moment within graphene at the nanoscale, whether the source is the introduction of defects, the addition of

adatoms or the exchange interaction of fully populated states [47]. The structure of the lattice plays again an important role in the formation of magnetic moments. Given the sp^2 hybridization of carbon along with the partially filled π orbital of each carbon atom, there is coupling in an antiparallel way with the nearest neighbor. The coupling is important in the establishment of long-range coherence at high temperatures due to the repulsive nature of the exchange at the π orbitals [48]. The long-range coherence due to the lattice creates a promising environment for long-range spin polarization. In the case of finite graphene, topological "frustration" of the π bonds seem to be what drives the shape of graphene. As a result, magnetism in any form in graphene, as small as it be, depends greatly on the shape [49].

Localized magnetism in graphene was first hypothesized in Lieb's theorem where a defect in a lattice can potentially generate magnetic moment. Having a vacancy in a graphene lattice, essentially having sublattice sites, can generate spin polarized electron density since it removes four electrons from that band as in figure 9. The removal leaves three covalent σ-bonds unsettled, with one electron forming a narrow resonant state due to being π quasilocalized. From Lieb's theorem, the last electron π will contribute to one Bohr magneton [50]. Furthermore, by Hund's coupling, the occupied σ electrons couple with the π states providing for two Bohr magnetons, which, due to Kondo-like coupling, will reduce to about 1.7 of a Bohr magneton [51]. Theoretically many first principles and density functional theory calculations agree with the given result [52].

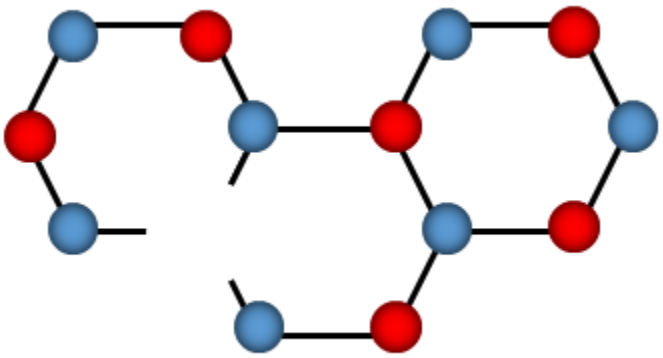

Figure 9 Vacancy in the graphene lattice

Graphene has been hypothesized to be able to have magnetic moments from several sources. Moreover, it can potentially be used in several applications due to its long spin lifetime and spin coherence. More specifically, spintronic devices. However, there are some inherent characteristics and magnetic properties that hinder such efforts. One of them is graphene's spin-orbit coupling. Spin-orbit coupling is responsible for many phenomena in graphene such as such as the spin Hall effect, quantum anomalous Hall effect, and spin-dependent Klein tunneling [53,54]. There can also be significant consequences in the spin properties of graphene from spin-orbit coupling since it effectively quenches spin coherence due to being responsible for spin relaxation [55]. Spin relaxation in graphene remains an open issue that has not reconciled the fact that experimental and theoretical values are discrepant by at least two orders of magnitude [56-58].

Table 1. Symbols and acronyms

Symbol/Acronym	**Description**	**Numerical Value**
s	S orbital	-
p_x, p_y, p_z	P orbitals directed in x,y, or z	-
kJ	kiloJoules (Energy unit)	-
Sp^2	Hybridization	-
mol	Molecule	-
$\boldsymbol{a_1}, \boldsymbol{a_2}$	Graphene's translation vectors	-
$\dot{A}$	Angstrom	10^{-10} meters
σ_{st}	Engineering stress	-
N	Newtons (Unit of force)	-
m	meter	-
ϵ_{st}	Engineering strain	-
E_{yn}	Young's modulus	-
AFM	Atomic force microscope	-
k_{sp}	Spring constant	-
GPa	GigaPascals (unit of pressure)	10^9 Pascals
VDW	Van der Waals	-
E	energy	-

k	Wave vector	-
k_x, k_y	Wave vector components in x and y	-
K_D, K_D'	Dirac points in momentum space	-
eV	Electronvolt (energy unit)	1.602177×10^{-19} J
v_F	Fermi velocity	-
τ_{lt}	Carrier lifetime	-
T	Tesla (unit of magnetic field)	-
fs	Femtosecond	10^{-15} seconds
l_{mfp}	Electron mean-free path	-
L, W	Length, Width	-
h	Planck's constant	$6.626 \times 10^{-34} m^2 kg\ s^{-1}$
T_n	Transmission probability	-
τ	Relaxation time	-
e	Electron charge	1.602×10^{-19} Coulombs
σ_{ball}	Ballistic conductivity	-
σ_d	Diffusive conductivity	-
k_B	Boltzmann constant	$1.381 \times 10^{-31} kg\ s^{-1} K^{-1}$
K	Kelvin (temperature unit)	-
T_{BG}	Bloch-Gruneisen temperature	-
k_F	Fermi vector	-

ρ	Resistivity	-
C_{SS}	Scattering strength parameter	-
σ_i	Impurity conductivity	-
n	Carrier density	-
μ	Electron mobility	-
B	Magnetic field intensity	-
μ_H	Hall mobility	-
ϵ	Electrical permittivity	
V_g	Gate voltage	-
V_{g_D}	Dirac gate voltage	-
$\boldsymbol{J_q}$	Heat flux	-
$\boldsymbol{\nabla T}$	Thermal gradient	-
κ	Thermal conductivity	-
λ_{mfp}	Phonon mean-free path	-
C_V	Specific heat capacity per volume	-
v_s	Sound velocity	-
W	Watts (Unit of power)	-
HAS	Helium Atom Scattering	-
HOPG	Highly oriented pyrolytic graphite	-
SQUID	Superconducting quantum interference device	-

III. 2D SUPERCONDUCTIVITY

Superconductivity is a macroscopic quantum phenomenon characterized by zero DC resistivity and perfect diamagnetism, the latter known as Meissner effect. Superconductivity has been studied laboriously ever since its discovery by Kamerlingh Onnes in 1911 [59]. Several macroscopic and phenomenological theories have been developed in order to understand the phenomenon such as London's equations and Ginzburg-Landau theory. A purely quantum and microscopic theory did not arrive until the Bardeen-Cooper-Schrieffer (BCS) theory in 1957 [60], which is characterized by a phonon mediated mechanism for pairing electrons which, in turn, are responsible for superconductivity. Moreover, in superconductors, the appearance of an exponential term in the specific heat pointed to the existence of an energy gap where superconductor carriers were allowed but normal electrons would not. Electromagnetic absorption measurements showed that indeed that was the case. In a BCS framework, the superconductor energy gap, of the order of 10^{-3} eV, is related to the critical temperature by the following equation:

$$T_c \sim \frac{\Delta_{sc}(0K)}{k_B 3.53}$$

Where k_B is Boltzmann's constant and $\Delta(0K)$ is the energy gap at 0 Kelvin—where it is maximum. The critical temperature can be estimated by:

$$T_c \sim 1.14\Theta_D \exp\left(-\frac{1}{DOS(E_F)U_{e-ph}}\right)$$

Where Θ_D is the Deybe temperature, $DOS(E_F)$ is the density of states at the Fermi level and U_{e-ph} is the electron-phonon coupling coefficient.

From the equation, it is important to notice that increasing either the electron-phonon interaction and/or the density of states at the Fermi level yields an increase in the critical temperature. For that reason, the introduction of ways to increase such parameters such as doping to increase the interaction, topological changes, and strain, have been used to increase and potentially engineer superconductors. More recently, the engineering of flat bands has been of great importance as a flat band leads to a maximum in the density of states at the Fermi level—it diverges.

The BCS theory proved to be a good analytical tool for type I superconductors. However, the emergence of other types of superconductivity, such as unconventional types and high-temperature superconductivity, has brought more attention into researching this phenomenon.

As the dimensions of a material are reduced for more sophisticated applications, the effects on the electronic and vibrational properties of materials become more relevant. In the case of superconductivity, two-dimensionality contributes to low density of electrons, leading to low probabilities of pairing. Moreover, low dimensionality reduces screening which suppresses Cooper pairing. Finally, there is a loss in long-range phase coherence due to fluctuations causing reduction in phonon-mediated pairing as well as the presence of topological defects that can potentially make the material metallic.

A. The Mixed State

A general parameter by which superconductors are classified is the London penetration depth-to-coherence length ratio $\left(\frac{\lambda_L}{\xi}\right)$. The ratio is often called the Ginzburg-Landau parameter, denoted here by κ_{GL}. The parameter's value determines whether a

superconductor falls into the type-I kind, mostly comprised of elemental materials, or type-II, mostly comprised of alloys and ceramic oxides. Type-II superconductors are characterized by an intermediate region between the normal phase and the purely superconductive phase; the latter being the region where the full Meissner effect occurs. The mixed state of type-II superconductors is characterized by the presence of vortices, similar to the vorticity phenomena found in the superfluid Helium-4 [61]. Vortices are objects of supercurrent circulation at the mesoscopic range containing a "normal," non-superconducting, core and quantized magnetic flux whose magnitude is given by $\phi_0 = \frac{h}{2e}$; h being Planck's constant and e the electron charge. The length or radius of their core is given by the coherence length ξ. The vortices in a type-II superconductor were first predicted by Alexei Abrikosov as a solution to spatial variations of the Ginzburg-Landau order parameter [61]. Vortices form a lattice, often called the Abrikosov lattice that tends to align in either rectangular or triangular shapes. Moreover, since a two-dimensional superconductor requires the coherence length to be bigger than the thickness of the sample, some superconductors can be considered three-dimensional in the physical sense. In other words, materials that are not in the atomic range thickness and that have more than a few monolayers can be considered two-dimensional for superconductivity purposes [62]. In layered materials with weak interlayer coupling, that is an interlayer interaction smaller than the thermal energy, the vortices take the form of what is known as Pearl or "pancake vortices". Pearl vortices are objects of magnetic quanta whose field intensity varies as *1/r*, and have long-range interaction as opposed to the logarithmic variation and short-range interactions in conventional Abrikosov vortices [63].

Due to the high anisotropy of type-II superconductors, the flux quanta are divided along the c-axis of the material, as they make a more energetically favorable structure. Pancake vortices interact strongly within the same layer but weakly with neighboring layers; similar to magnets with the same polarity placed on the same surface.

In the mixed state, vortices are generated along with their antivortex counterparts. In a superconductor with the coordinates and geometry of figure 10, vortices and antivortices meet several forces. Under stationary conditions, vortices are subjected to forces similar to those of superfluid vortices.

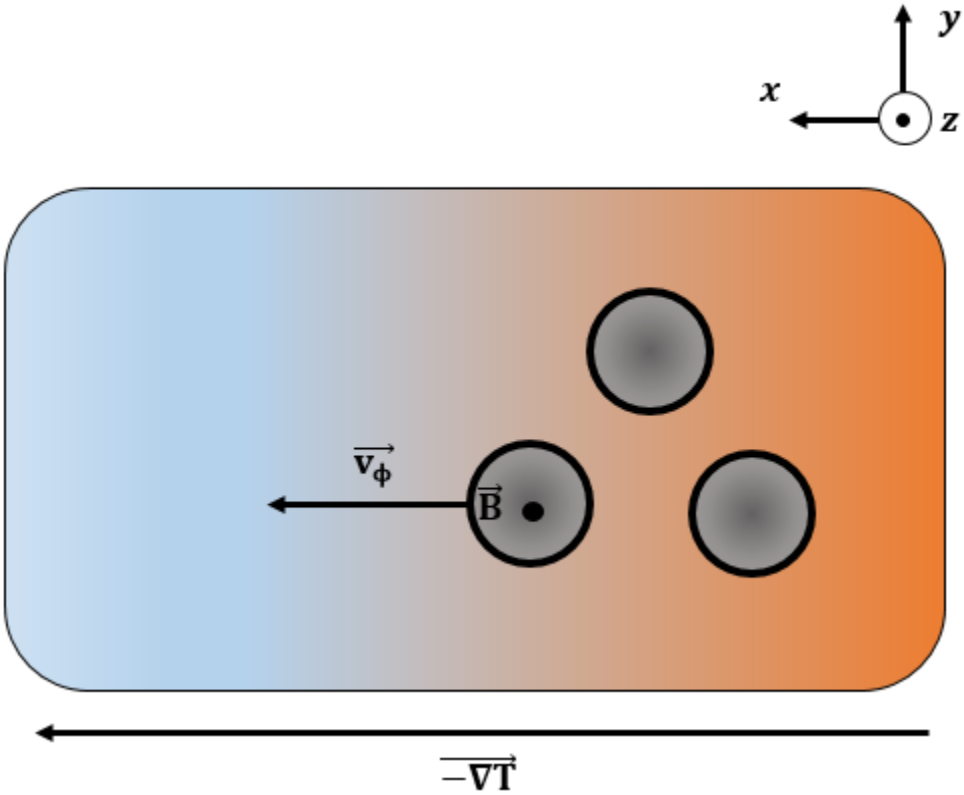

Figure 10. Sample geometry with an applied thermal gradient in the x direction and applied magnetic field in the *z* out-of-plane direction. The vortices move with velocity $\boldsymbol{v_\phi}$ from the hot side (red) to the cold side (blue).

Assuming constant vortex velocity, there is a damping or "viscosity" in the system; this viscosity in a superconductor is given as a coefficient γ times the velocity of the moving vortex $\boldsymbol{v_\phi}$. Moreover, the material's composition can also have an effect of the moving vortex. In particular, defects in the material, often called pinning sites, represent potential wells to the vortex. As a result, a force $\boldsymbol{F_p = J_c \times B}$ needs to be overcome in order to get a vortex "out" of such sites. The last force compensating the motion is the Magnus force. The Magnus force is a fluid analog applied to superconductors; this force is an interaction between the "fluid" motion and a rotating object, in this case the vortex. The Magnus force is given by $\theta n_s e(\boldsymbol{v_\phi \times \phi_0})$ where n_s is the density of superconducting electrons, e is the fundamental electron charge, $\boldsymbol{v_\phi}$ is the velocity of a vortex having $|\boldsymbol{\phi}|$ flux; the angle θ represents the amount of the Magnus force that is applied to the vortex in practice. Finally, the motion of the vortex itself is given by the Lorentz force. Following Newton's second law, the force equation for a vortex in a material under stationary conditions and no thermal gradients is given by:

$$\boldsymbol{j_n \times \phi_0} - \theta n_s e\big(\boldsymbol{v_\phi \times \phi_0}\big) - \gamma \boldsymbol{v_\phi} - \boldsymbol{J_c \times B} = 0$$

The previous equation describes the dynamics of a vortex under stationary conditions. However, it is usually modified to include other forces driving motion in the system. The most commonly used source of motion for experiments is a thermal gradient. In which case, the dynamic equation becomes:

$$-\boldsymbol{S_\phi \nabla T} - \theta n_s e\big(\boldsymbol{v_\phi \times \phi}\big) - \gamma \boldsymbol{v_\phi} - \boldsymbol{J_c \times B} = 0$$

Where $-\boldsymbol{S_\phi \nabla T}$ is the thermal driving force, $\boldsymbol{S_\phi}$ being the transport entropy per vortex and $\nabla \boldsymbol{T}$ the thermal gradient.

Superconductors in a temperature gradient display useful phenomena that comprises the basis for experiments regarding the presence of vortices, such as the Nernst effect. When a superconductor is in the mixed state and is subjected to a temperature gradient, the objects present in the material will diffuse from the higher entropy side, hot, to the low entropy side, cold. In the presence of an applied magnetic field orthogonal to the direction of the magnetic vortex's motion there is a corresponding cross product force that causes the diffusing magnetic vortex, and core quasiparticles, to experience a force orthogonal to both their motion and the applied magnetic field. The resulting imbalance of objects, in this case electrons, results in a potential in the transverse direction. It is this transverse voltage that is known as the Nernst voltage and the entire effect is known as the "Nernst effect."

B. The Nernst Effect

The Nernst effect is an elegant way of testing for vorticity or flux quanta in a superconductor. The measured transverse voltage resulting from a thermal gradient and a perpendicular magnetic field can arise from three cases: The voltage may come up as a result of flux flow involved in the materials as previously stated. However, the induced voltage can also have a contribution from quasi-particles due to the transverse or "sideways" deflection as a result of the Lorentz force acting on them. In the case of vortices, peaks with a steep drop on the colder side and an undulation on the hot side are the staple when recognizing transverse effects due to vorticity. Fluctuating Cooper pairs are also a source of Nernst signals. The shape and contribution to the Nernst signal is often analyzed via thermoelectric experiments.

Thermoelectricity is the generation of electric field due to a thermal gradient, or vice versa, in a material. Several effects correspond to such phenomena, namely, the Seebeck effect,

Peltier cooling, among others. A classical thermodynamic approach can be used to understand the nature of the phenomenon. In a classical framework, wherein thermoelectricity is modelled as an engine, a Fermi gas is usually considered a perfect gas [64] with an appropriate set of equivalences. Most notably, the partial pressure. In the case of a Fermi gas, the partial pressure can be modeled as a potential μ_T consisting of the electrostatic field $\mathcal{E}$ and a chemical potential μ_{ch}, thus, $\mu_T = \mu_{ch} + \mathcal{E}$

In using a classical analysis from the kinetic theory of gases, a channel with a temperature difference will have a distribution of high-velocity particles at the hot end. As a result, the gas at the hot end will have a high volume and, therefore, a small density. On the other hand, the cold end will have a low gas particle velocity, low volume and a high density as a result. Since there is, indeed, a temperature difference and heat flow, it can be concluded that there is a flow of carriers. The carrier density, in turn, produces a voltage difference. Therefore, in such a simple system, it is possible to see the relationship or "coupling" of both types of fluxes. The process can be divided into two isothermal branches at each temperature side, and two adiabatic branches: hot to cold and cold to hot. Entropy in the system is, then, coming from the adiabatic branches due to particle collision or interaction with other particles as well as the lattice. Given that the Fermi gas carries entropy in the adiabatic branches, it can be thought that each quasiparticle can carry entropy individually; fact that was shown by Callen [65]. It is important to notice that the classical approach does not deal with non-equilibrium phenomena occurring in the system.

The Onsager-Callen formalism or framework is preferred when dealing with quantifiable thermoelectric phenomena. Onsager's relations depict the fact that, in an irreversible system, the fluxes (as tensors) and their corresponding driving forces are coupled [66,67].

Callen's contribution was the grounding or foundation of the Kelvin and Bridgman observations in a more suitable theory based on Onsager's relations. In other words, the link between thermoelectric coefficients was derived directly from the Onsager's relations. It is because of this link that a more general principle from transverse phenomena can be inferred from the Onsager relations. The ratio of the gradients involved in the system, the electric field and thermal gradient, is related to the ratio of their corresponding fluxes. As a result, a definition of the Nernst coefficient involving entropy can be obtained: The Nernst coefficient measures the resulting transverse entropy due to longitudinal flow, whether it is quasiparticle or magnetic flux flow.

The work of Behnia and Aubin [68] demonstrates the fact that the transverse thermoelectric response in a material can be represented as the transport entropy per unit charge or particle. In their work they found an expression for the Seebeck coefficient using the thermoelectric coefficient and electrical conductivity expressions from Van houten and others [69-71]. The Seebeck coefficient corresponded to the ratio of the thermoelectric coefficient to the electrical conductivity coefficient. The observation implies that the ratio of entropy per electron to electric charge is also an expression for the Seebeck coefficient.

The same reasoning was applied to find the transverse responses. The Hall conductivity σ_{xy}, for instance, can be obtained in a similar manner [72]. The Hall conductivity is the ratio of the transverse current and the longitudinal applied electric field. The ratio, per particle, can be represented as $\sigma_{xy} = e/\phi_p$, where ϕ_p is the flux per particle. The flux per particle is found, by Boltzmann's approach, to be the expression:

$$\phi_p = \frac{h}{e}\left(\frac{l_B}{l_{mfp}}\right)^2$$

Where l_B is the magnetic length, l_{mfp} is the mean-free path and h is Planck's constant. Finally, the transverse coefficient of thermoelectricity is the ratio of the entropy per particle to flux per particle or $\alpha_{xy} = \widetilde{S_p}/\phi_p$. The expression comes out to be:

$$\alpha_{xy} = \frac{k_B e}{h}\left(\frac{l_{mfp}}{l_B}\right)^2\left(\frac{\lambda_F}{\Lambda}\right)^2$$

The previous expression is the magnitude of the transverse response due to a longitudinal thermal gradient and a perpendicular applied magnetic field by electrons. It is noted that the Hall effect in the mixed state of anisotropic and layered superconductors changes sign and it is related exponentially to the longitudinal field.

The transverse response due to flux quanta is then the ratio of the entropy per vortex to flux quantum. Thus, the transverse response due to vortices in a superconductor corresponds to the expression:

$$\alpha_{xy} = \frac{S_\phi}{\phi_0}$$

In the expression above S_ϕ corresponds to the entropy per vortex, often called the transport entropy per unit length and ϕ_0 is the flux quantum. The Nernst coefficient Ɲ can then be defined as the transverse thermoelectric response times the flux flow resistivity ρ_{ff} or:

$$Ɲ=\rho_{ff}\alpha_{xy} = \rho_{ff}\frac{S_\phi}{\phi_0}$$

A classical force-based approach analysis leads to simpler understanding of the effects in the longitudinal direction. The thermal force acting on both electrons and vortices induces flow down the temperature gradient. The imbalance of electrons in the vortex cores causes the Seebeck effect as long as the vortices are pinned. The effect of the supercurrent at temperatures less than T_c makes the vortices deviate allowing the backflow supercurrent to

cancel the normal current in the core. The Seebeck effect cannot be observed in a type-I superconductor due to field screening.

Moreover, the same approach used in the transverse direction can help in understanding the Nernst effect. The movement of vortices down the temperature gradient induces a force (Lorentz) on the flux present at temperature below, but near, the critical temperature. The force causes a transverse electric field which is the main component of the Nernst effect. It is also important to note that there is another transverse force present; the Magnus force, which is believed to be the source of the sign reversal in the Hall component.

Just like the Seebeck coefficient, the best way of finding out such quantities is by measuring the transverse response on a controlled thermal gradient and applied magnetic field.

Several experiments have made use of the Nernst effect as a means of detecting vorticity in the material. The first experiments measuring the Ettinghausen and Nernst signals come from Lowell et al [73]. Moreover, Huebener [74] also produced work on measuring Nernst signals in high-purity Niobium films, an elemental type-II superconductor, of 11-18 μ thickness. The experiment produced Nernst signals of up to 4.8 μV in the vicinity of 700 Gauss at 12 K. Huebener also measured Nernst signals in yttrium barium copper oxide (YBCO) [75] with magnitudes as high as of 2.7 μV/K in the vicinity of 80 K with an applied magnetic field of 12 T. In addition to Huebener's work, other experiments on cuprate superconductors were also published following the discovery of high-Tc superconductors [76]. Cuprate superconductors are known to have a broad resistive or mixed-state region due to their inherent high anisotropy [77]. One of the cuprates with the biggest Nernst signals is overdoped Lanthanum Strontium Copper Oxide (LSCO), which shows signals as high as 2.5 μV with applied field of 10 T at 16 K [78-80]. In addition, a

change in the Nernst signal's sign is reported due to the contribution to the Nernst signal of holes. On the other hand, underdoped LSCO has shown a clear broad Nernst signal that is simple to separate from hole contribution. Other types of interesting high-Tc superconductors have also emerged in recent years. Most notably, the iron-based superconductors which have measured Nernst signals as similar in magnitude as those of cuprates [81,82]. Nernst signals have also been observed in phosphorus-doped graphene at temperatures as high as 260 K [83].

C. The Berezinskii-Kosterlitz-Thouless Transition

Although several issues such as disorder and anisotropy arise from low dimensionality, there are mechanisms that still allow for superconductivity to occur in low-dimensional materials. One of such mechanisms is the Berezinskii-Kosterlitz-Thouless (BKT) transition. A BKT transition is characteristic of two-dimensional superconductors as it arises from the presence of topological defects in the form of vortices and antivortices. Topological defects are generally thought to come from the increased fluctuations as the dimensionality is reduced [84]. The existence of a BKT transition implies the establishment of a quasi-long coherence range correlation of the order parameter [85-87]. Moreover, at the mean-field level, the BCS mechanism for pairing still holds, though it is affected by other phenomena, such as the superconductor-insulator transition, which can weaken the pairing mechanism and suppress it completely because of disorder [88]. Therefore, two-dimensional superconductivity is a very plausible event.

In the strict sense, a two-dimensional superconductor is one whose coherence length is bigger than the thickness of the film. For such films it was hypothesized [89,90] that long-range coherence could not be obtained for $T>0$. As a result, no superconductivity could be

achieved in a two-dimensional system. Nevertheless, Berezinskii et al showed that there is a quasi-long coherence range achieved at the Berezinskii-Kosterlitz-Thouless (BKT) temperature T_{BKT} [91] where $T_{BKT} < T_{BCS}$. In a BKT system, regardless of the nature of the system itself, there is a binding interaction which becomes logarithmic in nature as the temperature reaches the BKT temperature. In other words, below the BKT temperature the interaction energy between pairs is approximated by $E_{int} \sim \log(r)$, with r being the vortex pair separation. Physically, in BKT systems, vortices and antivortices are generated due to fluctuations at finite temperatures. Above the BKT temperature there is enough energy for the pairs to be unbound and move freely. However, for temperatures below the BKT temperature; there is a logarithmic, growth of the energy between vortices and antivortices as a function of vortex-antivortex distance. That is to say, the pairs become effectively bound in a net zero dipole. This situation is expected in two-dimensional systems as long as the vortex-antivortex distance does not exceed the London penetration depth. In the case of the BKT dimensions exceeding the London penetration depth, there would be free vortices moving throughout the system except at absolute zero [92]. It is also worth mentioning that not only is the vortex-antivortex interaction logarithmic below T_{BKT}, but so is entropy [93]. The BKT transition is manifested in the form of a "jump" in the power law, $V \alpha I^{a}$, where the exponent a increases from 1 to 3 as the temperature in the system is lowered below T_{BKT} [94]. In other words, there is a non-linear relationship between current and voltage (I-V).

There have been several experiments that have allowed for BKT features to be observed in He^4 [95,96]. However, given the disordered nature of most type-II superconductors as well as the small range of temperature in between the BSC and the BKT transitions, the BKT

features are more difficult to observe in a superconducting film. Making use of films with large film resistance allows for a superconducting film to develop to the dirty limit. The dirty limit, or the limit at $\lambda_L < \xi$, gives rise to a superconductor in which impurities or defects do not affect its superconductivity properties. The use of a large sheet resistance material results in a large density of vortices generated in the mixed-state of the superconductor [97]. Consequently, the BKT temperature is lowered as it takes a lower temperature to "freeze" the system. A lower BKT temperature provides for a larger window or range to observe the non-linearity. However, it is also difficult to measure since there is a far denser vortex amount in the system to which the BKT model cannot be applied [98]. A similar difficulty also occurs when using disordered homogeneous and crystalline ultrathin superconductors. Measurements of the electron density via scanning tunneling spectroscopy (STS) show that inhomogeneous systems develop in such films [99-103]. The inhomogeneity results in the pinning of vortices which in turn do not allow for a development of BKT physics [87]. In the case of crystalline superconductors the pinning is much smaller, leading to flux creep. Flux creep is the tendency of vortices to jump out of their pinning sites leading to dissipation. The dissipation keeps the vortex from forming dipoles, freezing into a lattice and setting the BKT transition.

The power law behavior at the BKT temperature, $a = 3$, would then, because of the film difficulties, be difficult to observe as it was shown in some experiments. Such experiments on crystalline Nb films [104] did not show the jump in the power law. Other experiments on crystalline films [105-107] show the expected variation of the power law, more so when the measurements were done in-situ [105], while the other samples (Nb) had protective caps. The films were single atomic layers of (Tl,Pb) on Si (111).

D. Quantum Phase Transitions

High electron localization and condensates, BKT transitions and quantum-phase transitions (QTP) are some of the most interesting properties of two-dimensional superconductors. The superconductor-to-insulator transition (SIT) is characteristic and of great importance as it is inherent in those systems. The SIT can have two main mechanisms. First, the introduction of disorder in the system from difference sources produces a change in the amplitude and phase of the order parameter. The reduction in thickness in a material causes disorder, which is the lack of long range coherence usually found in crystalline structures. In other words, a disordered crystal is amorphous or non-crystalline. The lack of long-range coherence leads to higher electron localization. Localization refers to the defined spatial extension of a wave function. Given that in a superconductor, as per Ginzburg-Landau, the entire system can be considered a single electron, and can, therefore, be represented by a single wave function; provided the system is below the critical temperature, the localization of electrons becomes an element that quenches the superconductivity. Localized electrons are described by single wave functions as opposed to the order parameter used to describe the entire system. When there are localized electrons, that is localized charged quasiparticles, there is a Coulombic repulsion associated with them. As a result, an increase in the Coulombic potential occurs as a response to the localization. Higher localization of electrons produces reduced screening and reduced pairing affecting the amplitude of the order parameter. The reason the order parameter is affected is because the emergence of other electrons, other than the one described by the order parameter, implies that the total wave function is no longer the one, but its superposition with the emerging electrons, with

the highest amplitude at the same phase. On the other hand, the phase is affected by dirty bosons. The result is a transition characterized by a sheet resistance made of universal constants, $R_Q = h/(2e)^2$, called the quantum resistance. The quantity is material independent, and temperature dependent [108]. The second mechanism is a magnetic-induced transition via applied fields. The transition in this case is due the presence of both Cooper pairs and vortices in the superconducting phase. Before the transition, there is a condensate composed of Cooper pairs along with localized vortices. The localized vortices are often called "vortex glass." When the sheet resistance R_{sh} is proportional to the quantum resistance R_Q, there is a condensate of vortices and localized Cooper pairs called "Bose glass." Several metallic films act according to the superconductor-insulator transition at the quantum resistance some examples are amorphous Bi [109] and MoGe [110]. However, in some systems there is an intermediate "metallic" state between the superconducting phase and the insulating phase. The metallic state is characterized by a residual resistance below the quantum resistance R_Q at low temperatures [111]. Although there is no consensus to date as to what the mechanism, or reason behind the anomalous metallic state is, there are a few proposed theories attempting to explain it [108]. The first is the tunneling of vortices, wherein the vortex creep through quantum tunneling causes the residual resistance. This first model is in agreement with the metallic state observed in MoGe thin films [112] and ZrNCl in an electric double layer transistor configuration [113]. The second model is the "Bose metal" model, in which conduction via tunneling in a superconducting island array occurs. This metallic Bose state is observed in crystalline $NbSe_2$ bilayer [114] in magneto-transport experiments. Finally, the vortex motion can be induced via an applied field. The vortices can then interact with spinons or vortex metal

leading to a large peak of the sheet resistance R_{sh}. Such behavior was observed in amorphous InO_x films [115].

E. Irreversibility and hysteresis

The nature of the transitions in a superconductor, from metal to superconductor, from superconductor to metal to insulator, and so on, poses a very an interesting question: Are these phenomena dependent on their previous states? In other words, there should be a hysteretic behavior that can be plotted as a function of field and also temperature. There is indeed hysteretic behavior in superconductors as has been already pointed out by Tinkham [116], where the *I*-*V* characteristics of MoGe nanowires with diameters greater than 10 nm were found to display hysteretic behavior due retrapping of currents. Such trapping and retrapping were due to heating effects.

Moreover, hysteretic behavior has also been observed in flux trapping scenarios. Schweitzer's experiments [117] reveal that upon raising the applied magnetic field from zero up to a field higher than the critical field ($H > H_{c1}$) in a superconductor below the critical temperature, the magnetization is no longer reversible. In other words, when the field is lowered again to zero there is a residual flux of $+4\pi M$, which they call the trapped flux. The plot of such event is a hysteresis loop of magnetization vs applied field. In a two-dimensional specimen, the magnetic moment, and, thus, the magnetization is highly dependent on the area of the sample. Hysteresis in a type-II superconductor arises due to the induced supercurrents to counter the applied field. The Bean critical current model [118] is a simple yet powerful way of describing the phenomenon. In a type-II superconductor, there is a supercurrent that is induced called the bulk supercurrent; this current comes from the vortex gradients formed from the surface to the inside, when the

field is increased, and from the inside towards the surface, when the field is decreased. By Ampere's law, there must be a current that is induced in the presence of a field gradient. As a result, a supercurrent flowing on the surface to counter the applied field is induced. Furthermore, in the presence of a varying, AC, field, the supercurrents induced change their direction based on the changing field, in different layers. However, when the field is reduced to zero the currents flowing in different directions cancel each other out. However, some layer has the original supercurrent, thus, contributing to a remaining magnetization that can only be zeroed out by applying a field in the opposite direction. As a result, the increasing and decreasing of a varying magnetic field produces a hysteresis loop similar, in behavior, to that of a ferromagnetic material. Nevertheless, unlike a ferromagnetic material, the magnetization does depend on the size of the material [119]. The width of the hysteresis loop can be used to measure the magnetization current, and, thus, the critical current of the system.

In terms of graphite only, irreversible behavior is known to occur. Hysteresis in the thermomagnetic magnetization and magnetoresistance are evidence of superconductivity in graphite. The measurement of magnetoresistance in graphite samples showed a negligible change when the field was directed parallel to the interfaces, but it displayed an increase when the field was applied perpendicular to the basal (*c*-axis) plane. The measurements showed an anomalous response explained by highly anisotropic granular behavior as opposed to the formation of magnetic domains.

Regarding magnetization measurements, the importance of removing the diamagnetic background from the rest of the sample is key to having good measurements. The magnetization hysteresis is observed between the field -cooled and the zero field-cooled

curves. The appearance of anomalous magnetization and magnetoresistance only when the field is directed perpendicular to the basal plane is evidence of superconducting regions having transitions and not of magnetic ordered being introduced in the material [120]. More recent studies [121] have found hysteresis loops in the magnetization curves of reduced graphene oxide (r-GO) consistent with type-II superconductivity, wherein the size of the hysteresis loop is quenched by the application of higher magnetic fields.

The previous hysteretic characteristics of a type-II superconductor occur when varying the fields. However, hysteretic behavior occurs when there is a variation in the temperature as, in a Nernst effect context, the vortices will appear, diffuse, freeze on a cooling cycle, and then melt, diffuse, and eventually disappear at temperatures higher than the critical temperature [122]. Therefore, within the critical region and appearance of vortices, the Nernst signals should also have hysteretic behavior.

Table 2. Symbols and Acronyms

Symbol/Acronym	**Description**	**Numerical Value**
BCS	Bardeen-Cooper-Schrieffer	-
T_c	Critical temperature	-
Δ_{sc}	Superconductor energy gap	-
k_B	Boltzmann constant	1.381×10^{-31} kg $s^{-1}K^{-1}$
Θ_D	Debye temperature	-
U_{e-ph}	Electron-phonon interaction	-
$DOS(E_F)$	Density of states	-
λ_L	London penetration depth	-
ξ	Coherence length	-
κ_{GL}	Ginzburg-Landau parameter	-
ϕ_0	Magnetic flux quantum	2.0678×10^{-15}Wb
h	Planck's constant	6.626×10^{-34} m^2kg s^{-1}
e	Electron charge	1.602×10^{-19} C
$\boldsymbol{v_\phi}$	Vortex velocity	-
$\boldsymbol{F_p}$	Pinning force	-
$\boldsymbol{B}$	Magnetic field	-
$\boldsymbol{J_c}$	Critical current density	-
n_s	Superconductor carrier density	-

γ	Damping coefficient	-
$\boldsymbol{j_n}$	Normal current density	-
$\boldsymbol{S_\phi}$	Entropy per vortex	-
μ_T	Total potential	-
$\mathcal{E}$	Electric field	-
μ_{ch}	Chemical potential	-
μ	Electronic mobility	-
σ_{xx}	Longitudinal conductivity	-
l_{mfp}	Electron mean-free path	-
λ_F	Fermi wavelength	
α_{xx}	Longitudinal thermoelectric coefficient	-
Λ	De Broglie wavelength	-
σ_{xy}	Transverse conductivity	-
ϕ_p	Flux per particle	-
l_B	Magnetic length	-
S_p	Transport entropy per particle	-
YBCO	yttrium barium copper oxide	-
LSCO	Lanthanum Strontium Copper Oxide	-
$\tilde{S}_{vortex}$	Entropy per vortex	-
$\mathcal{N}$	Nernst coefficient	-

ρ_{ff}	Flux flow resistivity	-
V	Volt (unit of electric potential)	-
BKT	Berezinskii-Kosterlitz-Thouless	-
T_{BKT}	BKT temperature	-
Si	Silicon	-
Nb	Niobium	-
Tl	Thallium	-
Pb	Lead	-
QPT	Quantum phase transition	-
SIT	Superconductor-to-insulator transition	-
R_Q	Quantum resistance	6455 Ω
R_{sh}	Sheet resistance	-
Bi	Bismuth	-
MoGe	Molybdenum-Germanium	-
ZrNCl	Zirconium nitride chloride	-
$NbSe_2$	Niobium diselenide	-
InO_x	Indium-Oxygen compound	-
H_{c1}	First critical field	-
r-GO	Reduced graphene oxide	-

IV. TWO-DIMENSIONAL AND LAYERED SUPERCONDUCTORS

A. Granular and crystalline superconductors.

The first thin film superconductors were lead and tin thin films in 1938 [108]. Given that the deposition techniques in those days were limited to quenched condensation, the films resulted in low-dimensional highly granular and amorphous structures. The granular structures in the films are weakly coupled. As a result, Coulomb interactions become more relevant in the material. The Coulombic energy that needs to be overcome for electron transfer, from grain to grain, is given by $E_c = e^2/2C_g$ [123]. Where e is the electron charge and C_g is the grain's capacitance. The Coulombic interaction between grains due to lack of electrical coupling works to diminish a long-range coherent order and as a result superconductivity. Nevertheless, the Josephson energy is also present attempting to overcome the Coulomb repulsions and establish long-range coherence. The Josephson energy is given by $E_J = \phi_0 I_c$, where ϕ_0 is the quantum flux and I_c is the critical current. Another effect arising from the weak inter-grain coupling is the acquisition of an individual order parameter per grain. The order parameter, for a granular system is given by $\psi_k \, e^{i\theta_k}$ where ψ_k and θ_k are the amplitude and phase of the order parameter at the kth grain, respectively. The critical temperature of granular systems does not vary significantly with the reduction of thickness [124].

Improvement in growing techniques has led to homogeneous film growth. Although, not completely crystalline, this stage represents a middle ground between highly crystalline and granular films in terms of disorder. These types of films have electrically coupled nanocrystals. Film materials include lead, indium and some nitrides such as TiN, among

others. A special characteristic of homogeneous films is that topologically they are considered two-dimensional; however, their wavefunctions are still three-dimensional since their mean-free path is smaller than their thickness. There are two effects that play key roles in the superconductive properties of the films. First there are Coulomb interactions due to the well-coupled nanocrystals [125]. Coulombic or fermionic repulsions arises from disorder introduced by reducing dimensionality. As a result, scattering is increased, and screening is reduced. A second effect relevant to homogeneous films is Anderson localization, wherein electron wave functions are localized within a specific length called the localization length l_{loc} [126]. This type of localization, also known as strong localization, contributes to Cooper pair formation given the overlap of wave functions within the localization length. Full Cooper pair formation can be expected, ideally, if Coulombic repulsions are not present, and the localization occurs in a single and isolated grain. However, in a real case scenario both effects are present and interact in a complex manner.

The increase of disorder in homogeneous films, and quenching of superconductivity, is often measured by the product $k_F l_{mfp}$ reaching unity [100-103]. The Fermi vector is represented by k_F while l_{mfp} is the electron mean-free path. This situation in homogeneous films is reflected in the more "granular" behavior of its superconductive properties. It was found via scanning tunneling spectroscopy on a TiN film [99] that at low temperatures the superconducting gap has spatial variations greater than the coherence length. Several efforts in homogeneous films are concentrated on the effects of the nanocrystal distribution on the disorder potential in the film and whether they are responsible for the "granularity" at low temperatures.

The use of molecular beam epitaxy (MBE) techniques at ultra-high vacuum allows for the fabrication of less disordered films. Films grown at ultra-high vacuum display a weakly disordered as well as crystalline structure [125]. As a result, for a specific thickness, the films present homogeneous properties. The superconducting properties, however, are highly dependent on thickness unlike granular films. Various studies using STS and magnetometry show a strong conventional BCS behavior of the density of states [127,128]. Moreover, a significant reduction of the coupling constant becomes apparent below 10 monolayers [129], a monolayer being approximately 0.3 nm thick. As a result, the critical temperature and the energy gap are reduced with thinner films. There is still considerable uncertainty around the issue of thickness in crystalline films. Quantum size effects, such as quantum confinement near the Fermi energy could be a contribution [130]. The vertical confinement varies as the thickness is adjusted. Consequently, there is a change in the film's chemical potential which, in turn, affects the critical parameters.

The quantum size effects on thin crystalline films are mostly a consequence of oscillations around the critical temperature. There is, however, a discrepancy between experimental scanning tunneling spectroscopy (STS) measurements on conventional BCS films and theoretical density functional theory (DFT) calculations often lie in the type of function or trend followed. Previous experimental work determines that the fluctuations are discontinuous gaps or jumps due to the discrete values of the density of states [131,132]. On the other hand, calculations [133, 134] show that the critical temperature follows a smooth behavior as a function of thickness. Both approaches, theoretical and experimental, do agree on the same principle: the adjustment of the chemical potential must correspond with the thickness.

B. Interface superconductors and electrostatic doping

The use of paraelectric and ferroelectric materials such as strontium titanate ($SrTiO_3$), barium titanate ($BaTiO_3$) and lithium niobate ($LiNbO_3$) as a substrate has been applied to increase the critical temperature T_c of some superconductors such as yttrium barium copper oxide ($YBa2Cu_3O_{7-\delta}$ or YBCO), a well-known high-temperature superconductor, films at different thicknesses [135,136]. This observation has been mainly due to the introduction of crystalline defects into YBCO when deposited onto the ferroelectric substrate as well as the effect of polarization fields on the charge carrier density.

Ferroelectric materials are characterized by a spontaneous polarization without being under the effect of an external electric field. In general, they tend to have dielectric constants orders of magnitude larger than those of standard dielectrics [137]. Their atomic structure, more specifically, their relative position of their ions allows for the formation of dipoles that can be redirected by an eternal field and will remain polarized after the field is removed. An example of such structure is that of barium titanate, $BaTiO_3$, where the positive titanium ion and the negatively charged oxygen ions form a dipole. Ferroelectric structures like barium titanate, often perovskite oxides, owe their stability to the highly hybridized titanium 3d states and oxygen 2p states [138].

Ferroelectric materials can be used in the form of thin films. At the scales encountered in thin films the ferroelectric properties of the thin films are significantly influenced by their interaction with the substrate. Moreover, internal strain and fatigue have a stronger effect on the electronic properties of thin films than in their bulk counterparts. Nevertheless, due to the symmetry inversion center of perovskites the main contribution to the polarization

effect is due the polarization itself and note the strain generated [139]. A thin film ferroelectric material in contact with a superconductor will have its internal and intrinsic polarization field screened by the free carriers from the superconductor. As a result, the charge density at the interface will change and there will be a bending in the energy bands of the superconductor. The bending of the bands causes a potential within the system in which carriers are either attracted or repelled depending on the polarization direction and excess carriers found in the material. Consequently, a tuning of resistance and charge density can be developed in a heterostructure of superconductors and ferroelectrics.

The effect of electric fields induced due to polarization in ferroelectric materials has a significant effect in bilayer and trilayer structures of superconductors on ferroelectric substrates. In the case of the bilayer structures, the polarization at the interface can have a similar effect on the superconductor to that of doping by either attracting or repelling the charge carriers. High-temperature superconductors have interesting properties that have been exploited with the use of ferroelectric materials. Such properties include low charge densities and low coherence length [140]. The effects of ferroelectrics on high-temperature superconductors (HTSs) can be larger than those of low temperature superconductor materials as their critical temperature shift only accounts for 0.1 K. The critical temperature shift was found to be around 1 K in some of the early experiments on HTSs [141-146], while as high as 6 K in other works [147,148]. The smaller temperature shift is also due to the external field applied to generate more polarization. However, results of 100 nm YBCO thin films on $BaTiO_3$ arranged as a gated device with the use of polarization field, instead of external field, show a shift of 0.5 K in the transition temperature with the polarization directed away from the YBCO film [149]. Even though the change in critical temperature

is not so significant, several other studies have shown that YBCO/ $BaTiO_3$ structures in fact increase the critical current of the superconductor considerably [136]. This effect is mainly due to the $BaTiO_3$ particles in the YBCO acting as artificial pinning sites. Over the course of research on ferroelectric structures, higher temperature shifts have been obtained. Measurements include a shift of 7 K to 9 K of the *Tc* of gadolinium barium copper oxide (GBCO) on lead zirconate titanate and neodymium barium copper oxide (NBCO) [150,151], and as high as 30 K on YBCO on a bismuth ferrite ($BiFeO_3$) substrate [152].

Moreover, more pronounced and significant changes occur in the use of $LiNbO_3$ as a substrate on YBCO. The change in critical temperature due to internal polarization in the same gated device configuration is around 40 K [153]. Spontaneous polarization of a ferroelectric substrate, such as PZT, when in contact with HTS thin films in a bilayer structure have shown shifts in the critical temperatures. This effect is attributed to both the polarization as a doping-like effect on the charge density at the interface and the introduction of pinning sites during the growing of the HTS films.

On other hand, the effect of $SrTiO_3$-thin film superconductor-$SrTiO_3$ structures, a trilayer system, has to do with the modification of the internal charge distribution in the film, thus, increasing the superconducting transition temperature [154]. Contrary to a bilayer system, where the polarization of the ferroelectric substrate effectively repels the charge carriers to provide a doping-like effect, the trilayer system will allow screening of polarization field on either side of the superconductor. As a result, the structure and behavior of the carriers is affected throughout the film and not on one surface. This screening throughout the superconducting film allows for a complete redistribution of charge within it. The way it is distributed permits charge accumulation in the superconductor and; therefore, a higher

probability of Cooper pairing at higher temperatures. As a result, higher critical temperatures and resistive transitions can be expected [148].

C. Cuprate Superconductors

Cuprates are structures related to Perovskites that have alternating copper oxide (CuO_2) layers and weak coupling in the normal direction. The CuO_2 are the conducting layers while the ions on top, or bottom, act as electron reservoirs [155]. This fact is alone interesting since conductivity takes place in the transition metal layers instead of oxygen as in other oxides. The conduction is driven by the small energy difference between the metallic bands and the oxygen bands. Cuprates have an unfilled orbital (dx^2-y^2) which would contribute to a metallic behavior; however, cuprates are electrical insulators with strong electron interactions [156].

Cuprate superconductors have short coherence length, in the order of 0.1 nm, resulting in high sensitivity to local effects such as grain boundaries and other defects. Pressure acts positively in these superconductors as it brings the CuO_2 planes closer together.

Cuprate superconductors have less isotope effect. In a conventional superconductor, as described by the BCS theory, the critical temperature decreases as the atomic mass of the element increases. The decrease in critical temperature is inferred by phonon softening due to the heavier atomic mass. For that reason cuprate superconductors are thought to have a different pairing mechanism than that of conventional superconductors.

Some cuprate superconductor families are: The lanthanum family, discovered in 1986 [157]. The formula of such materials is $La_{2-x}Ae_xCuO_4$. Ae is an alkaline earth metal, often being calcium, barium or strontium. They have a tetragonal structure similar to Perovskites, and their highest critical temperature is 37.5 K.

The most known, and widely used high-temperature cuprate is yttrium barium copper oxide (YBCO). The superconductor was discovered in 1987 with the first critical temperature measured at 97 K; it was the first superconductor to exceed the liquid nitrogen temperature [158]. YBCO has an orthorhombic symmetry often described as an oxygen deficit Perovskite.

The same year the BSCO superconducting structure was discovered [159]. These materials have critical temperatures ranging from 7 K to 22 K; however, adding calcium to form the $Bi_4Sr_3Ca_3Cu_4O_{16}$ increased the critical temperature to 85 K. The highest critical temperature in this family is 110 K, achieved by the compound $BS_2C_2C_2O_3$ in bulk form. The latter structure is often preferred in applications due to its stability when in contact with oxygen and flexibility. Another cuprate is the thalium-based $TlBa_2Ca_{x-1}Cu_xO_{2x+3}$ discovered in 1988 [160], characterized by a critical temperature that depends on the oxide thickness, high critical parameters and a tetragonal structure.

Cuprate superconductivity is a phenomenon that is still not well understood. The most widely believed mechanism is the diminishing of magnetism in the material due to hole doping.

D. Iron-Based Superconductors

Iron-based superconductors were discovered by Hideo Hosono's group in 2006 [161,162]. The first critical temperature was 4 K and eventually it was increased to 26 K. This discovery was accepted by the community with surprise given that it was widely believed that materials with high magnetization or magnetic moment would not be able to generate Cooper pairs.

The first type of Fe-based superconductors is the 1111-family, which consists of ZrCuSiAs-type crystal structures. These compounds consist of anti-fluorite or tetrahedron Fe_2Pn_2 layers with fluoride layers stacked alternately. Here Pn refers to pnictides or elements from the group 15 in the periodic table, more specifically arsenic and phosphorus. At the time of discovery they had a critical temperature of 26 K which then was increased to 55 K [162]. The source of superconductivity in these films is the systematic doping of fluorine. It has been noticed that the diminishing or absence of antiferromagnetism in the film by changing its structure or by carrier doping, fluorine in this specific case, is key to onset superconductivity [161].

The first 1111-systems, specifically the phase LaFeAs(O,F), were grown using pulsed laser deposition (PLD). The key to growing the La1111 phase is the growth of the LaOF seed which is difficult in PLD since the growth takes place in an uncontrollable manner. As a result, the use of a two-step process with PLD was used to obtain the films. This process consists of using a KrF excimer laser at a wavelength of 248 nm in order to deposit LaFeAs(O,F) precursor films. The second step consists of ex situ annealing in an evacuated quartz tube. These films had a critical temperature of 28 K [163,164].

A second representative family is the family of 122 compounds which consists of $(Ae, A)Fe_2As_2$-like structures. They are made of tetrahedron Fe_2Pn_2 layers and alkaline earth layers stacked alternately. Their highest critical temperature has been recorded as 38 K [165]. The importance of these films lies in that antiferromagnetism is not a problem when it comes to affecting the superconductive properties of the films. In other words, they demonstrated that antiferromagnetism can coexist with Cooper pairs.

This family is characterized by the superconductive onset being triggered by the excess of hole carriers or hole dopants, more specifically, on the systematic replacement of potassium in the alkaline earth metal comprising the outer layer of the system [166]. Nevertheless, the introduction of potassium in such systems is a difficult task due to the element's volatility, that is, its instability at high temperatures when it is set to have any absorption tasks. As a result, several changes in the growth in a molecular beam epitaxy system are applied such as lowering the partial pressure of some of the elements used and increasing the temperature of growth, in order to allow for potassium to settle in the alkaline metal site. This is specifically for systems involving $(Ba,K)Fe_2As_2$ and $(Sr,K)Fe_2As_2$.

A third structure is the 11 compounds. These are the FeCh family, where Ch is a chalcogenide or specifically, sulfides, selenides and tellurides rather than oxides [167]. They possess a PbO-type crystal structure that is they are divalent chalcogen ions instead of pnictogen ions. They have stacks of tetrahedral Fe_2Ch_2 layers bonded by the van der Waals interaction. Their critical temperature is low, 14 K, but has been increased to 37 K by applying hydrostatic pressure. Their low critical temperature as well as difficult stoichiometry make them unstable and not desirable for applications [168].

E. Flat bands, Moire patterns and superconductivity in graphene

The knowledge of superconductivity phenomena in carbon dates back to 1965 when measurements in potassium-intercalated graphite showed some superconductivity-like characteristics [169]. In 1974 measurements on annealed carbon powder using aluminum contacts [170] showed a behavior similar to a Josephson-coupled granulated superconductor.

Several transport measurements have provided evidence of granular superconductivity occurring at the interfaces of graphite [171-173]. The most basic measurement, the resistance versus temperature, shows an abrupt increase in resistance regardless of the purity of the sample. In the studies the least "pure" or ideal graphite sample showed a typical metallic behavior while the rest of the samples (higher purity) showed an increase similar to that of a metal-insulator transition. Moreover, the magnetoresistance measured was too big to match the metal-insulator transition for fields as small as 1 kOe. Since the interfaces are well-defined, the metallic behavior is not intrinsic of the graphite layers. The measurements showed the possibility of granular (Coulomb against Josephson) superconductivity in isles embedded within the layers. A more practical way, however, to find out if the isles or interfaces could potentially be superconductive, was to place contacts as close as possible to an interface. The studies used transmission electron microscopy (TEM) to locate the interfaces and ion beam lithography to place contacts at the edges of several interfaces. The *I-V* curves showed a sharp transition at 150 K with an applied current of 100 nA. Increasing the value of the applied current lowered the transition in temperature, which is consistent with Josephson-coupled granulates.

Superconductivity in graphene has been a focus of research for the past few decades. The high mobility, long phonon coherence length, tuning of carrier density and of density of states, by a gate voltage, have led to research into turning graphene into a superconductor. Superconductivity was successfully induced in mechanically exfoliated graphene by means of superconducting Ti/Al bilayer (10/70 nm) contacts [174] wherein a Josephson supercurrent was observed.

Due to the low carrier concentration of graphene and the vanishing density of states toward the intrinsic Fermi level, superconductivity is not thought to happen in undoped graphene. The vanishing density of states does not allow for superconductivity to for, and the low carrier concentration reduces the electron-phonon coupling. As a result, the idea of doping was proposed as a practical solution given that it can increase the carrier density and the density of states near the Fermi level. From a theoretical point of view, a mean field diagram of superconductive graphene was also derived and plasmon mediated superconductivity was also predicted to occur [175]. Moreover, other theoretical works analyzed the use of lithium adatoms systematically applied to the surface of graphene to cover it and enhance the electronic properties. They predicted superconductivity at 18 K [176]. Though it was later tested experimentally [177] and no superconductivity was observed above 1.8 K; the cause of the low critical temperature was credited to the strong confinement of the lithium layers.

Interest in superconductivity research in graphene was renewed by the observation of superconductivity in calcium intercalated graphite at 11.5 K [178]. The research up to that found that the key elements to superconductivity in graphene involved the introduction of adatoms to increase the carrier density and the formation of a superlattice between the graphene layers as to create overlapping of the electron bands. In 2016, robust superconductivity in calcium-intercalated graphene laminates was observed at 4 K [179].

A recent trend in two-dimensional superconductivity is the use of Moire patterns to enhance the electronic properties of graphene. Such patterns involved rotations in the overlapping layers of graphene as shown schematically in figure 11.

From a BCS framework, it is known that increasing the phonon-electron coupling and/or the density of states at the Fermi level increases the critical temperature of a superconductor via its exponential dependence. The density of states is often increased to a maximum by making it diverge. For divergence to occur the electronic bands are made flat. Several methods are used to make electronic bands flatter. The most popular are topological arrangement of the lattice and strain. In the case of bilayer graphene topological flattening of the bands is the method that led to superconductivity by rotating overlapping single layers.

It is well understood that the stacking arrangement influences the band structure and the electronic properties of some materials. In the case of graphene, the addition of layers smears the Dirac cones turning them into parabolas. Moreover, the type of stacking can also contribute to the electronic properties significantly. Few-layer graphene usually presents a Bernal stacking or AB stacking where every other layer is shifted relative to the adjacent ones. Rotational stacking faults in such stacking scheme leads to the decoupling of adjacent layers.

Twisted bilayer graphene (TBG) involves the addition of a layer and the rotation relative to the substrate at an angle of interest. Given that the Dirac points have a repulsive interaction with other Dirac-points at adjacent layers [180], energy gaps develop when placing two graphene unit cells on top of each other. However, rotating them at an angle, and arc length, less than the interdistance of the Dirac points leads to the decrease of the band gap, the increase of the density of states and the unit cell area.

It was found by Landau level spectroscopy and high magnetic field scanning tunneling microscope (STM) that a rotation at an angle less than 2 degrees causes a strong electron

coupling effect, while a higher angle will cause decoupling. [181]. Supercell modulation in a Moire pattern has a strong effect on the electronic properties of certain materials and, as a result, on the critical temperature within a framework of superconductivity [182-183].

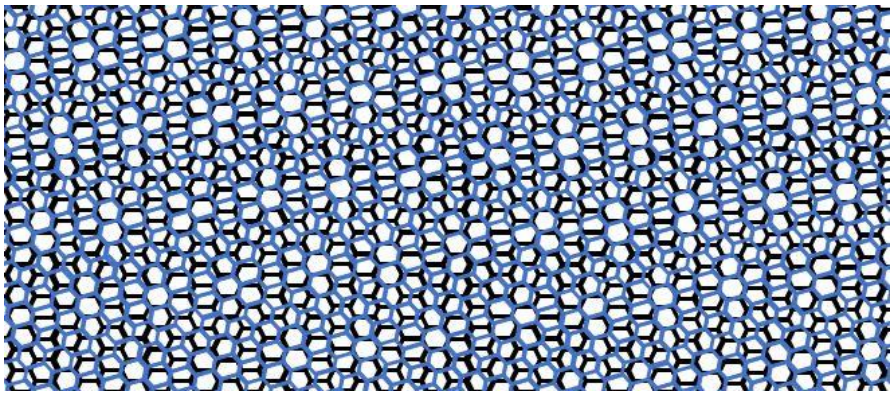

Figure 11 Moire Lattice in twisted bilayer graphene. The schematic shows bigger unit cells created by the overlay of blue on black.

In order to study analytically the effects of superconductivity due to Moire modulation, several models have been used. The Holstein model seems to provide a simple yet clearer picture of what goes on. The Holstein model [184] is characterized by assuming an interaction of phonons as localized particles with free fermions in the lattice with a Hamiltonian given by:

$$\frac{g_{eff}^2}{k}\sum_j n_j \uparrow n_j \downarrow + \sum_j \omega(a_j^\dagger a_j + 0.5) \; + g_{eff}\sqrt{\frac{h}{\pi M\omega}}\sum_{j,\sigma} n_{j\sigma}(a_j^\dagger + a_j)$$

where k is the electron momentum vector, n_j is the Fermion density at j; the electron occupation number is given by $n_{j\sigma} = c_{j\sigma}^* c_{j\sigma}$ where $c_{j\sigma}^*$ and $c_{j\sigma}$ represent fermion creation and annihilation at j, respectively; and $a_j^\dagger a_j$ are the phonon creation and annihilation operators. In other words

Moire superconductivity within the Hubbard-Holstein model is useful when studying different levels of interaction. One interaction is at the Moire unit cell level in the region seen in figure 12.

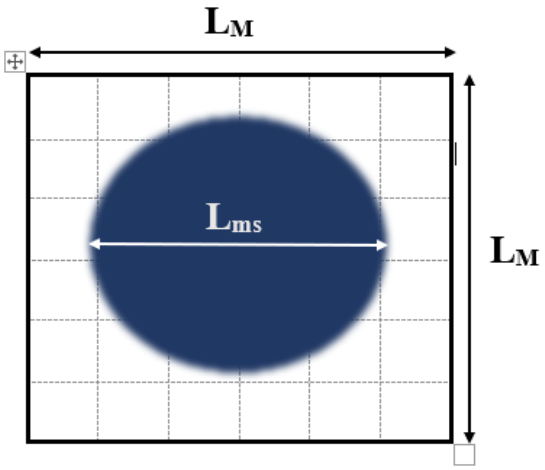

Figure 12 Schematical representation of a Moire unit cell of side length L_M, microlattice (dotted line) and phonon density with spread Lms

An electron in a Moire cell can be in N atomic sites; that is, it can be part of a cloud of electrons in any of the N_a atoms present at the given Moire cell. Assuming a weak Moire potential then the electrons present would then interact with the same number of phonons $N_a = N_{ph}$; the common assumption being that only longitudinal phonons contribute to Cooper pairing. However, in a stronger Moire potential there is only a fraction of electrons interacting with the phonons. This quantity amounts to only one electron per number of phonons in the cell or $1/N_{ph}$. Plugging the inverse term in the electron-density interaction portion of the Hamiltonian leads to $g_{eff}^2 n_j^2 / 2kN_{ph}$ for a single electron.

Although, the model would show a reduction of the electron interactions (inverse term) in each microscopic band making up the Moire cell, there is an increase in the density of states

at the Moire level when summed up in the Hamiltonian. The increase leads to a higher coupling coefficient U_{e-ph}, which leads to an effectively unaffected superconductivity state [185].

In a case where the potential is studied over a finite width of the electronic band, as opposed to the individual unit cells, the potential is smooth and has a bandwidth equivalent to the Moire cell length times the lattice constant of the material, that is $L_M * a_L$. In this case, the potential is strong enough to cause the wavefunction concentration to be near the minima of the potential. As a result, the number of electrons interacting with phonons is much smaller than the total number of electrons in the Moire cell, that is $N_e < N_M$. Nevertheless, the electron-phonon interaction coefficient is still enhanced by the Moire cell. Finally, in taking into account the Coulomb interaction in the lattice, the renormalization still shows no enhancement of the unscreened Coulomb potential in either long- or short-range interactions [186]. As a result, the Moire cell can effectively suppress the enhancement of unscreened Coulomb potentials while enhancing the density of states and, thus, superconductivity.

The Holstein model is a qualitative tool that encompasses the general behavior in a twisted bilayer graphene sample without much use of detailed physics. From the model several conclusions can be drawn that match their experimental counterparts: First, there is an enhancement in the density of states as well as the coupling coefficient whenever superlattice modulation is applied in a bilayer graphene system. Moreover, the softening of phonons in such systems enhances the possibility of phonon-electron coupling. Nevertheless, an enhancement in U_{e-ph} does not necessarily imply an enhancement in the population density. The rather low electron density has negative effects on

superconductivity as it is the driving factor in the BKT transition. Such effects include, low and bounded T_c as well low critical current.

Experimentally, Moire superconductivity in twisted bilayer graphene can be measured with the use of a Hall bar geometry. Cao et al [187] studied TBG on a Hall bar where the twisted bilayer graphene was etched onto as seen schematically in figure 13. The contacts were made from evaporated chromium to avoid proximity effects and superconducting transitions going into the Chromium. A gate voltage was applied to a gold electrode placed at the bottom to modify the carrier density. Superconductivity in such device is found at temperatures of 1.7 K and 0.5 K for angles of 1.16˚ and 1.05˚, respectively. The transition occurs when the Fermi energy is moved from E = 0 towards the half filing lower band. No results were observed for gate voltages tuning the Fermi label towards the conduction bands. The flat valence band in the twisted bilayer system has some interesting effects. The density of states was almost 3 orders of magnitude higher than the uncoupled layers. Mostly, this was due to the increased localization and drop in Fermi velocity. Other effects related to superconductivity can also be observed. A BKT transition also occurs at this temperature. More specifically, at 1 K with a carrier density of 1.44×10^{12} cm^{-2}. BKT was inferred from data fitting where the longitudinal voltage V_{xx} is proportional to the cubed current I^3.

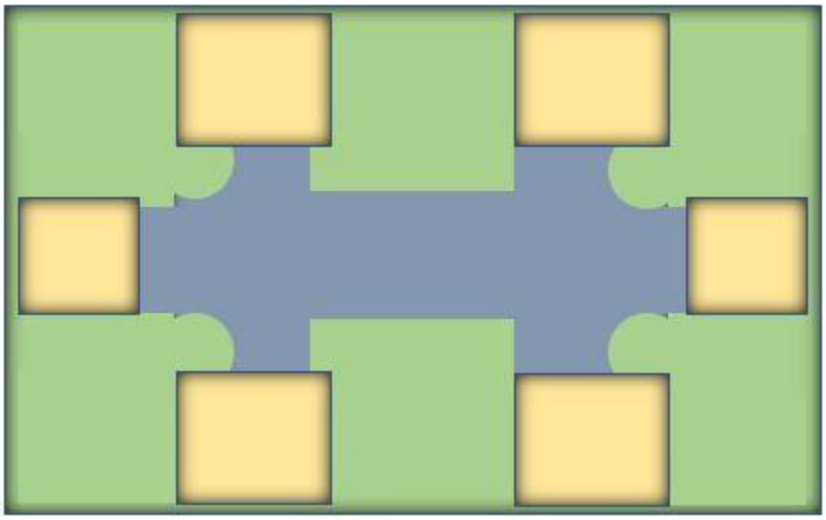

Figure 13 Hall bar fixture

The same Hall set up under the applications of a magnetic field perpendicular to the sample can have significant properties. Although at such small temperature the application of a field can quench superconductivity due to the vortices and disorder introduced by it [140]. Cao et al. found that the application of a perpendicular field created oscillations in the critical parameters near the Mott-like insulating state [181]. Similar to superconducting quantum interference device (SQUID) -like superconductors, the oscillations seem to come from arrays of Josephson couplings. Most likely due to imperfections in the measuring device as the critical parameters get suppressed gradually by the field eventually. Moreover, the temperature dependence of the perpendicular critical field is well understood via Ginzburg-Landau theory [188] the in-plane critical field is not. As a result, the dependence is often attributed to paramagnetic pair-breaking due to the Zeeman energy [181]. Though, the transitions are not abrupt, the results by Cao et al do show characteristics of two-dimensional superconductivity driven by a crossover of Bose-Einstein condensate and BCS conventional states.

Other experimental efforts [189] have found similar results as Cao et al, including insulating transitions at the same angles. Yankowitz et al have also found a clear relation between the carrier densities involved in the process. At half filling, that is $n_s/2$, is where the superconductive state can be narrowed down in the measurements. Moreover, the superconductive transition occurs near the insulating transition. Given the timing of the onset of superconductivity with the appearance of quantum oscillations, it can be suggested that a small Fermi surface with lower degeneracy was formed. These Fermi surfaces are nucleated only at half filling as other fillings observed did not caused superconductivity.

Several theoretical and experimental efforts have yielded similar results and conclusions about the use of Moire superlattices in bilayer graphene. There are advantages of using graphene due to high mean-free path, coherence length and Debye temperature. Those aspects in graphene along with the large density of states created by electron doping and the twisting at the "magic angle" are key to introduce electron interaction and, thus, superconductivity. Nevertheless, some issues do exist in the way interactions occur. A high level of confidence is being given to superconductivity relying on flat bands for Cooper pairing. Since the formation of Cooper pairs is a very fast event, essentially at timeframes inverse to phonon frequencies, a flat band is not required for electron-electron interaction. Moreover, the coherence in graphene is reduced due to the localized increase of the density of states at the Moire unit cells. Evidence of this, among other traits, can be observed in the low critical temperatures in the vicinity of 1.7 K.

Table 3. Symbols and Acronyms

Symbol/Acronym	**Description**	**Numerical Value**
E_c	Coulomb energy	-
C_g	Grain capacitance	-
E_J	Josephson energy	-
I_c	Critical current	-
ψ_k	Kth order parameter amplitude	-
θ_k	Kth order parameter phase	-
TiN	Titanium nitride	-
l_{loc}	Localization length	-
k_F	Fermi vector	-
l_{mfp}	Electron mean-free path	-
MBE	Molecular beam epitaxy	-
STS	Scanning tunneling spectroscopy	-
DFT	Density functional theory	-
$SrTiO_3$	strontium titanate	-
$BaTiO_3$	Barium titanate	-
$LiNbO_3$	lithium niobate	-
YBCO	yttrium barium copper oxide	-
HTS	high-temperature superconductors	-

NBCO	neodymium barium copper oxide	-
	bismuth ferrite	-
GBCO	gadolinium barium copper oxide	-
PZT	Lead zirconate titanete	-
PLD	Pulsed laser deposition	-
ZrCuSiAs	Zirconium Copper Silicon Arsenide	-
Fe_2Pn_2	Iron pnictide	-
LaFeAs(O,F)	Fluorine-doped lanthanum iron oxyarsenide	-
LaOF	Lanthanum oxyfluoride	-
KrF	Krypton fluoride	-
$Fe_2\ As_{2-}$	oxypnictide	-
Ae	Alkaline earth metal	-
A	Alkaline	-
FeCh	Iron chalcogenide	-
kOe	Kilo Oersted	79577.47 A/m
TEM	transmission electron microscopy	-
I-V	Current versus voltage	-
TBG	Twisted bilayer graphene	-
STM	scanning tunneling microscope	-
g_{eff}	Electron-phonon effective interaction	-

$c_{j\sigma}$	Fermion annihilation operator	-
$c_{j\sigma}^{*}$	Fermion creator operator	-
$a_j^{\dagger}$	Phonon creation	-
a_j	Phonon annihilation	-
N_{ph}	Number of phonons	-
N_e	Number of electrons	-
U_{e-ph}	Electron-phonon coupling coefficient	-
V_{xx}	Longitudinal voltage	-

V. EXPERIMENTAL METHODS

A. Sample preparation fundamentals:

i. Ion Implantation

Ion implantation is a processing technique used to change the structure of a material beyond the surface by using ions as projectiles to impinge and implant. The use of ion energies of hundreds of keV allows for the effective implantation of ions at thousands of angstroms under the surface. As a result, ion implantation is a widely used technique for doping. The basic process of implantation consists of ionizing the atoms of the dopant before accelerating them with a voltage to target a wafer. A gas is often used as a source of dopant, which is turned into a plasma by applying a current. The application of a voltage to a grid, allows for the ionized gas to accelerate through the grid. The ionized atoms pass through a mass spectrometer that bends the path and allows only a beam of the needed atom to pass onto the substrate. Typical doses range from 10^{12}-10^{16} cm^{-2} [190] An Annealing process might be needed afterwards, depending on the application, to restore the crystallinity of the material.

There are two types of ion implantation energy losses. The first is the losses due to Coulombic interactions between the surface electrons on the substrate and the ions being accelerated at it. The Coulombic loss results in ionization of the surface leading to photons and Auger electrons. The second type of loss, after the electrons incurring Coulombic losses, is the nuclear type. The nuclear losses are due to the collision of the atoms from the ionized gas coming into contact with the surface. The result is a displacement of some atoms on the substrate due to the incoming atoms setting into the lattice. The losses, or

"stopping" forces, have values in the range of 5-10 eV/0.1 nm and 10-100 eV/0.1 nm for electronic and nuclear losses, respectively.

The modeling, as a function of distance, of the events in ion implantation are of statistical nature. The reason behind the statistical nature of ion implantation is that the ions deviate from their entry point as a result of the collision and stopping forces acting on them up entry. The model of such distribution is Gaussian in nature and depends on the dose of ions ϕ_{ion} given by:

$$\phi_{ion} = \frac{Q_{dep}}{nqA}$$

Where Q_{dep} is the deposited charge per unit area A, q is the ion charge and n is the number of charges in the gas. The Gaussian model is, however, not perfect as structural modifications can occur that are not accounted for by the model.

There are some important phenomena that can alter composition. The first is channeling. It is a phenomenon in which the range of penetration of the ion beam is extended due to the lack of nuclear collisions along a particular crystallographic direction. A second type of change is the mixing of atoms from the thin film to the substrate due to high-energy beams; this is known as ion-beam mixing. A more abrupt structural change occurs with the change of coherence in the film. In other words, at a high enough dose of ions the film can become amorphous, assuming an initial crystalline film.

ii. Mechanical exfoliation

Mechanical exfoliation of graphite is the most popular form of producing graphene due to its simplicity and low cost [191]. Mechanical exfoliation of bulk highly-oriented pyrolytic graphite (HOPG) has its roots in the use of the atomic force microscope (AFM) to cleave

the layers, use of chemical vapor deposition to place a mask of SiO_2, removing the mask and rub against a substrate to transfer graphene islands onto the substrate. Nevertheless, the process is difficult to control. Novoselov and Geim [192] are credited as being the first to use adhesive tape to exfoliate graphene from HOPG bulk; this method was the beginning of the wide used of graphene. The idea of Novoselov and Geim is to use adhesive (they used Scotch tape), press it onto the HOPG and gently peel off graphite layers from it. The process is then repeated from the adhesive, by folding and unfolding the adhesive onto itself, in order to obtain thinner and thinner layers progressively, until the layers turn from a shiny color to a dull one. Finally, the tape is place in a solution of acetone along with a silicon wafer; the wafer is then cleaned with propanol, leaving the exfoliated flakes attached to it [2].

B. Previous experiments on phosphorus-doped graphene.

Previous work has shown evidence that suggests a transition to the superconductive state in phosphorus-doped HOPG and graphene [193-196]. Such evidence includes a drop in dc resistance (figure 14) at low temperatures, though not to zero, and the quenching of the transition when a magnetic field is applied seen in figure 15.

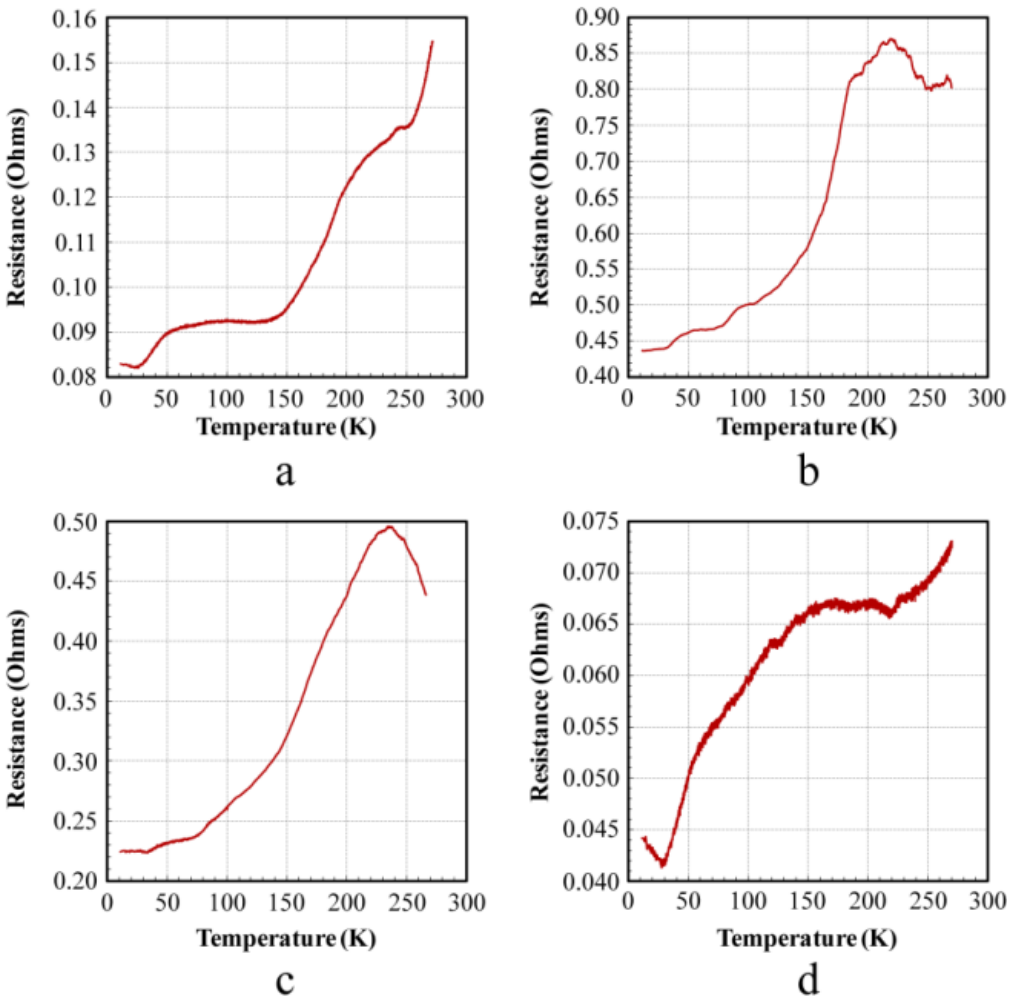

Figure 14 *R* versus *T* curves of 4 exfoliated phosphorus-doped HOPG samples. Implantation energy was 10 keV, dose 1.2×10^{8} cm^{-2}) [196].

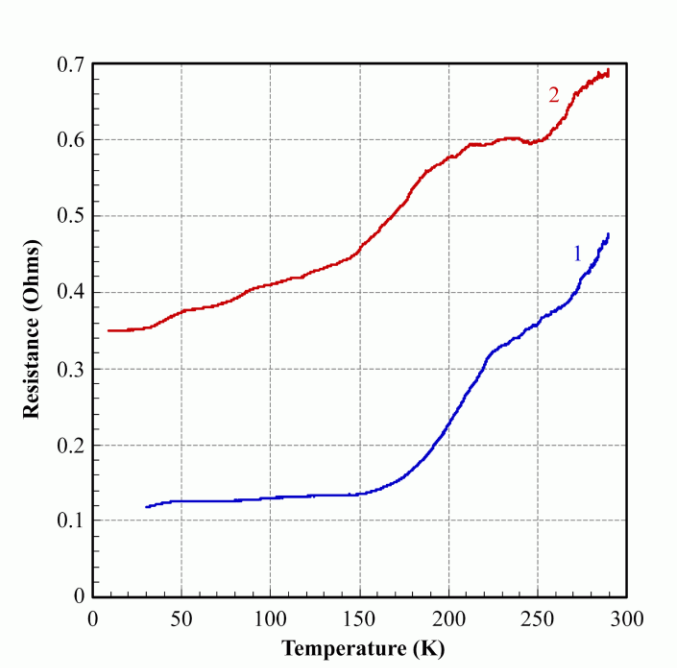

Figure 15 *R* vs. *T* curves of exfoliated phosphorous-doped HOPG without applied field (1) and with 0.035 T of applied field (2) [196].

Due to the high anisotropy of graphene as well as its layered nature, it was hypothesized that flux flow resistance was the cause of the resistance and its step like features. The appearance of "steps" in the resistance versus temperature curves also suggests the presence the melting of the vortex lattice at different temperatures. The steps did not depend on how the material was doped. Furthermore, magnetization and susceptibility measurements have also shown behavior consistent with two-dimensional superconductivity: There is a hysteresis loop in the magnetization measurements is not due to ferromagnetic or anomalous ferromagnetic effects due to the lack of ferromagnetic atoms in graphene. Moreover, the negative magnetization measurements at low field reinforce the notion of graphene not being a ferromagnetic material as seen in figure 16. Yet another sign of superconductivity is found in the change of sign in the Hall voltage, which is a known feature of mixed-state superconductivity [197-199].

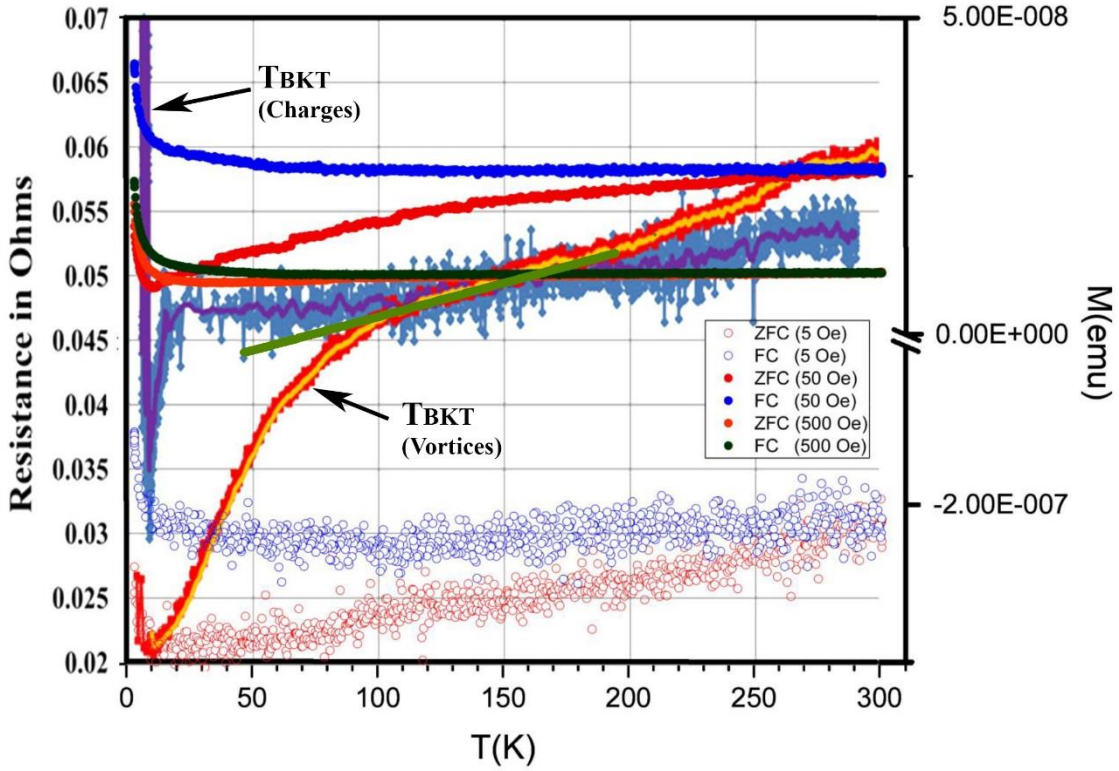

Figure 16 Overlay of magnetization and transport measurements in phosphorus-doped graphene. The susceptibility measurements were made by Dr. Deng from Dr. Paul Chu's group at the University of Houston. There is a clear hysteresis loop opening at 250 K in the zero field and field-cooled curves. The resistance measurements corresponding to the 5 Oe measurement (red with yellow) show a drop in resistance at a low field, while the other transport curve (dark blue on light blue) does not show the drop when higher fields are applied. [204].

The evidence shown suggest the presence of vortices, and, thus, of mixed-state superconductivity. The fact that graphene is a material with high anisotropy also suggests that the formation of pancake vortices as a more favorable energetic mechanism is present. Those measurements alone are not enough to prove the presence of vortices. As such, the Nernst effect was also used to show vorticity and mixed-state superconductivity in phosphorus-doped graphene. It is important to note here that there are other methods of detecting vorticity such magneto-optic imaging, scanning Hall probes, scanning SQUIDS, among others [200-202]. However, in two-dimensional and quasi-two dimensional

materials the vortices might contain more than one flux quanta rendering the methods difficult to use [203].

The work by Sornkhampan et al [204,83] showed that there is indeed vorticity in phosphorus-doped graphene, as quite large structures that resemble classical Nernst peaks were measured at temperatures near 35 K (as shown in figure 17). Smaller “Nernst” peaks were also measured at higher temperatures, leading to the conclusion of smaller vortex stacks being melted at such temperatures. Figure 18 shows clear hysteresis coming from the cooling and warming measurements of the Nernst experiments. The transverse voltage in such Nernst measurements was found to “pick up” the same value at which it was measured without finishing the cycle; a clear indication of hysteretic behavior. As a result, a series of cyclic measurements were planned and performed in order to plot the hysteresis caused by the freezing and melting of the vortex lattice in graphene.

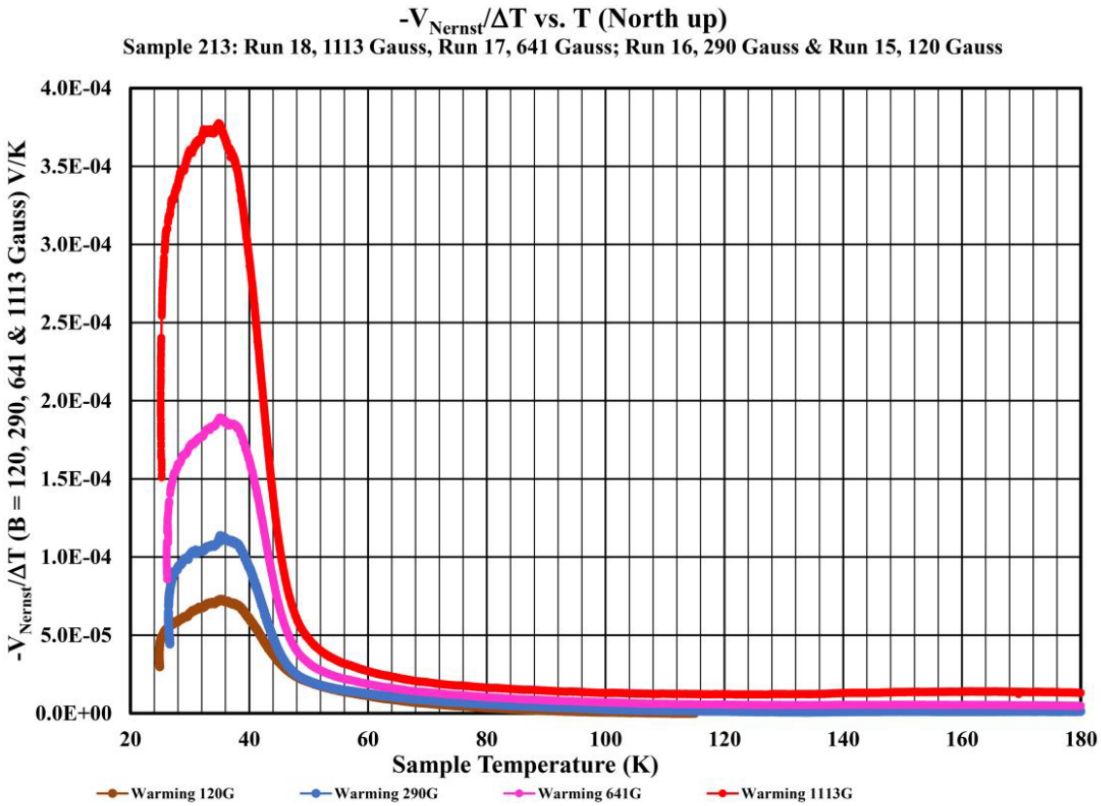

Figure 17 Nernst peaks from 20-180 K. Warming cycles only [83].

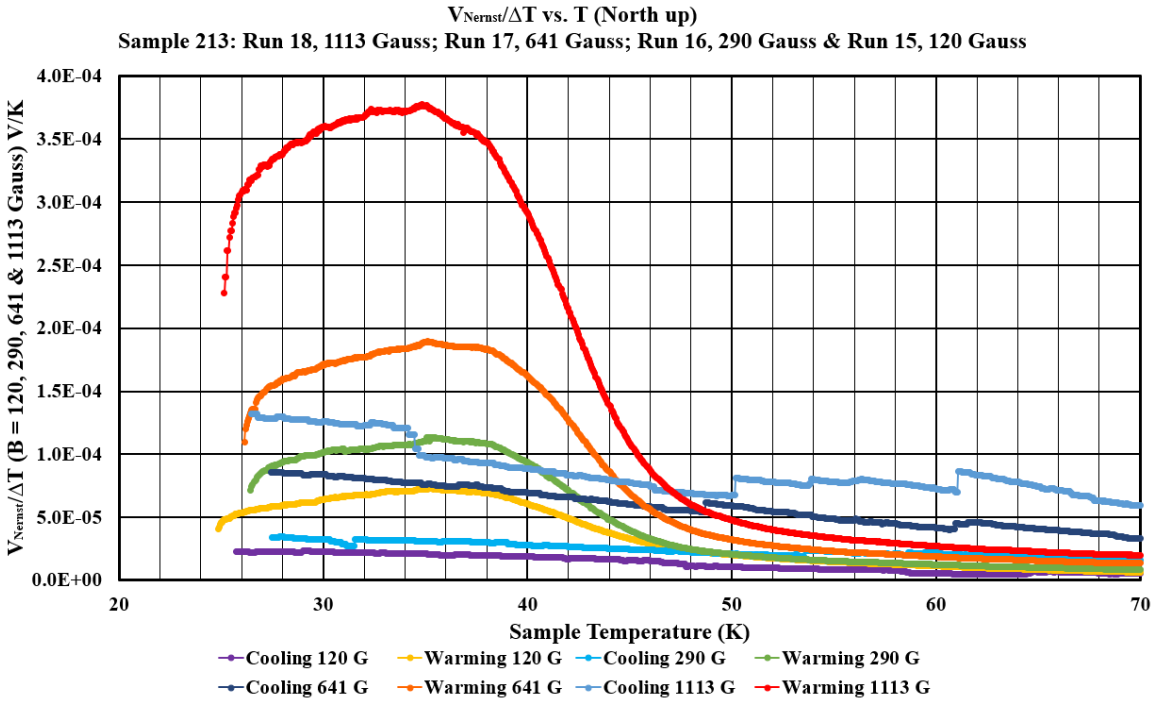

Figure 18 Nernst curves for both cooling and warming cycles from 20-70 K. [83]

C. Cyclic Nernst Experiment

The samples used in the experiments are 1 cm^2 graphene sheets mechanically exfoliated from 2 mm thick highly oriented pyrolytic graphite (HOPG). The HOPG, grade ZYB, samples were purchased and doped on a mail-in basis. The HOPG chips were phosphorus-doped and purposely damaged by argon implantation in order to provide pinning sites. The phosphorus doping was performed at a low voltage setup with 10 Kev introducing $1.2x10^8$ ions/cm^2. The argon implantation was performed at 5 Kev introducing the same number of ions as phosphorus. An array of our samples after ion implantation can be seen in figure 19.

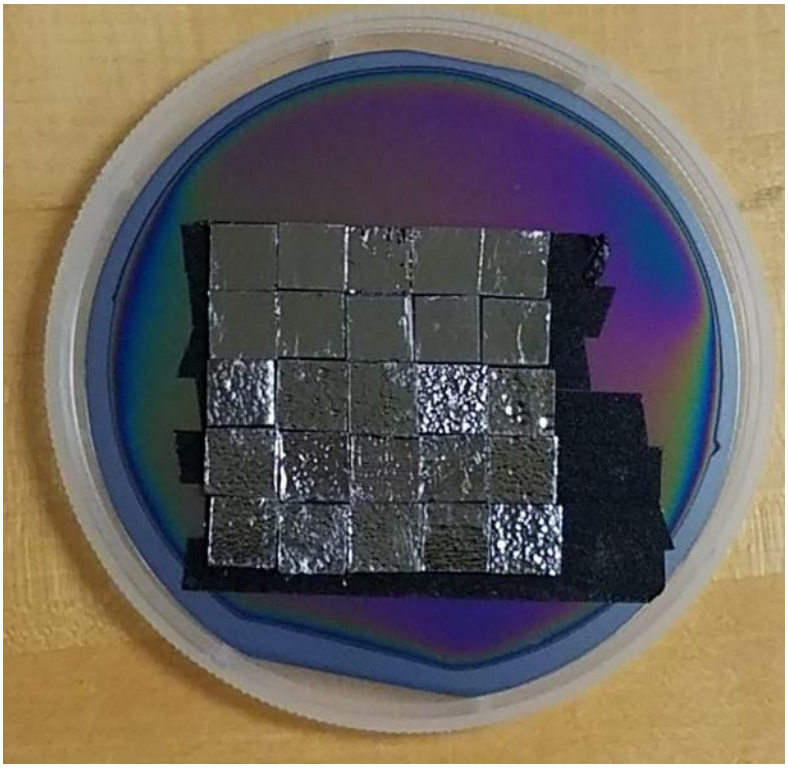

Figure 19 HOPG samples in a 5 cm by 5 cm array stuck on a silicon wafer by means of double sided carbon tape after being doped and damaged by ion implantation.

The exfoliation process was done with commercially available adhesive polyimide Kapton tape. The set up for the exfoliation process is shown in figure 20. A clamp holds a plastic chuck, which is connected to a vacuum via a hose through a hole drilled through the chuck. The HOPG chip is placed on the chuck, a piece of kapton tape is stuck to the sample and gently pressed in order rid the surface from air. Finally, the tape is carefully removed from the HOPG with the layer of graphene on it. The edges of the tape are cut with scissors.

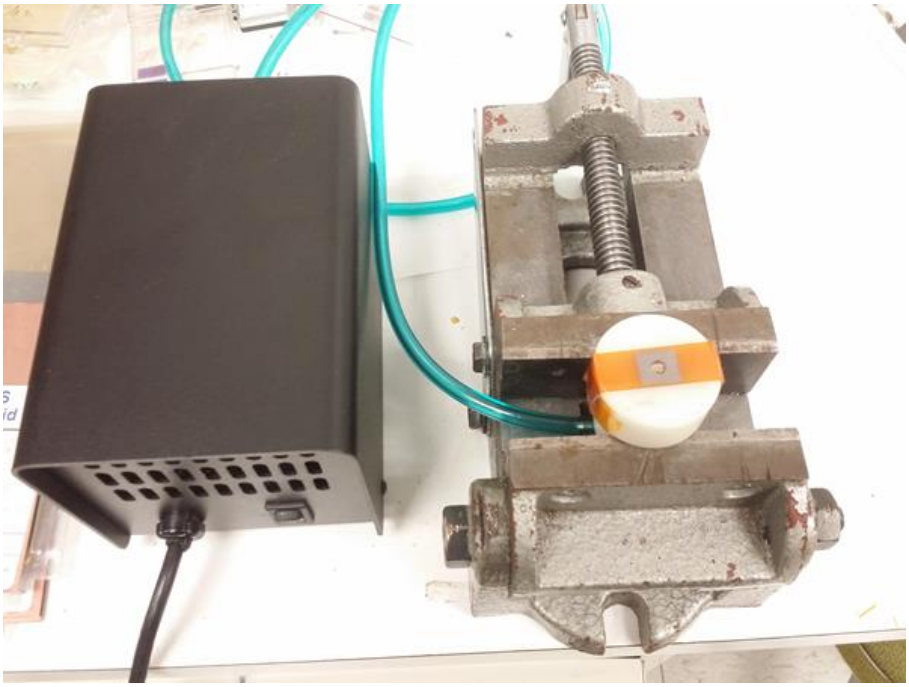

Figure 20 Exfoliation setup. The samples are placed on the chuck (right) while the vacuum system (left) holds the sample in place to facilitate the exfoliation procedure. [196]

The Nernst measurements were performed on a custom-made aluminum fixture shown in figure 21. The fixture is anchored to the cooling side of the closed-cycle Helium refrigerator while the rest of the fixture is left floating, so as to leave a gap between the cold head and the surface where the sample is placed. The gap is used to place a Neodymium disk magnet to provide a perpendicular magnetic field, in this particular experiment the field is one of 1113 Gauss. The polarity of the field is labeled north up for

runs where the north pole of the magnet is facing the graphene sample, and north down when the north pole is facing away from the graphene sample. The gap is big enough to avoid any contact from the magnet to the fixture with the purpose of not disturbing the thermal grading. On the opposite side of the fixture, a 0.10 Ω resistor is bolted in order to generate a thermal gradient through the aluminum. The resistor dissipated 0.1 W of heat to the aluminum fixture.

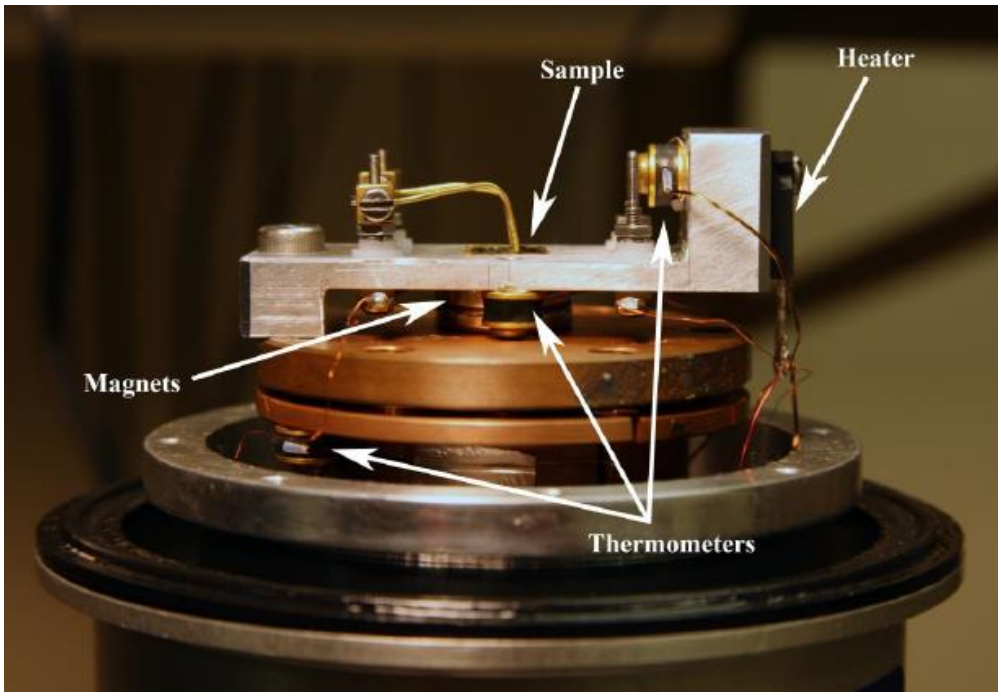

Figure 21 Nernst fixture. Aluminum fixture with an end attached on the cold head to leave space for a disk magnet. Three thermocouples are at the cold head, under the sample and at the heating site.[83]

Indium shot was molded and placed between the Aluminum and the resistor's plate to improve the thermal conductivity. Two contacts made of Brass wire were bent and bolted to the fixture to measure voltage. The temperature was measured with three sensors placed in the cold, hot and sample regions.

The chamber was then sealed and evacuated with a turbo molecular pump in preparation for the flowing of Helium via a compressor. The chamber was cooled with Helium when the pressure inside the chamber reached just under $1.5x10^{-5}$ Torr. No discernible difference was observed between having the run with active evacuation and having the chamber sealed after reaching $1.5x10^{-5}$ Torr.

The Lakeshore temperature sensors, F 70 compressor, and the Keithley 2128A nanovoltmeter were all controlled from a Labview program written specifically for the experiment. The program controls the cooling cycle and the warming cycle recording the three thermal readings from the sensors along the process.

The voltage is measured perpendicular to both the thermal gradient and magnetic field at a rate of 5 seconds per final averaged data.

The program starts by reading an initial measurement from sensor B. The measurement determines if the upcoming run is to be a cooling or warming run, by having the midrange temperature of the system be compared to the reading. In the case of the cooling cycle, the reading is higher than the midrange temperature, which will trigger the compressor to start cooling the chamber. Simultaneously, the reading is also recorded in three variables A, B, C, for cold, hot, and sample, respectively. The voltage readings star to get collected and gets stored as a variable for the cooling cycle. All variables collected at this point are tabulated and plotted by the program to be displayed through the runs. It is important to mention that the graphs being plotted are not the Nernst effect graphs, but rather the voltage vs. temperature graphs. The data is also recorded in a comma separated values (CSV) file for analysis. The flowcharts for the compressor and data acquisition programs can be observed in figures 22 and 23, respectively. The Nernst signal can then is calculated by

dividing the vector recorded for the induced dc transverse voltage by the temperature difference between the hot and cold side, that is B and A, respectively. The temperature difference is denoted by Delta-T or ΔT. The time that takes to cool the chamber and perform measurements from room temperature down to 30 K was 2400 seconds (40 minutes), while the warming cycle to 290 K was 28,800 seconds (8 hours).

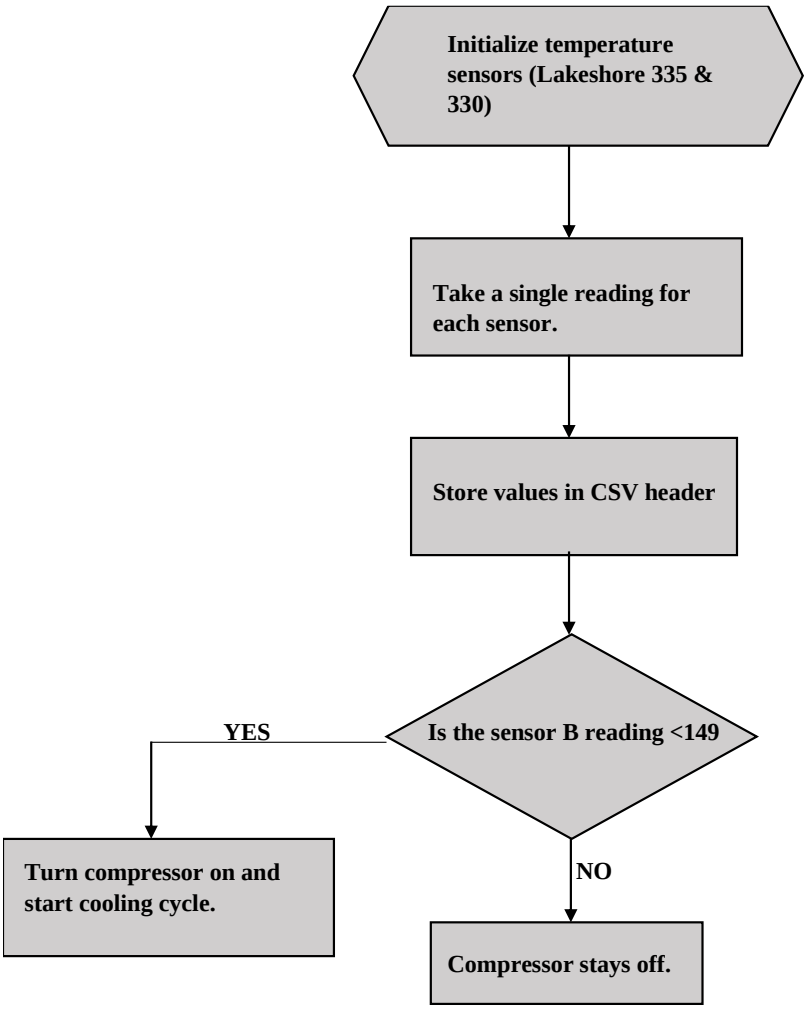

Figure 22 Compressor program flowchart

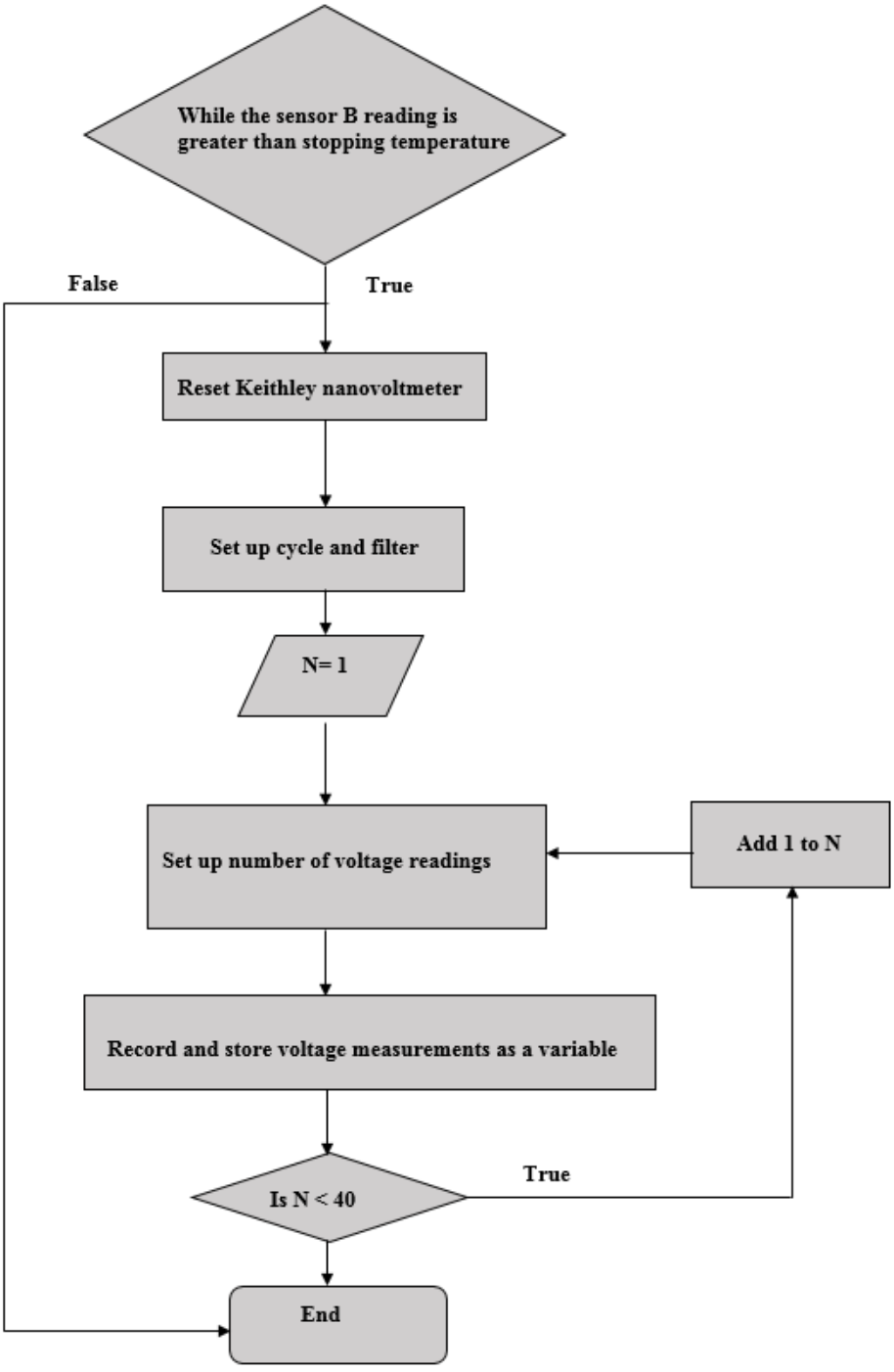

Figure 23 Voltage acquisition flowchart

The Nernst effect is used to determine and measure vorticity in a superconductor. However, in this particular experiment a cyclic Nernst experiment was performed. The temperatures used for the cycles were as follows: The chamber was cooled down to 16 K from room temperature and warmed to 150 K; 156 K down to 16 K and up to 180 K; 180 K down to 16 K and up to 220 K; 220 K to 16 K and back to 240 K; 240 K down to 16 K and back to 260 K; 260 K to 16 K and finally back to room temperature [122]. Figures 24 and 25 show all the plots with the corresponding temperature ranges.

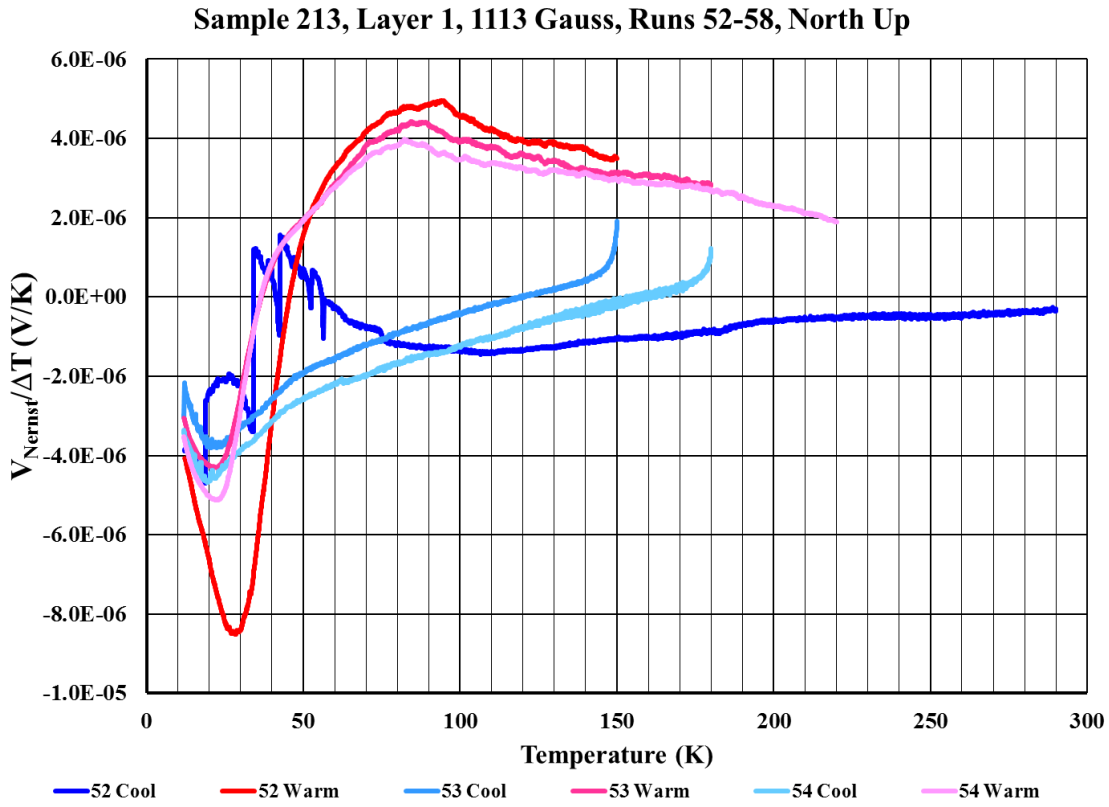

Figure 24. Warming (Warm) and cooling (Cool) curves from room temperature down to 16 K and up to 150 K (Run 52); 150 K down to 16 K and warmed up to 180 K (Run 53); and down to 16 K and warmed up to 220 K (Run 54).

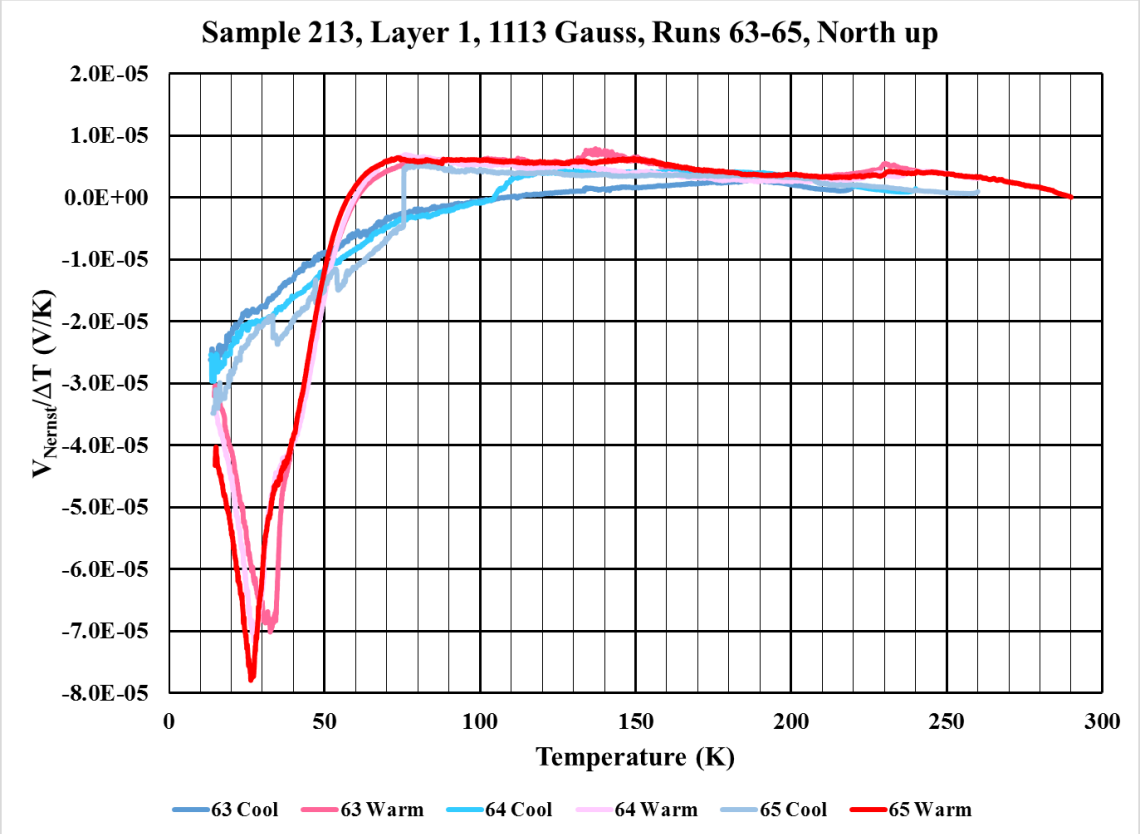

Figure 25 Warming (Warm) and cooling (Cool) curves from room temperature down to 16 K from 220 K and up to 240 K (Run 63); 240 K down to 16 K and warmed up to 260 K (Run 64); and down to 16 K and warmed up to room temperature (Run 65)

The mechanics of the system work as follows: The thermal gradient activates the flow of quasiparticles parallel to the gradient itself. As the temperature in the chamber is lowered, the system reaches the critical temperature at which vortices start to appear. The flux from the vortices aided by the thermal force and the Magnus force will deviate to a side of the sample creating a transverse voltage. The signal measured is a peak with a tail on the hotter side and a drop at the cold side. The drop indicates the freezing or the onset of a localized lattice that will diminish the transverse voltage signal. When the system starts to warm up the vortex lattice will undergo a process of melting, allowing vortices to break free and move; their movement will induce a voltage signal.

Table 4. Symbols and Acronyms

Symbol/Acronym	**Description**	**Numerical Value**
ϕ_{ion}	Ion dose	-
Q_{dep}	Deposited charge	-
FCC	Face-centered cubic	-
AFM	Atomic force microscope	-
SiO_2	Silicon Dioxide	-
HOPG	Highly-oriented pyrolytic graphite	-
CSV	Comma separated values	-

VI. RESULTS

The purpose of the previous set of experiments was to show that our phosphorus-doped graphene samples have trapped flux. By systematically varying the starting temperature of the runs, the purpose evolved to observe the behavior of the vortices at different temperature ranges.

Graphene is hypothesized to be a high temperature and highly anisotropic superconductor. As a result, it is expected to have a broad mixed-state region where the vortex fluid state is dominant. The expected phenomenon in the cyclic Nernst experiment is a tendency to remember where the refrigerator was turned on and "pick up" from there. The phenomenon is similar to that of a ferromagnetic hysteresis loop. However, it is well-established that carbon is a non-magnetic material without any d or f-shell unpaired electrons. Moreover, susceptibility measurements, especially those made at low temperatures, show a negative susceptibility. It is because of those reasons that the existence of vortices is the only explanation, known to us, that explains the presence of hysteresis loops in a diamagnetic material.

The figures 26 to 31 show a clear hysteresis loop between the cooling (blue) and warming (red) cycles. The loops come together where the refrigerator is turned off at 16 K; they diverge from each other at higher temperatures, closing again when the refrigerator is turned back on. The warming plots show the characteristic Nernst peak at temperatures near 30 K. The peak is the result of vortices being melted and entering the vortex fluid state after the BKT transition at low temperatures. The opening of the hysteresis loop is the voltage measured as the vortices diffuse due to the applied temperature gradient in the warming cycle. On the other hand, the cooling cycle has a somewhat negative slope due to

the decrease in thermal energy and the increase of the pinning energy as the temperature goes down.

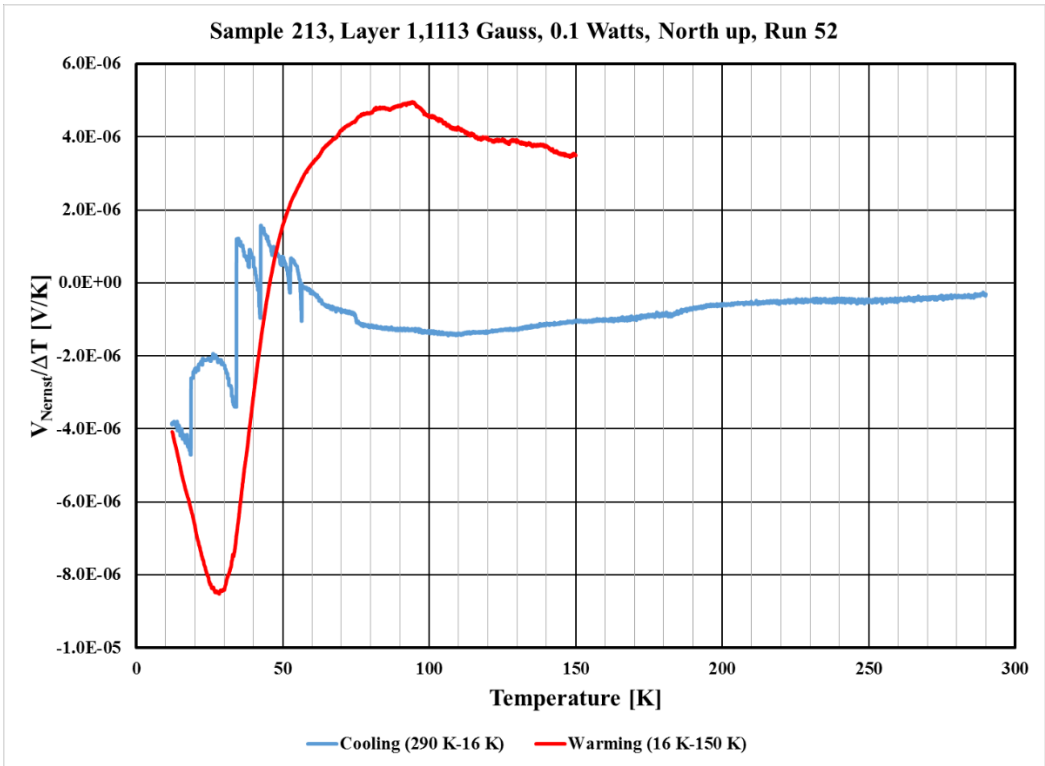

Figure 26 Field-cooled at 1113 Gauss run from 290 K down to 16 K and warming up to 150 K. A almost flat cooling curve (blue) is the result of mobile vortices. The flux is screened at 50 K, as seen in the steps below 50 K.

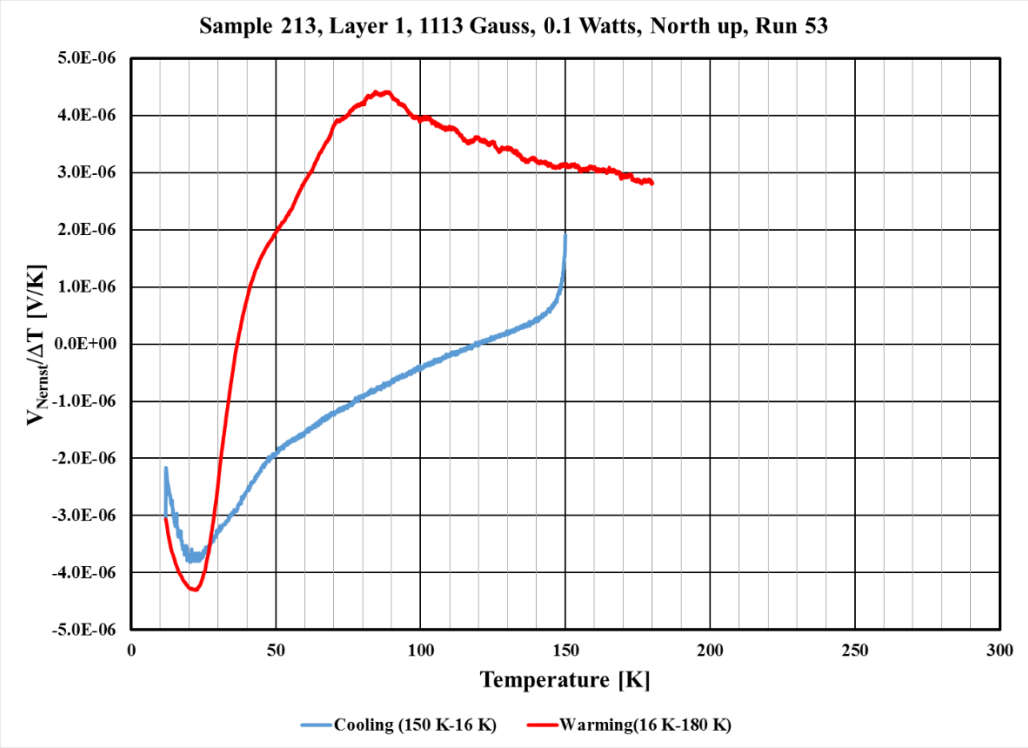

Figure 27 Field-cooled at 1113 Gauss run from 150 K down to 16 K and warming up to 180 K. The cooling curve (blue) is smoother with a downward slope as field was screened in the previous run.

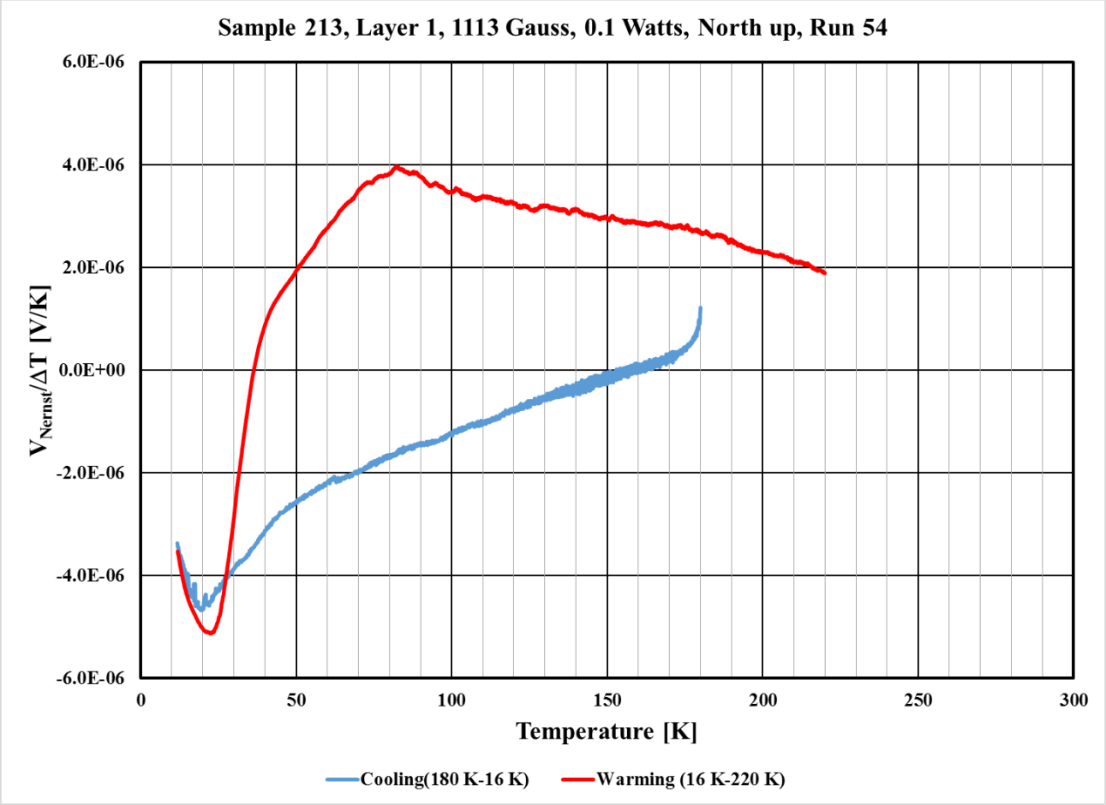

Figure 28 Field-cooled at 1113 Gauss run from 180 K to 16 K and warming to 220 K

The degree of hysteresis in the first three plots (figures 26-28) is large compared to the rest of the plots. At lower temperatures (T < 220 K) the curves close when the refrigerator is turned on, which is expected as the temperature gradient cannot be reversed instantaneously. The Nernst peaks also increase and diminish at around the same temperature (80 K) due to vortex-antivortex pair dissociation. In contrast, the plots at higher temperatures (figures 29-31) have a smaller degree of hysteresis that decreases as the temperature cycles are increased. The Nernst peak occurs at a lower temperature due to the screening of excess vortices from previous cooling-warming cycles. As a result, the balancing of vortex-antivortex pairs counters the effect of flux flow. Moreover, the diminishing effects of hysteresis and the temperature of the Nernst peaks are not explained by undesired or unexpected thermal effects. As shown in figure 32, the measured thermal

hysteresis from the runs shows no anomalous structures nor changes not consistent with a smooth temperature gradient.

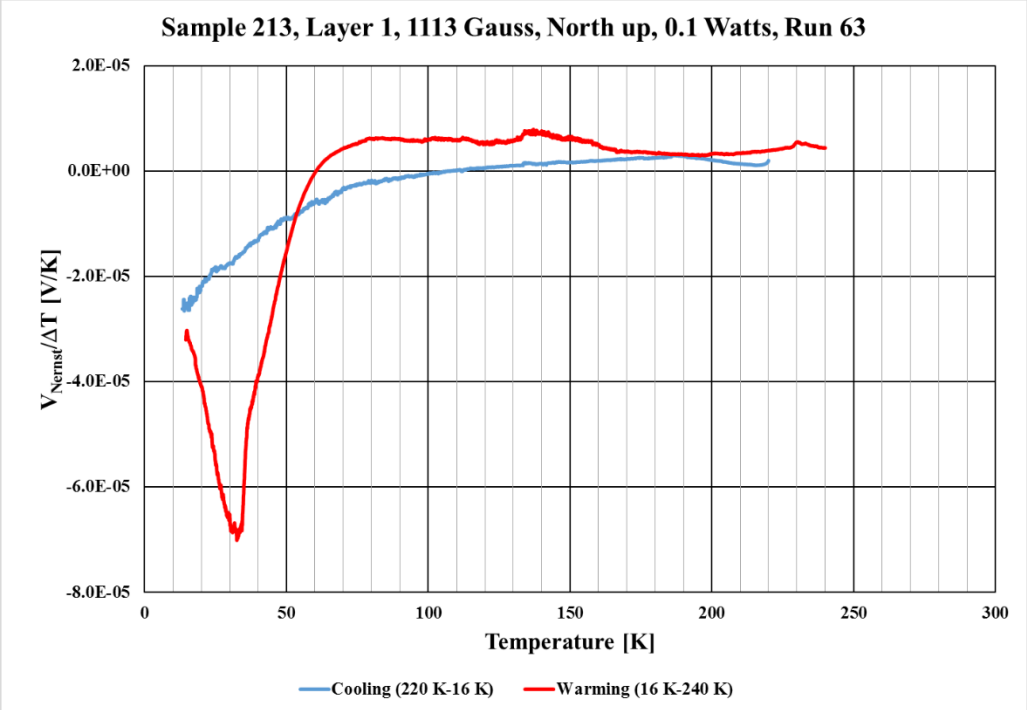

Figure 29 Field-cooled at 1113 Gauss run from 220 K to 16 K and warming up to 240 K. Hysteresis is diminished as the sample is warmed above 200 K. The closings and openings are marked by smaller Nernst peaks at 130 K and 230 K.

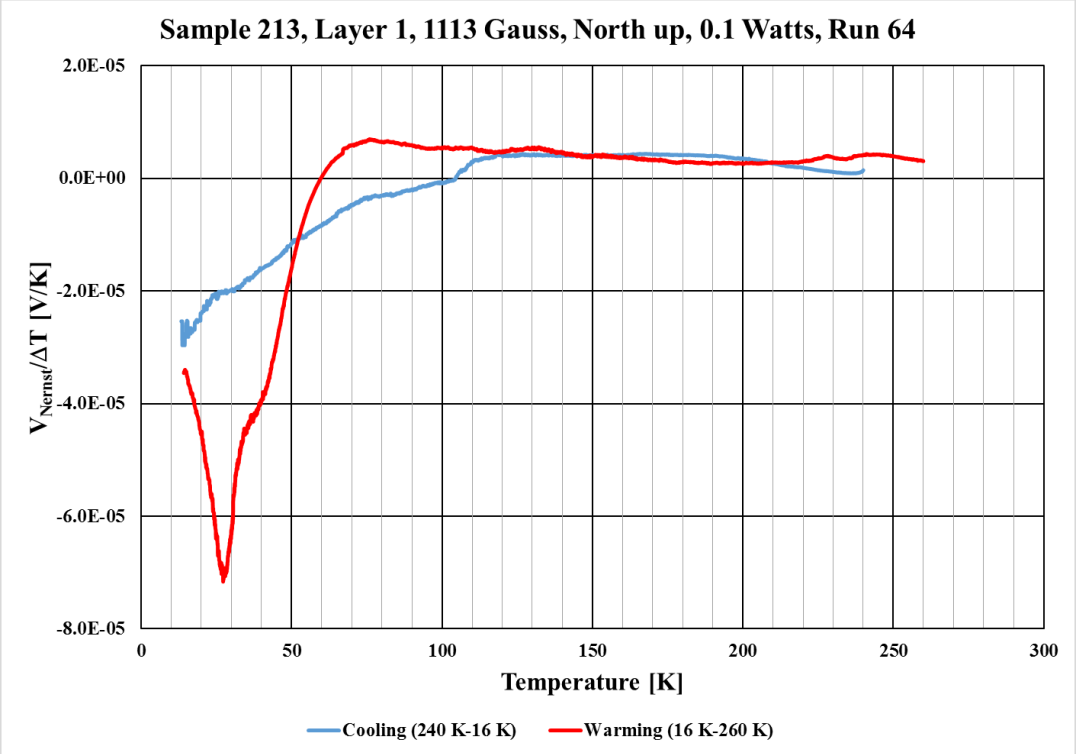

Figure 30 Field-cooled at 1113 Gauss run from 240 K to 16 K and warming up to 260 K. More vortices become mobile at higher temperatures as seen in the flatness of the cooling curve (blue).

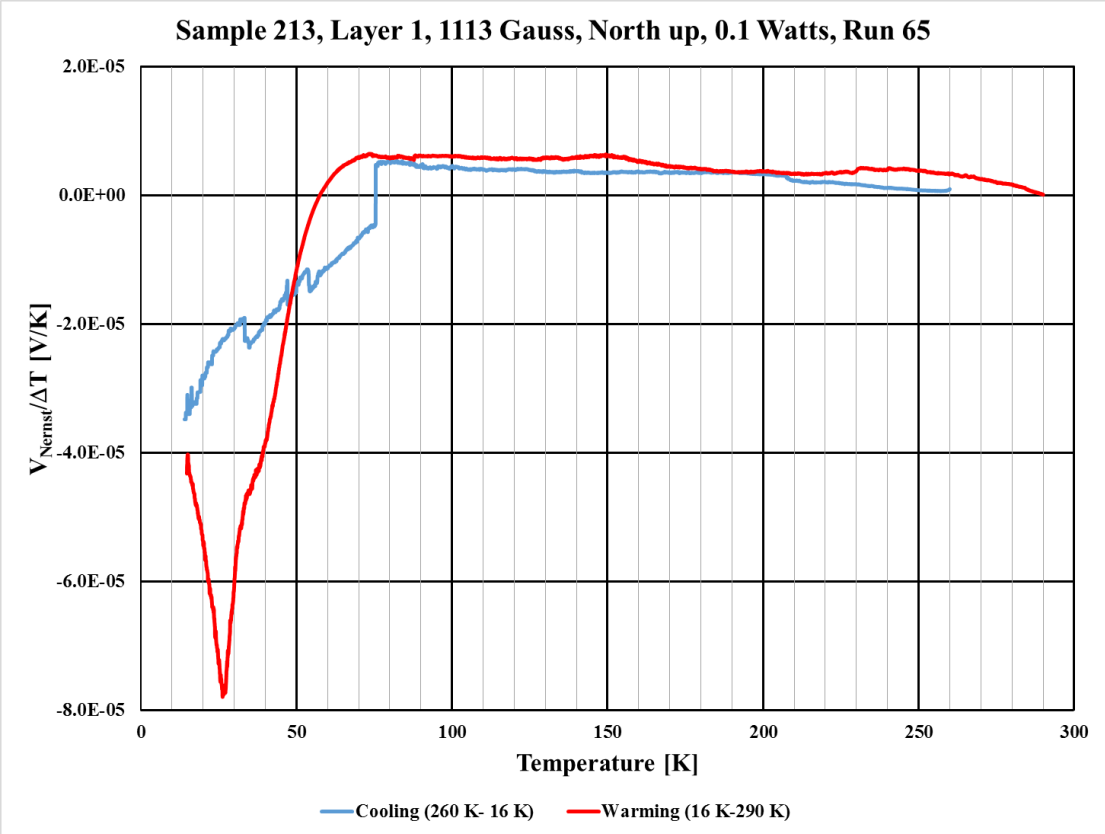

Figure 31 Field-cooled at 1113 Gauss run from 260 K to 16 K and warming up to 290 K

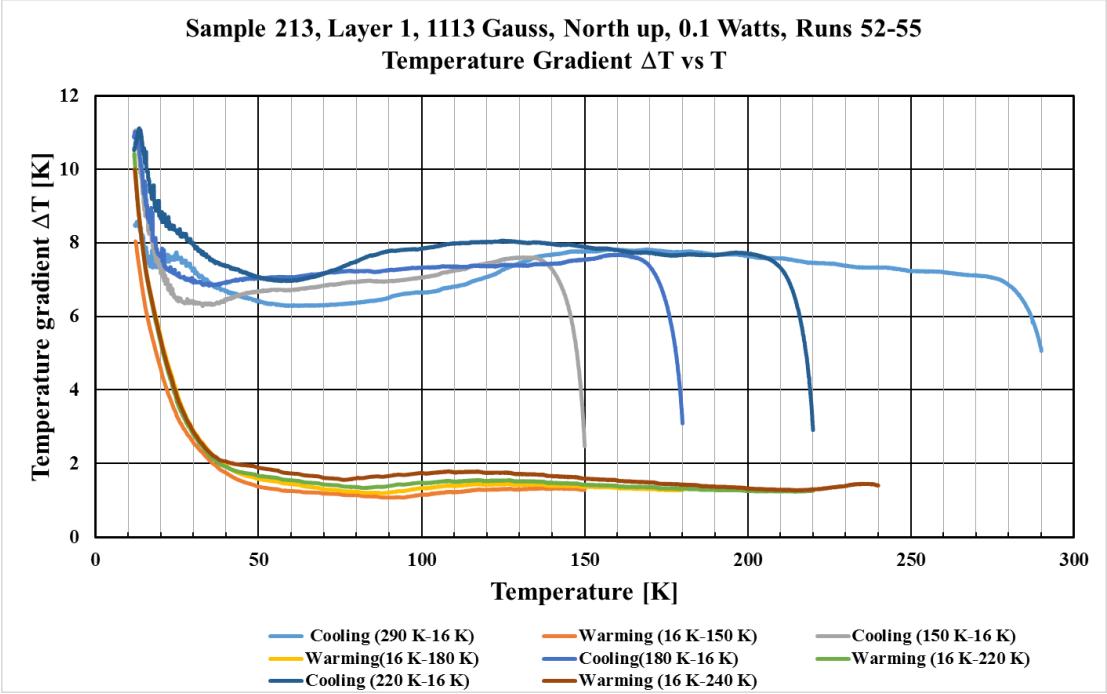

Figure 32 Thermal hysteresis from runs 52 to 55. The curves are smooth with no sign of thermal voltages

The reason for diminishing of the hysteresis can be observed in figured 33 and 34. The figures show the end of the cooling runs before the refrigerator is turned off and the system is left warming up with the Nernst resistor as the only heat source in the system. The initial plot (290 K – 16 K in light blue) has a jagged structure or a series of abrupt Nernst voltage increments that decrease as the temperature goes down. Such structure effectively disappears in subsequent runs. It is believed those peaks results, and disappear, from trapped flux being screened from the system. In other words, some of the flakes in our doped samples display some degree, or effectively, of Meissner effect at temperatures below 60 K.

Figure 34 shows the end of the cooling cycle being cooled down from higher temperatures (T > 200 K). From the plot the reappearance of the jagged steps or structure is evident. The steps are a sign that there is flux being introduced and trapped again at higher temperatures, or that melting of vortex stacks is taking place.

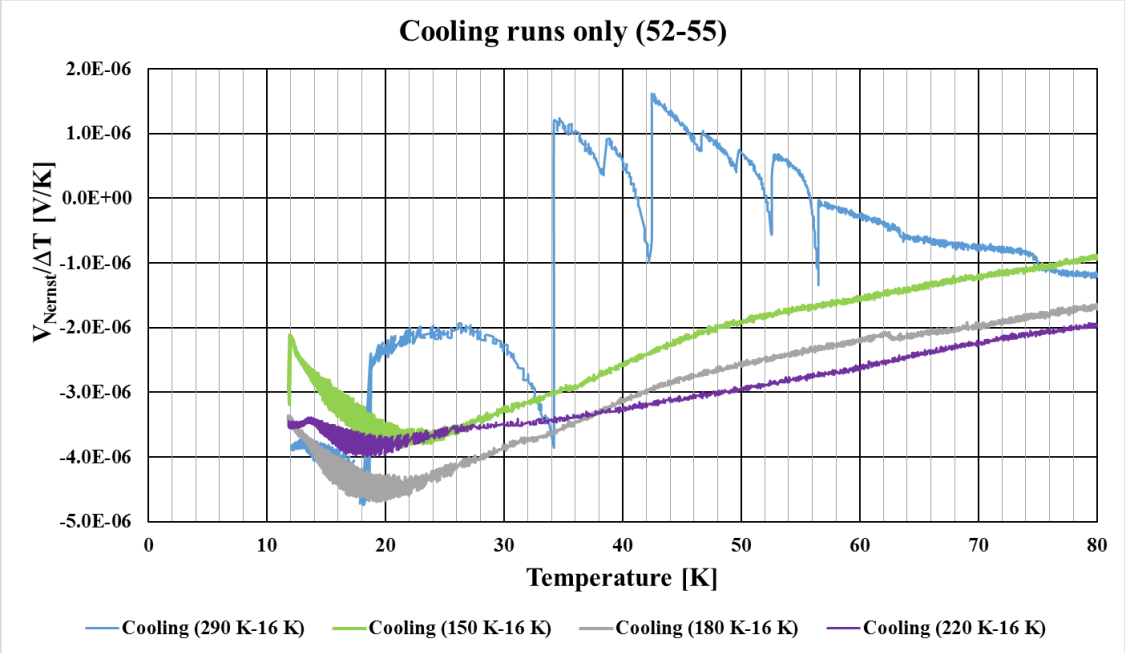

Figure 33 Close up below 80 K of FC cooling runs (52-55). After the first cooling cycle (jagged) the curves become smoother as less flux is expelled.

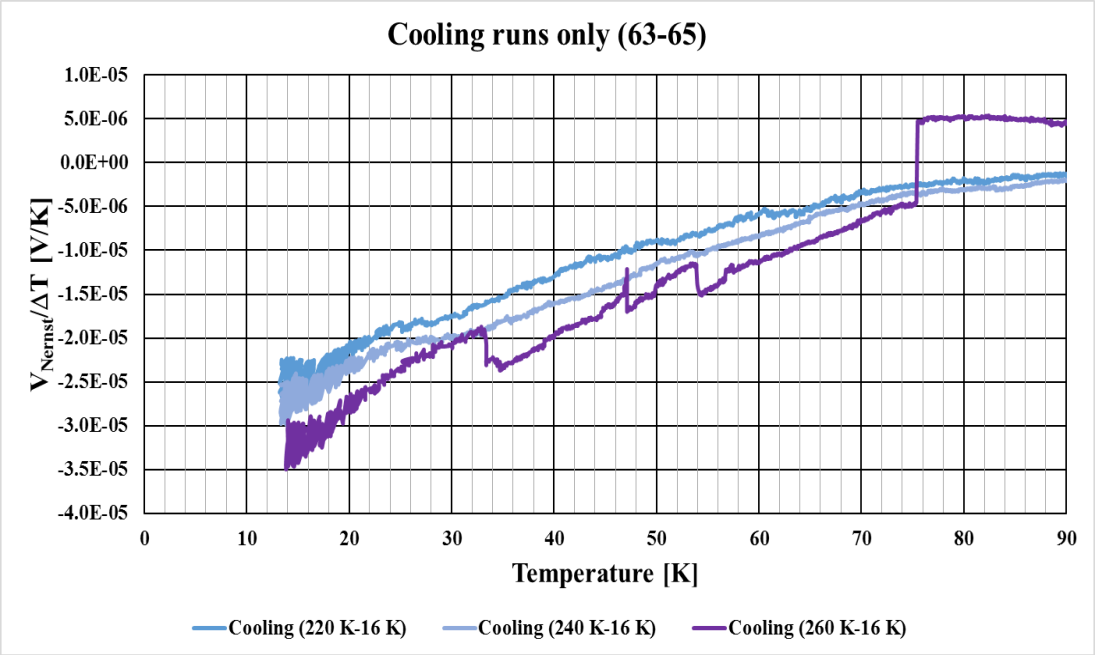

Figure 34 Field-Cooled runs 62-65 below 100 K. The jagged steps reappeared as stacks of vortices with higher activation energies are melted and eventually screened.

VII. DISCUSSION

In highly anisotropic superconductors, there is a large mixed-state region where flux is partially allowed into the sample via quantized filaments or vortices. The mixed-state region is where the irreversible behavior in type-II superconductors occurs. The irreversible behavior manifests itself as hysteresis loops in a variety of measurements as discussed earlier. The phenomenon that causes the hysteresis within the irreversibility region is the behavior of the vortices when they interact with several forces and energies. The main energies often compete against each other as a result of their opposing behaviors, and benefit different vortex states. For instance, the thermal energy is what allows the vortices to creep and, in a fluid state, to wander in the sample; however, what keeps them from moving, and in a lattice, until the necessary thermal energy is achieved, is the pinning energy. The thermal energy, when larger than the interlayer bonding energy, effectively breaks the bonds decoupling certain parameters within the layer; vortex lines and their coupling is one of them. As a result, pancake vortices and fluid and gas states of vortices benefit from strong thermal energies, while the repulsive interaction and the pinning forces benefit a lattice or glass state.

The mechanism of supercurrent generation has a role to play in the mixed-state. In a ferromagnetic material, there is a bulk current flowing in the surface of the material generating a magnetic field. The current flows in the entire material because it is the averaged current from all the electron spins; the electron spins are uniformly distributed in the material. However, the case of a type-II superconductor is different. As the flux enters the material, via the formation of vortices, the supercurrent does not flow evenly, instead it flows only in the interior of the material while trying to screen the field that attempts to

penetrate the sample. The origin of the current is Ampere's law. As the vortices enter the system, the magnetic field is not uniform (as it is the case in ferromagnetic materials). As a result, there is a magnetic field gradient which in turn generates a current [118]. As the vortex lattice melts and vortices become mobile, there is a relaxation in the bulk supercurrent generated which no longer restricts the movement of vortices. The anisotropy of materials allows for vortex stacks to be melted at different temperatures, which does not allow for screening to be uniform or fully carried out.

From the discussion it follows that non-linearity and anomalous behavior must follow when there is freezing and melting of the vortex lattice. From the results (figures 29 and 30 in results) the multiple peaks are close in appearance to those found in two-dimensional or quasi two dimensional materials when transverse voltages are measured; there is a peak with a sharp drop at the low temperature end and a tail at the high temperature end. In addition, smaller peaks, with the same structure, appear at higher temperatures suggesting that certain stacks do not melt until reaching higher temperatures. The magnetic measurements (figure 16) and drops in resistance suggest the presence of vortices and the behavior that is expected in a quasi-two dimensional and highlight anisotropic superconductor [74-76]. Moreover, the behavior is still consistent with screening or a partial Meissner effect by looking at figures 33 and 34. The figures clearly show structures disappearing when the sample is cooled below 70 K, and after being systematically warmed and cooled again. The disappearance of the jagged steps along with the shrinking of the hysteresis when warming at temperatures higher than 200 K, are consistent with the behavior of vortices being screened at low temperatures so that the balancing of vortices and antivortices, and subsequent annihilation, contributes to the diminishing of the

irreversible behavior. Moreover, after the first cycle (figure 26) the cooling curve in blue shows a downward slope as the temperature decreases, which is what is expected when less field is trapped in the material [193-196]

The behavior is also evident in the way the hysteresis area is lowered at higher temperatures. When the sample keeps being cooled from temperatures lower than 200 K, not all of the vortices are mobile. Some are still frozen, there are none entering the system and, as a result, the field gradient is not increased. The picture changes when higher temperatures are reached. There are more vortices, and antivortices, entering the system as those that were frozen become mobile, thus melting their lattice. As the system is cooled from those temperature higher than 200 K, there are more vortices being "scooped" out of the system than before (when cooled from temperatures below 200 K). The result is a system with less vortex phenomena at the high temperature end which implies less irreversibility [119] behavior and an earlier (in temperature) closing of the loop.

So far, the effects seen in the graphs shown are attributed to magnetic effects resulting from the appearance and dynamics of superconductive vortices. The appearance of such effects resulting from thermal anomalies are not possible given that the transverse probes are located at the same distance from the sample edge, longitudinally. As a result, the probes are always at the same nominal temperature; thus, making any thermal voltages improbable. Moreover, assuming that a small deviation in the positioning of the probes does exist, the resulting voltages would not result in significant effects given the slow rate of change of the gradient in graphene as compared with the overall rate of change of the temperature gradient.

VIII. CONCLUSION

Phosphorus-doped graphene exhibits characteristics inherent to highly anisotropic, layered and two-dimensional superconductors. There is a broad resistive region (16 K- 260 K) corresponding to the mixed state. From the results it is determined that: There are clear peaks (Nernst) near 30 K; a sign of vortices becoming mobile as the temperature increases and thermal energy is gained. Smaller peaks are seen at higher temperatures near 230 K resulting from vortices becoming free of their pinning sites at such temperatures. The peaks also coincide with flux screening, flux trapping, and a BKT transition as there is hysteresis in each of the runs made in the cyclic experiment that become smaller when the sample was warmed above 200 K, effectively closing at 210 K and reopening at higher temperatures as a result of vortex melting. Finally, partial Meissner is also observed at low temperatures in the form of jagged steps that eventually disappear when the sample is warmed and cooled cyclically.

To conclude, the unique physical properties of graphene combined with the addition of charge carriers and pinning sites via ion implantation have shown clear signs of mixed-state superconductivity with an estimated critical temperature near 240 K. The susceptibility and thermal measurements discard other sources of Nernst voltage and hysteresis in the phosphorus-doped samples; superconductivity then remains as the only theory known to us that explains the phenomena presented in this work.

IX. FUTURE WORK

A. Vortices through a constriction

The theory of vortices in type-II superconductors was tested by R. D. Parks in 1965 [205]. The experiment consisted of having a thin bridge between two superconducting films. The set up was then subjected to different magnetic fields. In the experiment, Parks proposed that with a low enough field, the vortices appearing in the material were few and big. As a result, they should not be able to travel through the constriction. However, if the field is increased, there will be more vortices with a lower coherence length. At the exact field, the vortices would have an appropriate size to move through the constriction. The absence of vortices in the bridge or constriction would be rise to a current shielding from the field, while if vortices were to be present in the bridge, such current would not be present.

The R. D. Parks experiment is the basis of our experiment. Our doped graphene-on-Kapton tape samples were cut in the appropriate shape using a 20 μm beam Argon-fluoride laser. The samples were cut to have a bridge 0.01 -1 mm thick and 2-3 mm long. The experiment set up is seen schematically in figure 35.

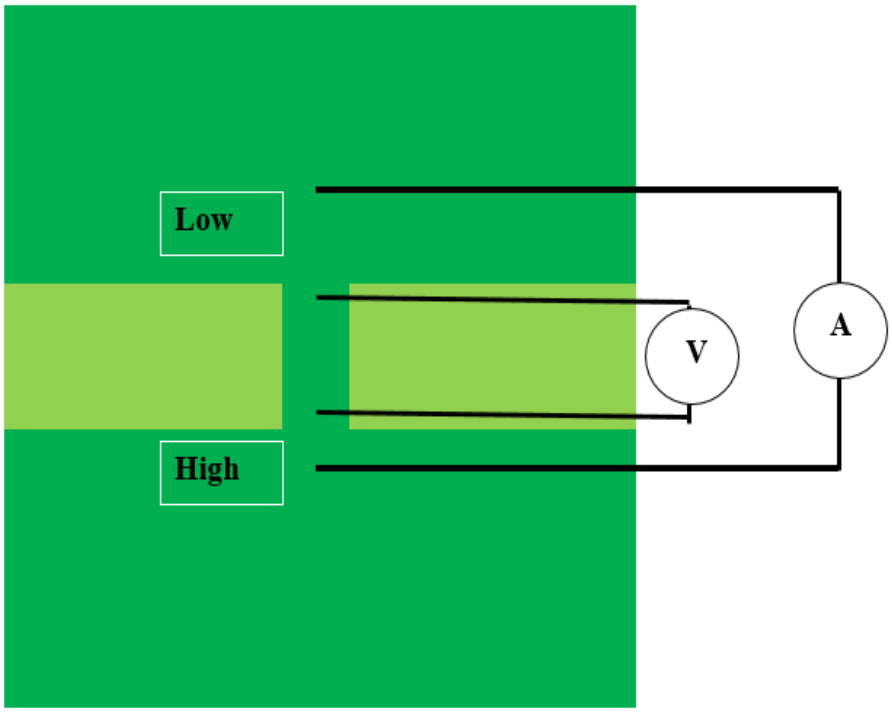

Figure 35 Schematic of the constriction and relative probe placement

A program was written to measure the current versus voltage characteristics across the bridge at every degree Kelvin while warming (Appendix). A series of *I-V* measurements are to be made while applying a magnetic field perpendicular to the sample, systematically increasing it. The basis of this experiment is that the absence of vortices should produce linear (ohmic) characteristics as the applied current sweep should develop a longitudinal potential proportional to the current. On the other hand, if vortices become small enough, that is if the field is strong enough, then nonlinearities should appear as the current and voltages are no longer ohmic, and there would be regions of superconductive transport. Such nonlinear behavior should also disappear as a large enough magnetic field is applied,

quenching the superconductivity. The expected results can give us a notion of the size of the vortices and their behavior as they are forced to arrange themselves in a constriction.

B. Electrostatic doping

As in many high temperature superconductors, ferroelectric substrates have had a significant increase in its transport properties as well as in the temperature at which they occur. Our graphene samples have in the past demonstrated significant effects at much higher temperatures than the most popular high-temperature superconductors. Therefore, we to modulate and increase these effects with the use of ferroelectrics.

The first set of measurements involve the transverse electric field induced by a longitudinal thermal gradient and a perpendicular magnetic field apply on the sample. In other words, a set of standard Nernst effect measurements to study the effects of the ferroelectric on the mixed-state properties of multilayer graphene. The setup for this experiment inside the closed cycle refrigerator consists of a custom-made aluminum fixture, bolted on one end while leaving space under it to place rare metal magnets to provide a source of magnetic perpendicular magnetic field. The other end of the fixture is used to hold a 10 Ω resistor, powered by an eternal dc source, as a means of applying a temperature gradient. Thermometers are placed along the fixture to measure temperature at the hot end, at the sample and at the cold end of the fixture.

A second set of measurements would involve traditional resistance versus temperature curves. Resistance measurements are done via a four-probe setting where a stimulus current of 10 μA or less is run across the sample. Simultaneously the voltage measured across the sample is used with the applied current in a Keithley 6221/2182A delta setting to obtain the resistance of the material. An external dc source is used as a gate voltage Vg in order to tune and pole the ferroelectric layer.

REFERENCES

1. K. S. Novoselov et al, "Two-dimensional gas of massless Dirac fermions in graphene," Nature, vol. 438, (7065), pp. 197-200, 2005.

2. K. S. Novoselov et al, "Electric field effect in atomically thin carbon films," Science, vol. 306, (5696), pp. 666-669, 2004.

3. J. C. Meyer et al, "The structure of suspended graphene sheets," Nature, vol. 446, (7131), pp. 60-63, 2007.

4. J. Salvetat et al, "Mechanical properties of carbon nanotubes," Applied Physics A, vol. 69, (3), pp. 255-260, 1999.

5. T. W. Tombler et al, "Reversible electromechanical characteristics of carbon nanotubes underlocal-probe manipulation," Nature, vol. 405, (6788), pp. 769-772, 2000.

6. I. W. Frank et al, "Mechanical properties of suspended graphene sheets," Journal of Vacuum Science & Technology B: Microelectronics and Nanometer Structures Processing, Measurement, and Phenomena, vol. 25, (6), pp. 2558-2561, 2007.

7. C. Lee et al, "Measurement of the elastic properties and intrinsic strength of monolayer graphene," Science, vol. 321, (5887), pp. 385-388, 2008.

8. Y. Shibutani and S. Ogata, "Mechanical integrity of carbon nanotubes for bending and torsion," Modell Simul Mater Sci Eng, vol. 12, (4), pp. 599, 2004.

9. F. Liu, P. Ming and J. Li, "Ab initio calculation of ideal strength and phonon instability of graphene under tension," Physical Review B, vol. 76, (6), pp. 064120, 2007.

10. S. P. Koenig et al, "Ultrastrong adhesion of graphene membranes," Nature Nanotechnology, vol. 6, (9), pp. 543, 2011.

11. A. C. Neto et al, "The electronic properties of graphene," Reviews of Modern Physics, vol. 81, (1), pp. 109, 2009.

12. M. I. Katsnelson, K. S. Novoselov and A. K. Geim, "Chiral tunnelling and the Klein paradox in graphene," Nature Physics, vol. 2, (9), pp. 620-625, 2006.

13. N. Stander, B. Huard and D. Goldhaber-Gordon, "Evidence for Klein tunneling in graphene p− n junctions," Phys. Rev. Lett., vol. 102, (2), pp. 026807, 2009.

14. A. F. Young and P. Kim, "Quantum interference and Klein tunnelling in graphene heterojunctions," Nature Physics, vol. 5, (3), pp. 222-226, 2009.

15. J. H. Warner et al, Graphene: Fundamentals and Emergent Applications. 2012.

16. L. Brus, "Size, dimensionality, and strong electron correlation in nanoscience," Acc. Chem. Res., vol. 47, (10), pp. 2951-2959, 2014.

17. D. R. Cooper et al, "Experimental review of graphene," International Scholarly Research Notices, vol. 2012, 2012.

18. N. Peres, "The transport properties of graphene," Journal of Physics: Condensed Matter, vol. 21, (32), pp. 323201, 2009.

19. S. Pisana et al, "Breakdown of the adiabatic Born–Oppenheimer approximation in graphene," Nature Materials, vol. 6, (3), pp. 198-201, 2007.

20. E. H. Hwang and S. D. Sarma, "Acoustic phonon scattering limited carrier mobility in two-dimensional extrinsic graphene," Physical Review B, vol. 77, (11), pp. 115449, 2008.

21. S. Adam et al, "A self-consistent theory for graphene transport," Proceedings of the National Academy of Sciences, vol. 104, (47), pp. 18392-18397, 2007.

22. F. Schedin et al, "Detection of individual gas molecules adsorbed on graphene," Nature Materials, vol. 6, (9), pp. 652-655, 2007.

23. C. Kittel, P. McEuen and P. McEuen, Introduction to Solid State Physics. 19968.

24. K. I. Bolotin et al, "Ultrahigh electron mobility in suspended graphene," Solid State Commun., vol. 146, (9-10), pp. 351-355, 2008.

25. C. R. Dean et al, "Boron nitride substrates for high-quality graphene electronics," Nature Nanotechnology, vol. 5, (10), pp. 722-726, 2010.

26. R. Prasher, "Graphene spreads the heat," Science, vol. 328, (5975), pp. 185-186, 2010.

27. Y. Xu, Z. Li and W. Duan, "Thermal and thermoelectric properties of graphene," Small, vol. 10, (11), pp. 2182-2199, 2014.

28. A. A. Balandin et al, "Superior thermal conductivity of single-layer graphene," Nano Letters, vol. 8, (3), pp. 902-907, 2008.

29. I. Calizo et al, "Temperature dependence of the Raman spectra of graphene and graphene multilayers," Nano Letters, vol. 7, (9), pp. 2645-2649, 2007.

30. D. S. Ghosh et al, "Extremely high thermal conductivity of graphene: Prospects for thermal management applications in nanoelectronic circuits," Appl. Phys. Lett., vol. 92, (15), pp. 151911, 2008.

31. J. Jiang, J. Wang and B. Li, "Thermal expansion in single-walled carbon nanotubes and graphene: Nonequilibrium Green's function approach," Physical Review B, vol. 80, (20), pp. 205429, 2009.

32. G. Benedek, J. R. Manson and S. Miret-Artés, "The electron–phonon coupling constant for single-layer graphene on metal substrates determined from He atom scattering," Physical Chemistry Chemical Physics, vol. 23, (13), pp. 7575-7585, 2021.

33. X. Li et al, "Strain effects on the thermal conductivity of nanostructures," Physical Review B, vol. 81, (24), pp. 245318, 2010.

34. K. Sun, M. A. Stroscio and M. Dutta, "Graphite C-axis thermal conductivity," Superlattices and Microstructures, vol. 45, (2), pp. 60-64, 2009.

35. F. Hao, D. Fang and Z. Xu, "Mechanical and thermal transport properties of graphene with defects," Appl. Phys. Lett., vol. 99, (4), pp. 041901, 2011.

36. N. Wei et al, "Strain engineering of thermal conductivity in graphene sheets and nanoribbons: a demonstration of magic flexibility," Nanotechnology, vol. 22, (10), pp. 105705, 2011.

37. J. Jiang et al, "Isotopic effects on the thermal conductivity of graphene nanoribbons: Localization mechanism," J. Appl. Phys., vol. 107, (5), pp. 054314, 2010.

38. A. V. Krasheninnikov et al, "Embedding transition-metal atoms in graphene: structure, bonding, and magnetism," Phys. Rev. Lett., vol. 102, (12), pp. 126807, 2009.

39. M. P. López-Sancho, F. de Juan and M. A. Vozmediano, "Magnetic moments in the presence of topological defects in graphene," Physical Review B, vol. 79, (7), pp. 075413, 2009.

40. K. Harigaya and T. Enoki, "Mechanism of magnetism in stacked nanographite with open shell electrons," Chemical Physics Letters, vol. 351, (1-2), pp. 128-134, 2002.

41. Y. Wang et al, "Room-temperature ferromagnetism of graphene," Nano Letters, vol. 9, (1), pp. 220-224, 2009.

42. J. Fernández-Rossier and J. J. Palacios, "Magnetism in graphene nanoislands," Phys. Rev. Lett., vol. 99, (17), pp. 177204, 2007.

43. L. Pisani et al, "Electronic structure and magnetic properties of graphitic ribbons," Physical Review B, vol. 75, (6), pp. 064418, 2007.

44. M. Sepioni et al, "Limits on intrinsic magnetism in graphene," Phys. Rev. Lett., vol. 105, (20), pp. 207205, 2010.

45. R. R. Nair et al, "Spin-half paramagnetism in graphene induced by point defects," Nature Physics, vol. 8, (3), pp. 199-202, 2012.

46. P. Venezuela, M. Lazzeri and F. Mauri, "Theory of double-resonant Raman spectra in graphene: Intensity and line shape of defect-induced and two-phonon bands," Physical Review B, vol. 84, (3), pp. 035433, 2011.

47. K. F. Mak et al, "The evolution of electronic structure in few-layer graphene revealed by optical spectroscopy," Proceedings of the National Academy of Sciences, vol. 107, (34), pp. 14999-15004, 2010.

48. Y. H. Wu, T. Yu and Z. X. Shen, "Two-dimensional carbon nanostructures: Fundamental properties, synthesis, characterization, and potential applications," J. Appl. Phys., vol. 108, (7), pp. 10, 2010.

49. B. Nanda et al, "Electronic structure of the substitutional vacancy in graphene: density-functional and Green's function studies," New Journal of Physics, vol. 14, (8), pp. 083004, 2012.

50. M. M. Ugeda et al, "Missing atom as a source of carbon magnetism," Phys. Rev. Lett., vol. 104, (9), pp. 096804, 2010.

51. O. V. Yazyev and L. Helm, "Defect-induced magnetism in graphene," Physical Review B, vol. 75, (12), pp. 125408, 2007.

52. J. Balakrishnan et al, "Colossal enhancement of spin–orbit coupling in weakly hydrogenated graphene," Nature Physics, vol. 9, (5), pp. 284-287, 2013.

53. C. L. Kane and E. J. Mele, "Quantum spin Hall effect in graphene," Phys. Rev. Lett., vol. 95, (22), pp. 226801, 2005.

54. I. Žutić, J. Fabian and S. D. Sarma, "Spintronics: Fundamentals and applications," Reviews of Modern Physics, vol. 76, (2), pp. 323, 2004.

55. N. Tombros et al, "Electronic spin transport and spin precession in single graphene layers at room temperature," Nature, vol. 448, (7153), pp. 571-574, 2007.

56. W. Han et al, "Tunneling spin injection into single layer graphene," Phys. Rev. Lett., vol. 105, (16), pp. 167202, 2010.

57. P. J. Zomer et al, "Long-distance spin transport in high-mobility graphene on hexagonal boron nitride," Physical Review B, vol. 86, (16), pp. 161416, 2012.

58. T. Yang et al, "Observation of long spin-relaxation times in bilayer graphene at room temperature," Phys. Rev. Lett., vol. 107, (4), pp. 047206, 2011.

59. H. H. Weitering and J. Z. Wu, "Superconductivity: how the unconventional became the new norm," Superconductor Science and Technology, vol. 30, (4), pp. 040301, 2017.

60. J. Bardeen, L. N. Cooper and J. R. Schrieffer, "Theory of superconductivity," Physical Review, vol. 108, (5), pp. 1175, 1957.

61. J. F. Annett, Superconductivity, Superfluids and Condensates. 20045.

62. C. Brun, T. Cren and D. Roditchev, "Review of 2D superconductivity: the ultimate case of epitaxial monolayers," Superconductor Science and Technology, vol. 30, (1), pp. 013003, 2016.

63. K. Kadowaki, "Vortex states in high-Tc superconductors and superconductivity in modern nano-science and engineering," Science and Technology of Advanced Materials, vol. 6, (6), pp. 589-603, 2005.

64. C. Goupil et al, "Thermodynamics of thermoelectric phenomena and applications," Entropy, vol. 13, (8), pp. 1481-1517, 2011.

65. H. B. Callen, "The application of Onsager's reciprocal relations to thermoelectric, thermomagnetic, and galvanomagnetic effects," Physical Review, vol. 73, (11), pp. 1349, 1948.

66. L. Onsager, "Reciprocal relations in irreversible processes. I." Physical Review, vol. 37, (4), pp. 405, 1931.

67. L. Onsager, "Reciprocal relations in irreversible processes. II." Physical Review, vol. 38, (12), pp. 2265, 1931.

68. K. Behnia and H. Aubin, "Nernst effect in metals and superconductors: a review of concepts and experiments," Reports on Progress in Physics, vol. 79, (4), pp. 046502, 2016.

69. Y. Imry and R. Landauer, "Conductance viewed as transmission," Reviews of Modern Physics, vol. 71, (2), pp. S306, 1999.

70. H. Van Houten et al, "Thermo-electric properties of quantum point contacts," Semiconductor Science and Technology, vol. 7, (3B), pp. B215, 1992.

71. K. Behnia, Fundamentals of Thermoelectricity. 2015.

72. R. Landauer, "Spatial variation of currents and fields due to localized scatterers in metallic conduction," IBM Journal of Research and Development, vol. 1, (3), pp. 223-231, 1957.

73. J. Lowell, J. S. Munoz and J. Sousa, "Thermally induced voltages in the mixed state of type II superconductors," Physics Letters A, vol. 24, (7), pp. 376-377, 1967.

74. R. P. Huebener and A. Seher, "Nernst effect and flux flow in superconductors. I. Niobium," Physical Review, vol. 181, (2), pp. 701, 1969.

75. M. Zeh et al, "Nernst effect in superconducting Y-Ba-Cu-O," Phys. Rev. Lett., vol. 64, (26), pp. 3195, 1990.

76. R. P. Huebener, "Superconductors in a temperature gradient," Superconductor Science and Technology, vol. 8, (4), pp. 189, 1995.

77. N. P. Ong et al, "Vorticity and the Nernst effect in cuprate superconductors," Annalen Der Physik, vol. 13, (1-2), pp. 9-14, 2004.

78. Y. Wang et al, "Onset of the vortex-like Nernst signal above T c in La 2− x Sr x CuO 4 and Bi 2 Sr 2− y La y CuO 6," Physical Review B, vol. 64, (22), pp. 224519, 2001.

79. Y. Wang et al, "High field phase diagram of cuprates derived from the Nernst effect," Phys. Rev. Lett., vol. 88, (25), pp. 257003, 2002.

80. Y. Wang et al, "Dependence of upper critical field and pairing strength on doping in cuprates," Science, vol. 299, (5603), pp. 86-89, 2003.

81. A. Pourret et al, "Strong correlation and low carrier density in Fe 1 y Te 0.6 Se 0.4 as seen from its thermoelectric response," Physical Review B, vol. 83, (2), pp. 020504, 2011.

82. A. Kondrat et al, "Unusual Nernst effect and spin density wave precursors in superconducting LaFeAsO 1− x F x," Physical Review B, vol. 83, (9), pp. 092507, 2011.

83. N. Sornkhampan et al, "Evidence of vortices and mixed-state superconductivity in phosphorus-doped graphene. Part I (Nernst)," Superconductor Science and Technology, vol. 34, (3), pp. 035022, 2021.

84. J. M. Kosterlitz and D. J. Thouless, "Ordering, metastability and phase transitions in two-dimensional systems," Journal of Physics C: Solid State Physics, vol. 6, (7), pp. 1181, 1973.

85. J. T. Ye et al, "Superconducting dome in a gate-tuned band insulator," Science, vol. 338, (6111), pp. 1193-1196, 2012.

86. J. Hone, "Transport measurements of MoS2 using a van der Waals heterostructure device platform," Bulletin of the American Physical Society, vol. 61, 2016.

87. Y. Saito et al, "Superconductivity protected by spin–valley locking in ion-gated MoS 2," Nature Physics, vol. 12, (2), pp. 144-149, 2016.

88. D. Costanzo et al, "Gate-induced superconductivity in atomically thin MoS 2 crystals," Nature Nanotechnology, vol. 11, (4), pp. 339-344, 2016.

89. N. D. Mermin and H. Wagner, "Absence of ferromagnetism or antiferromagnetism in one-or two-dimensional isotropic Heisenberg models," Phys. Rev. Lett., vol. 17, (22), pp. 1133, 1966.

90. S. Coleman, "There are no Goldstone bosons in two dimensions," Communications in Mathematical Physics, vol. 31, (4), pp. 259-264, 1973.

91. V. L. Berezinskii, "Destruction of long-range order in one-dimensional and two-dimensional systems having a continuous symmetry group I. Classical systems," Sov.Phys.JETP, vol. 32, (3), pp. 493-500, 1971.

92. T. I. Baturina and V. M. Vinokur, "Superinsulator–superconductor duality in two dimensions," Annals of Physics, vol. 331, pp. 236-257, 2013.

93. J. M. Kosterlitz and D. J. Thouless, "Long range order and metastability in two dimensional solids and superfluids.(Application of dislocation theory)," Journal of Physics C: Solid State Physics, vol. 5, (11), pp. L124, 1972.

94. T. Uchihashi, "Two-dimensional superconductors with atomic-scale thickness," Superconductor Science and Technology, vol. 30, (1), pp. 013002, 2016.

95. D. J. Bishop and J. D. Reppy, "Study of the superfluid transition in two-dimensional He 4 films," Phys. Rev. Lett., vol. 40, (26), pp. 1727, 1978.

96. G. Agnolet, D. F. McQueeney and J. D. Reppy, "Kosterlitz-Thouless transition in helium films," Physical Review B, vol. 39, (13), pp. 8934, 1989.

97. M. R. Beasley, J. E. Mooij and T. P. Orlando, "Possibility of vortex-antivortex pair dissociation in two-dimensional superconductors," Phys. Rev. Lett., vol. 42, (17), pp. 1165, 1979.

98. M. Gabay and A. Kapitulnik, "Vortex-antivortex crystallization in thin superconducting and superfluid films," Phys. Rev. Lett., vol. 71, (13), pp. 2138, 1993.

99. B. Sacépé et al, "Disorder-induced inhomogeneities of the superconducting state close to the superconductor-insulator transition," Phys. Rev. Lett., vol. 101, (15), pp. 157006, 2008.

100. Y. Noat et al, "Unconventional superconductivity in ultrathin superconducting NbN films studied by scanning tunneling spectroscopy," Physical Review B, vol. 88, (1), pp. 014503, 2013.

101. M. Chand et al, "Phase diagram of the strongly disordered s-wave superconductor NbN close to the metal-insulator transition," Physical Review B, vol. 85, (1), pp. 014508, 2012.

102. A. Kamlapure et al, "Emergence of nanoscale inhomogeneity in the superconducting state of a homogeneously disordered conventional superconductor," Scientific Reports, vol. 3, (1), pp. 1-8, 2013.

103. C. Carbillet et al, "Confinement of superconducting fluctuations due to emergent electronic inhomogeneities," Physical Review B, vol. 93, (14), pp. 144509, 2016.

104. J. Hsu and A. Kapitulnik, "Superconducting transition, fluctuation, and vortex motion in a two-dimensional single-crystal Nb film," Physical Review B, vol. 45, (9), pp. 4819, 1992.

105. A. V. Matetskiy et al, "Two-dimensional superconductor with a giant Rashba effect: One-atom-layer Tl-Pb compound on Si (111)," Phys. Rev. Lett., vol. 115, (14), pp. 147003, 2015.

106. W. Zhao et al, "Evidence for Berezinskii–Kosterlitz–Thouless transition in atomically flat two-dimensional Pb superconducting films," Solid State Commun., vol. 165, pp. 59-63, 2013.

107. H. Zhang et al, "Detection of a superconducting phase in a two-atom layer of hexagonal Ga film grown on semiconducting GaN (0001)," Phys. Rev. Lett., vol. 114, (10), pp. 107003, 2015.

108. Y. Saito, T. Nojima and Y. Iwasa, "Highly crystalline 2D superconductors," Nature Reviews Materials, vol. 2, (1), pp. 1-18, 2016.

109. D. B. Haviland, Y. Liu and A. M. Goldman, "Onset of superconductivity in the two-dimensional limit," Phys. Rev. Lett., vol. 62, (18), pp. 2180, 1989.

110. A. Yazdani and A. Kapitulnik, "Superconducting-insulating transition in two-dimensional a-MoGe thin films," Phys. Rev. Lett., vol. 74, (15), pp. 3037, 1995.

111. C. Yang et al, "Intermediate bosonic metallic state in the superconductor-insulator transition," Science, vol. 366, (6472), pp. 1505-1509, 2019.

112. N. Mason and A. Kapitulnik, "Dissipation effects on the superconductor-insulator transition in 2D superconductors," Phys. Rev. Lett., vol. 82, (26), pp. 5341, 1999.

113. Y. Saito et al, "Metallic ground state in an ion-gated two-dimensional superconductor," Science, vol. 350, (6259), pp. 409-413, 2015.

114. A. W. Tsen et al, "Nature of the quantum metal in a two-dimensional crystalline superconductor," Nature Physics, vol. 12, (3), pp. 208-212, 2016.

115. M. A. Steiner, N. P. Breznay and A. Kapitulnik, "Approach to a superconductor-to-Bose-insulator transition in disordered films," Physical Review B, vol. 77, (21), pp. 212501, 2008.

116. M. Tinkham et al, "Hysteretic I− V curves of superconducting nanowires," Physical Review B, vol. 68, (13), pp. 134515, 2003.

117. D. G. Schweitzer, M. Garber and B. Bertman, "Hysteresis in Superconductors. I. Flux Trapping in Low-and High-κ Materials," Physical Review, vol. 159, (2), pp. 296, 1967.

118. C. P. Bean, "Magnetization of high-field superconductors," Reviews of Modern Physics, vol. 36, (1), pp. 31, 1964.

119. I. Edmond and L. D. Firth, "Hysteresis in a high-temperature superconductor," Journal of Physics: Condensed Matter, vol. 4, (14), pp. 3813, 1992.

120. A. Ballestar et al, "Josephson-coupled superconducting regions embedded at the interfaces of highly oriented pyrolytic graphite," New Journal of Physics, vol. 15, (2), pp. 023024, 2013.

121. A. N. Ionov et al, "The magnetization of a composite based on reduced graphene oxide and polystyrene," Nanomaterials, vol. 11, (2), pp. 403, 2021.

122. J. Gil-Pinzon et al, "Evidence of vortices and mixed-state superconductivity in phosphorus-doped graphene. Part II (Hysteresis)," Superconductor Science and Technology, vol. 34, (3), pp. 035023, 2021.

123. H. Grabert and M. H. Devoret, Single Charge Tunneling: Coulomb Blockade Phenomena in Nanostructures. 2013294.

124. D. B. Haviland, Y. Liu and A. M. Goldman, "Onset of superconductivity in the two-dimensional limit," Phys. Rev. Lett., vol. 62, (18), pp. 2180, 1989.

125. A. M. Finkel'Shtein, "Superconductivity-transition temperature in amorphous films," Pisma V Zhurnal Eksperimentalnoi i Teoreticheskoi Fiziki, vol. 45, pp. 37-40, 1987.

126. M. V. Feigel'Man et al, "Fractal superconductivity near localization threshold," Annals of Physics, vol. 325, (7), pp. 1390-1478, 2010.

127. D. Eom et al, "Persistent superconductivity in ultrathin Pb films: A scanning tunneling spectroscopy study," Phys. Rev. Lett., vol. 96, (2), pp. 027005, 2006.

128. C. Brun et al, "Reduction of the superconducting gap of ultrathin Pb islands grown on Si (111)," Phys. Rev. Lett., vol. 102, (20), pp. 207002, 2009.

129. J. Noffsinger and M. L. Cohen, "First-principles calculation of the electron-phonon coupling in ultrathin Pb superconductors: Suppression of the transition temperature by surface phonons," Physical Review B, vol. 81, (21), pp. 214519, 2010.

130. M. Schackert et al, "Local measurement of the Eliashberg function of Pb islands: Enhancement of electron-phonon coupling by quantum well states," Phys. Rev. Lett., vol. 114, (4), pp. 047002, 2015.

131. J. M. Blatt and C. J. Thompson, "Shape resonances in superconducting thin films," Phys. Rev. Lett., vol. 10, (8), pp. 332, 1963.

132. A. A. Shanenko, M. D. Croitoru and F. M. Peeters, "Oscillations of the superconducting temperature induced by quantum well states in thin metallic films: Numerical solution of the Bogoliubov–de Gennes equations," Physical Review B, vol. 75, (1), pp. 014519, 2007.

133. D. Valentinis, D. Van Der Marel and C. Berthod, "BCS superconductivity near the band edge: Exact results for one and several bands," Physical Review B, vol. 94, (2), pp. 024511, 2016.

134. D. Valentinis, D. Van Der Marel and C. Berthod, "Rise and fall of shape resonances in thin films of BCS superconductors," Physical Review B, vol. 94, (5), pp. 054516, 2016.

135. T. Horide et al, "Flux pinning properties of YBCO thin films deposited on SrTiO3 (1 0 0) and MgO (1 0 0) substrates," Physica C: Superconductivity, vol. 412, pp. 1291-1295, 2004.

136. A. K. Jha and N. Khare, "Strongly enhanced pinning force density in YBCO–BaTiO3 nanocomposite superconductor," Physica C: Superconductivity, vol. 469, (14), pp. 810-813, 2009.

137. R. E. Hummel, Electronic Properties of Materials. 2011.

138. R. E. Cohen, "Origin of ferroelectricity in perovskite oxides," Nature, vol. 358, (6382), pp. 136-138, 1992.

139. G. H. Haertling, "Ferroelectric thin films for electronic applications," Journal of Vacuum Science & Technology A: Vacuum, Surfaces, and Films, vol. 9, (3), pp. 414-420, 1991.

140. M. Tinkham, Introduction to Superconductivity. 2004.

141. U. Kabasawa, K. Asano and T. Kobayashi, "Electric Field Effect on the Al-MgO-YBa2Cu3Oy Structure," Japanese Journal of Applied Physics, vol. 29, (1A), pp. L86, 1990.

142. A. T. Fiory et al, "Metallic and superconducting surfaces of YBa 2 Cu 3 O 7 probed by electrostatic charge modulation of epitaxial films," Phys. Rev. Lett., vol. 65, (27), pp. 3441, 1990.

143. J. Mannhart et al, "Influence of electric fields on pinning in YBa 2 Cu 3 O 7− δ films," Phys. Rev. Lett., vol. 67, (15), pp. 2099, 1991.

144. X. X. Xi et al, "Effects of field-induced hole-density modulation on normal-state and superconducting transport in YBa 2 Cu 3 O 7− x," Phys. Rev. Lett., vol. 68, (8), pp. 1240, 1992.

145. A. Walkenhorst et al, "Electric field effects on vortex dynamics in ultrathin YBa 2 Cu 3 O 7− δ films," Phys. Rev. Lett., vol. 69, (18), pp. 2709, 1992.

146. J. Mannhart, "Changes in the Superconducting Properties of High-T c Cuprates Produced by Applied Electric Fields," Modern Physics Letters B, vol. 6, (10), pp. 555-571, 1992.

147. G. L Larkins et al, “Shifts in T_c of multilayer ferroelectric high T_c structures with poled ferroelectric layers,” Applied superconductivity, vol. 2, (8),pp. 1637-1640, 1993

148. G. L. Larkins et al, "Multilayer ferroelectric-high T/sub c/structures with poled ferroelectric layers," IEEE Trans. Appl. Supercond., vol. 5, (2), pp. 3049-3052, 1995.

149. V. V. Lemanov, A. L. Kholkin and A. B. Sherman, "YBCO thin films on ferroelectric substrates: the polarization-induced changes of superconductive properties," Superconductor Science and Technology, vol. 6, (12), pp. 814, 1993.

150. C. H. Ahn et al, "Electrostatic modulation of superconductivity in ultrathin GdBa2Cu3O7-x films," Science, vol. 284, (5417), pp. 1152-1155, 1999.

151. D. Matthey et al, "Electric-field-effect modulation of the transition temperature, mobile carrier density, and in-plane penetration depth of ndba 2 cu 3 o 7− δ thin films," Phys. Rev. Lett., vol. 98, (5), pp. 057002, 2007.

152. A. Crassous et al, "Nanoscale electrostatic manipulation of magnetic flux quanta in ferroelectric/superconductor BiFeO 3/YBa 2 Cu 3 O 7− δ heterostructures," Phys. Rev. Lett., vol. 107, (24), pp. 247002, 2011.

153. V. V. Lemanov, A. L. Kholkin and A. B. Sherman, "Effect of the spontaneous polarization of ferroelectric substrates on the electrical properties of films," Pisma V Zhurnal Eksperimentalnoi i Teoreticheskoi Fiziki, vol. 56, (11), pp. 580-583, 1992.

154. N. Pavlenko, "Modulation of superconductivity by ferroelectric polarization in confined ferroelectric-superconductor-ferroelectric films," Physical Review B, vol. 70, (9), pp. 094519, 2004.

155. M. A. Rahman, M. Z. Rahaman and M. N. Samsuddoha, "A review on cuprate based superconducting materials including characteristics and applications," American Journal of Physics and Applications, vol. 3, (2), pp. 39-56, 2015.

156. R. J. Cava, "Oxide superconductors," J Am Ceram Soc, vol. 83, (1), pp. 5-28, 2000.

157. J. G. Bednorz and K. A. Müller, "Possible high T c superconductivity in the Ba− La− Cu− O system," Zeitschrift Für Physik B Condensed Matter, vol. 64, (2), pp. 189-193, 1986.

158. M. Wu et al, "Superconductivity at 93 K in a new mixed-phase Y-Ba-Cu-O compound system at ambient pressure," Phys. Rev. Lett., vol. 58, (9), pp. 908, 1987.

159. C. Michel et al, "Superconductivity in the Bi-Sr-Cu-O system," Zeitschrift Für Physik B Condensed Matter, vol. 68, (4), pp. 421-423, 1987.

160. Z. Z. Sheng and A. M. Hermann, "Bulk superconductivity at 120 K in the Tl–Ca/Ba–Cu–O system," Nature, vol. 332, (6160), pp. 138-139, 1988.

161. M. Sakoda, K. Iida and M. Naito, "Recent progress in thin-film growth of Fe-based superconductors: superior superconductivity achieved by thin films," Superconductor Science and Technology, vol. 31, (9), pp. 093001, 2018.

162. H. Hosono et al, "Recent advances in iron-based superconductors toward applications," Materials Today, vol. 21, (3), pp. 278-302, 2018.

163. S. Haindl et al, "Thin film growth of Fe-based superconductors: from fundamental properties to functional devices. A comparative review," Reports on Progress in Physics, vol. 77, (4), pp. 046502, 2014.

164. S. Haindl et al, "Recent progress in pulsed laser deposition of iron based superconductors," J. Phys. D, vol. 49, (34), pp. 345301, 2016.

165. S. Adachi et al, "Pulsed laser deposition of BaFe2 (As, P) 2 superconducting thin films with high critical current density," Superconductor Science and Technology, vol. 25, (10), pp. 105015, 2012.

166. K. Chang et al, "Molecular beam epitaxy growth of superconducting LiFeAs film on SrTiO3 (001) substrate," EPL (Europhysics Letters), vol. 109, (2), pp. 28003, 2015.

167. L. Chen et al, "Enhanced flux pinning properties in superconducting FeSe0. 5Te0. 5 thin films with secondary phases," Superconductor Science and Technology, vol. 25, (2), pp. 025020, 2012.

168. S. Jung et al, "Fabrication of cobalt-doped SrFe2As2 superconducting thin films," Physica C: Superconductivity and its Applications, vol. 470, pp. S511-S512, 2010.

169. N. B. Hannay et al, "Superconductivity in graphitic compounds," Phys. Rev. Lett., vol. 14, (7), pp. 225, 1965.

170. K. Antonowicz, "Possible superconductivity at room temperature," Nature, vol. 247, (5440), pp. 358-360, 1974.

171. H. Kempa et al, "Magnetic-field-driven superconductor–insulator-type transition in graphite," Solid State Commun., vol. 115, (10), pp. 539-542, 2000.

172. A. Ballestar et al, "Josephson-coupled superconducting regions embedded at the interfaces of highly oriented pyrolytic graphite," New Journal of Physics, vol. 15, (2), pp. 023024, 2013.

173. P. Esquinazi et al, "Indications for intrinsic superconductivity in highly oriented pyrolytic graphite," Physical Review B, vol. 78, (13), pp. 134516, 2008.

174. H. B. Heersche et al, "Induced superconductivity in graphene," Solid State Commun., vol. 143, (1-2), pp. 72-76, 2007.

175. B. Uchoa and A. C. Neto, "Superconducting states of pure and doped graphene," Phys. Rev. Lett., vol. 98, (14), pp. 146801, 2007.

176. G. Profeta, M. Calandra and F. Mauri, "Phonon-mediated superconductivity in graphene by lithium deposition," Nature Physics, vol. 8, (2), pp. 131-134, 2012.

177. J. Chapman et al, "Superconductivity in Ca-doped graphene laminates Sci," 2016.

178. K. Li et al, "Superconductivity in Ca-intercalated epitaxial graphene on silicon carbide," Appl. Phys. Lett., vol. 103, (6), pp. 062601, 2013.

179. A. H. MacDonald and R. Bistritzer, "Graphene moiré mystery solved?" Nature, vol. 474, (7352), pp. 453-454, 2011.

180. A. Luican et al, "Single-layer behavior and its breakdown in twisted graphene layers," Phys. Rev. Lett., vol. 106, (12), pp. 126802, 2011.

181. Y. Cao et al, "Unconventional superconductivity in magic-angle graphene superlattices," Nature, vol. 556, (7699), pp. 43-50, 2018.

182. X. Liu et al, "Spin-polarized correlated insulator and superconductor in twisted double bilayer graphene," arXiv Preprint arXiv:1903.08130, 2019.

183. L. Jauregui et al, "Superconductivity in twisted transition metal dichalcogenide homobilayers," in APS March Meeting Abstracts, 2019.

184. T. Holstein, "Studies of polaron motion: Part I. The molecular-crystal model," Annals of Physics, vol. 8, (3), pp. 325-342, 1959.

185. I. Martin, "Moiré superconductivity," Annals of Physics, vol. 417, pp. 168118, 2020.

186. P. Morel and P. W. Anderson, "Calculation of the superconducting state parameters with retarded electron-phonon interaction," Physical Review, vol. 125, (4), pp. 1263, 1962.

187. L. Wang et al, "One-dimensional electrical contact to a two-dimensional material," Science, vol. 342, (6158), pp. 614-617, 2013.

188. V. L. Ginzburg, "On the theory of superconductivity," Il Nuovo Cimento (1955-1965), vol. 2, (6), pp. 1234-1250, 1955.

189. M. Yankowitz et al, "Tuning superconductivity in twisted bilayer graphene," Science, vol. 363, (6431), pp. 1059-1064, 2019.

190. M. Ohring, Materials Science of Thin Films. 2001.

191. M. H. Rümmeli et al, "Graphene: Piecing it together," Adv Mater, vol. 23, (39), pp. 4471-4490, 2011.

192. K. S. Novoselov et al, "Two-dimensional atomic crystals," Proceedings of the National Academy of Sciences, vol. 102, (30), pp. 10451-10453, 2005.

193. G. Larkins and Y. Vlasov, "Indications of superconductivity in doped highly oriented pyrolytic graphite," Superconductor Science and Technology, vol. 24, (9), pp. 092001, 2011.

194. G. Larkins, Y. Vlasov and K. Holland, "Periodic steps in the resistance vs. temperature characteristics of doped graphite and graphene: evidence of superconductivity?" arXiv Preprint arXiv:1307.0581, 2013.

195. G. Larkins, Y. Vlasov and K. Holland, "Evidence of superconductivity in doped graphite and graphene," Superconductor Science and Technology, vol. 29, (1), pp. 015015, 2015.

196. K. Holland, "Doping as a Possible Means to create Superconductivity in Graphene," 2016.

197. S. J. Hagen et al, "Flux-flow Hall effect in superconducting Tl 2 Ba 2 CaCu 2 O 8 films," Physical Review B, vol. 43, (7), pp. 6246, 1991.

198. N. B. Kopnin, B. I. Ivlev and V. A. Kalatsky, "The flux-flow Hall effect in type II superconductors. An explanation of the sign reversal," J. Low Temp. Phys., vol. 90, (1), pp. 1-13, 1993.

199. N. B. Kopnin and A. V. Lopatin, "Flux-flow Hall effect in clean type-II superconductors," Physical Review B, vol. 51, (21), pp. 15291, 1995.

200. A. Oral, S. J. Bending and M. Henini, "Scanning Hall probe microscopy of superconductors and magnetic materials," Journal of Vacuum Science & Technology B: Microelectronics and Nanometer Structures Processing, Measurement, and Phenomena, vol. 14, (2), pp. 1202-1205, 1996.

201. J. M. García-Martín et al, "Imaging magnetic vortices by magnetic force microscopy: experiments and modelling," J. Phys. D, vol. 37, (7), pp. 965, 2004.

202. L. N. Vu, M. S. Wistrom and D. J. Van Harlingen, "Imaging of magnetic vortices in superconducting networks and clusters by scanning SQUID microscopy," Appl. Phys. Lett., vol. 63, (12), pp. 1693-1695, 1993.

203. V. V. Moshchalkov et al, "Magnetization of multiple-quanta vortex lattices," Physical Review B, vol. 54, (10), pp. 7385, 1996.

204. N. Sornkhampan, "Study of Charge Carrier Transport in Graphene and Graphite as Two Dimensional and Quasi-Two Dimensional Materials and Their Interfaces," 2019.

205. R. D. Parks et al, “Critical-field behavior of a microscopic superconducting bridge,” Physical Review Letters, vol. 13, (11), p.331, 1964

APPENDICES

APPENDIX 1

Equipment used

- F-70 Sumitomo Helium compressor

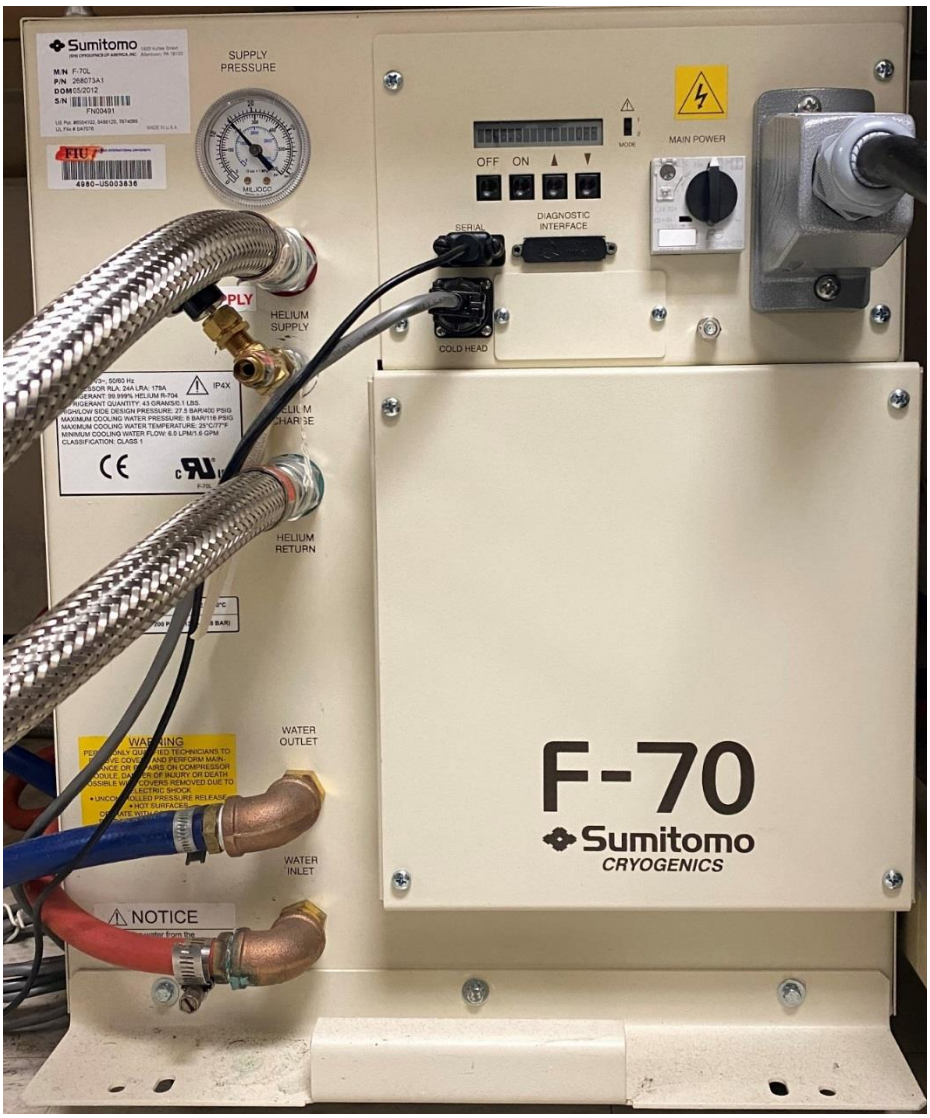

- Closed-cycle helium refrigerator

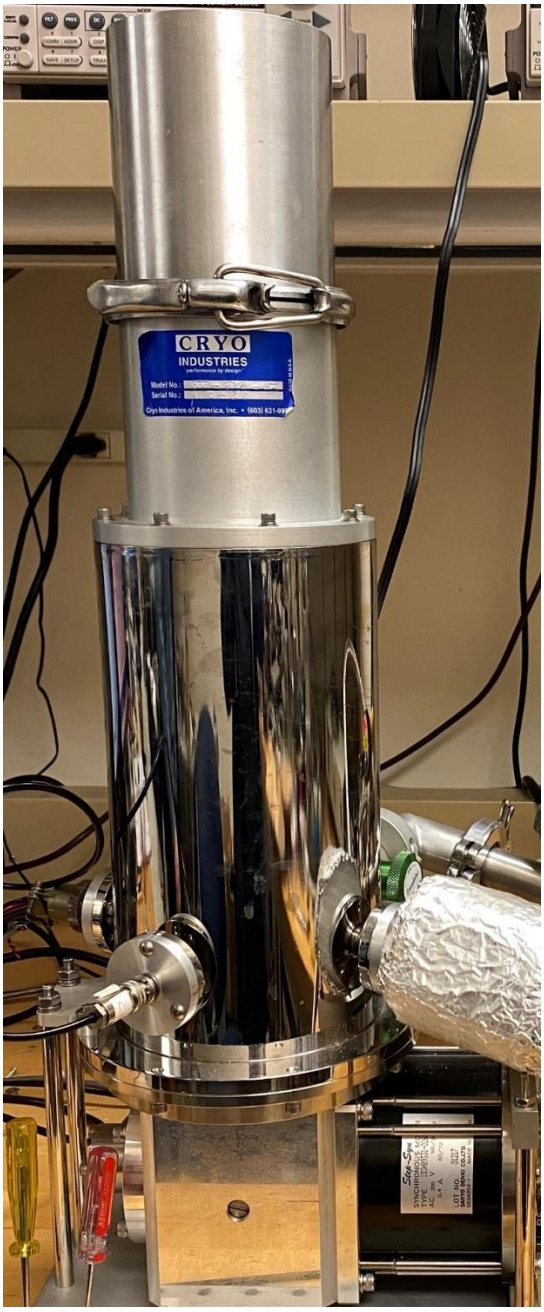

- Keithley 6221 current source (left) and Keithley 2182A Nanovoltmeter (right).

- Lakeshore 335 temperature controller

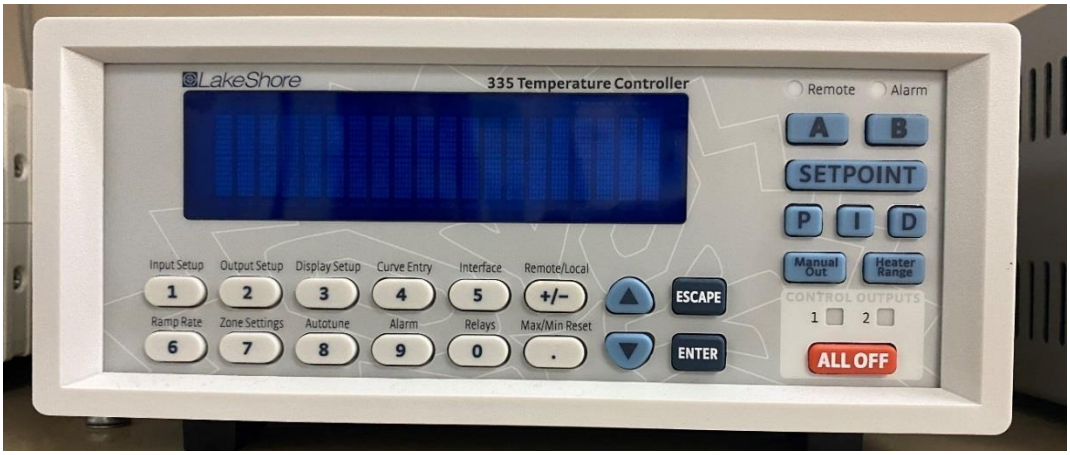

- PFEIFFER turbomolecular pump

APPENDIX 2

LABIEW PROGRAMS

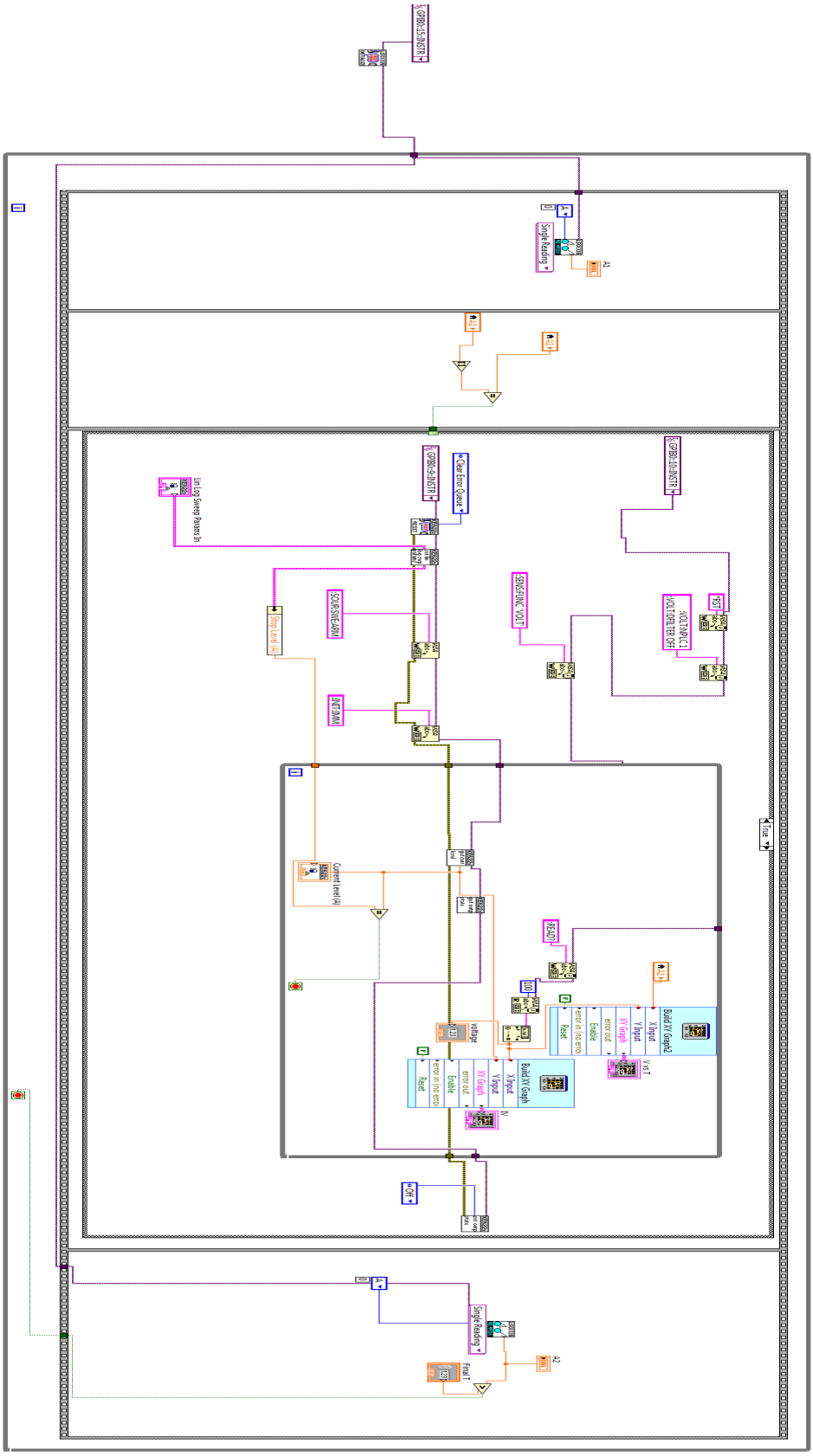
GPIB0::15::INSTR
Single Reading
A1
GPIB0::24::INSTR
Clear Error Queue
Lim Log Sweep Params In
Sweep Level (A)
SOURCEMEAMV
SENSEAMC VOLT
:VOLTAMPCC1
:VOLTAMPLTER OFF
*RST
RANGEMV
Current Level (A)
RESADJ
Build XY Graph2
Build XY Graph
voltage
Single Reading
A2
Final T
True

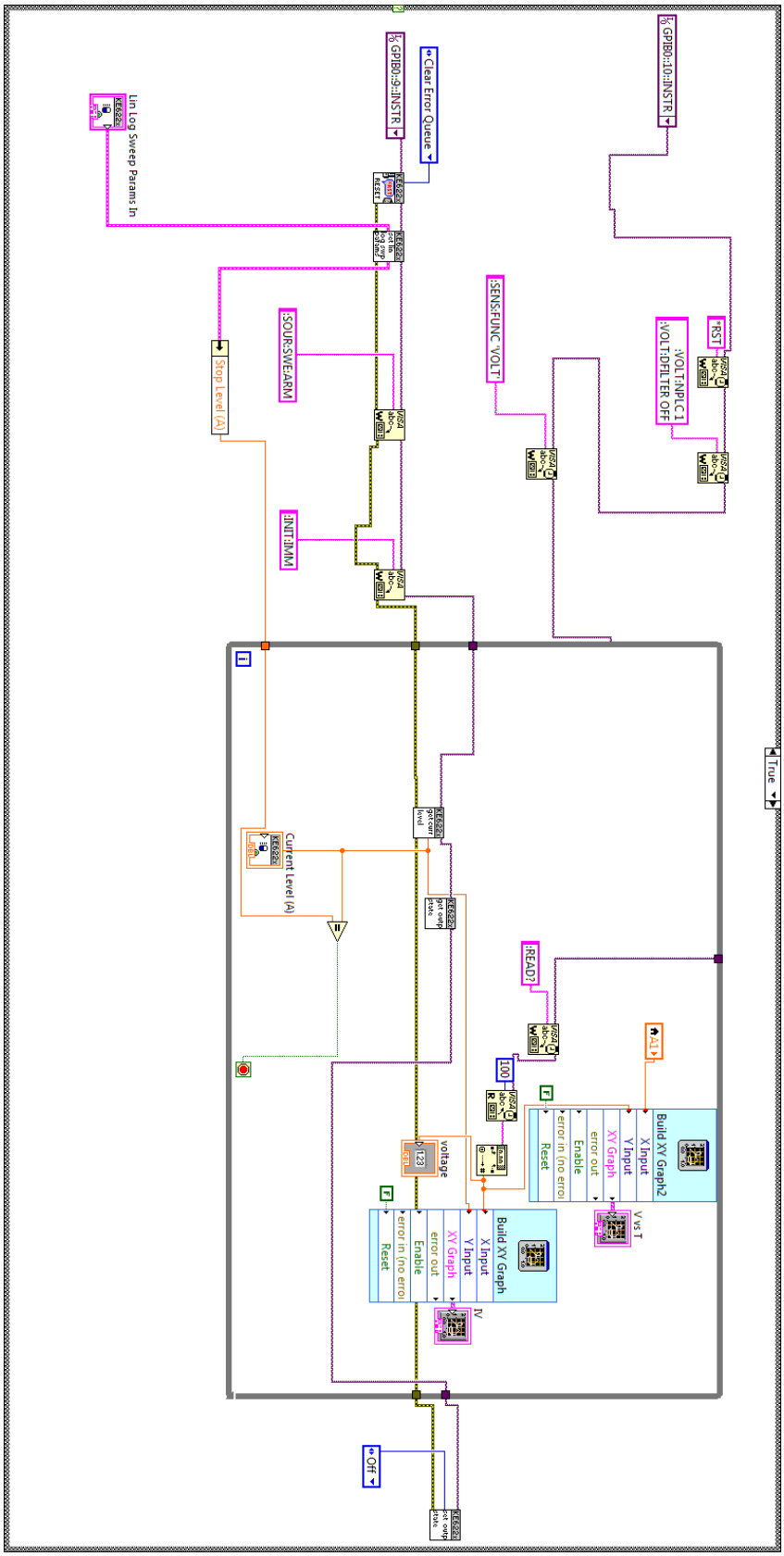
GPIB0::10::INSTR
GPIB0::9::INSTR
Clear Error Queue
Lin Log Sweep Params In
*RST
:VOLT:NPLC 1
:VOLT:DFLTER OFF
:SENS:FUNC 'VOLT'
:SOUR:SWEARM
Stop Level (A)
:INIT:IMM
:READ?
100
Current Level (A)
voltage
Build XY Graph2
Build XY Graph
X Input
Y Input
XY Graph
error out
Enable
Reset
error in (no error)
V vs T
IV
Off
True

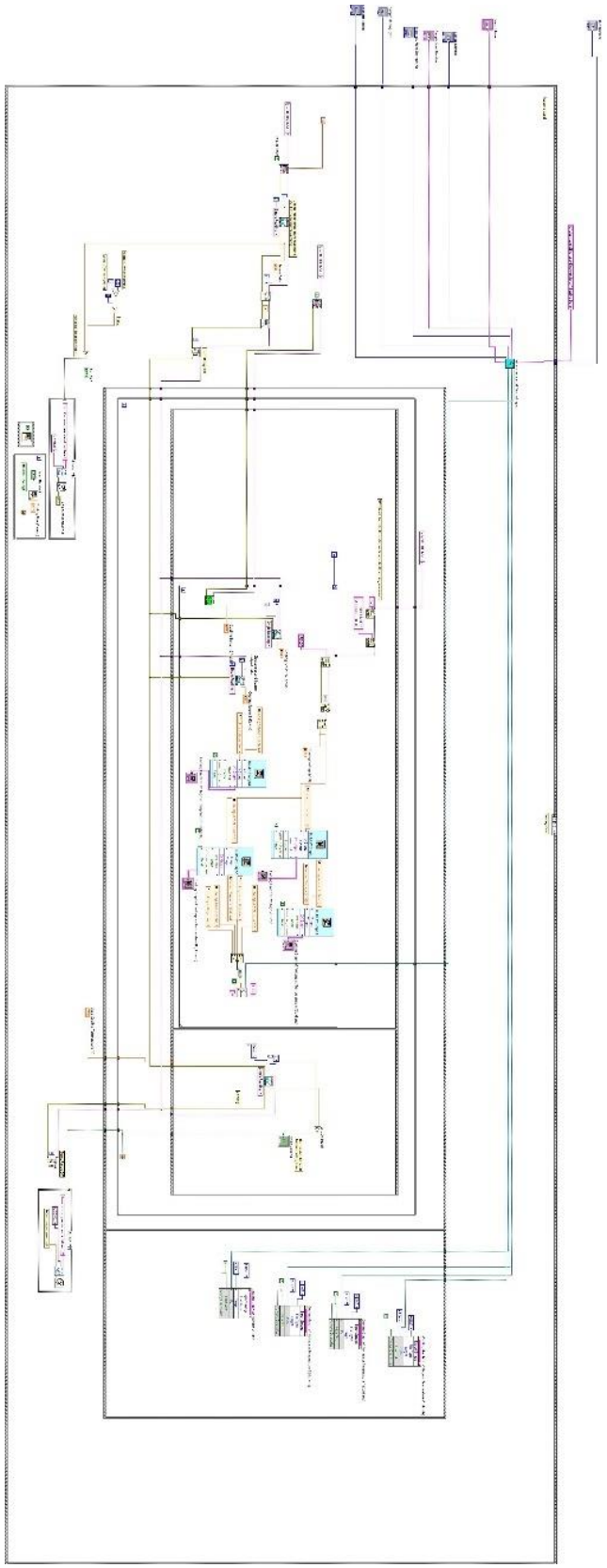

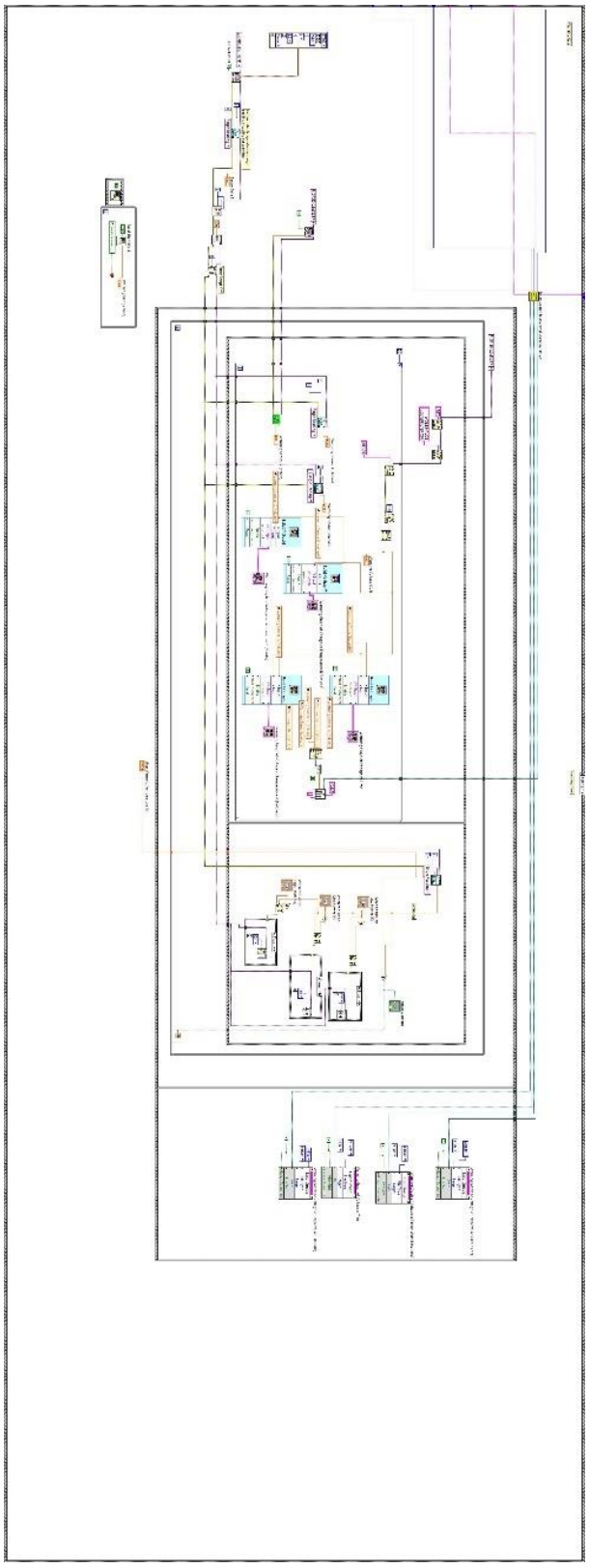

APPENDIX 3

PLOTS

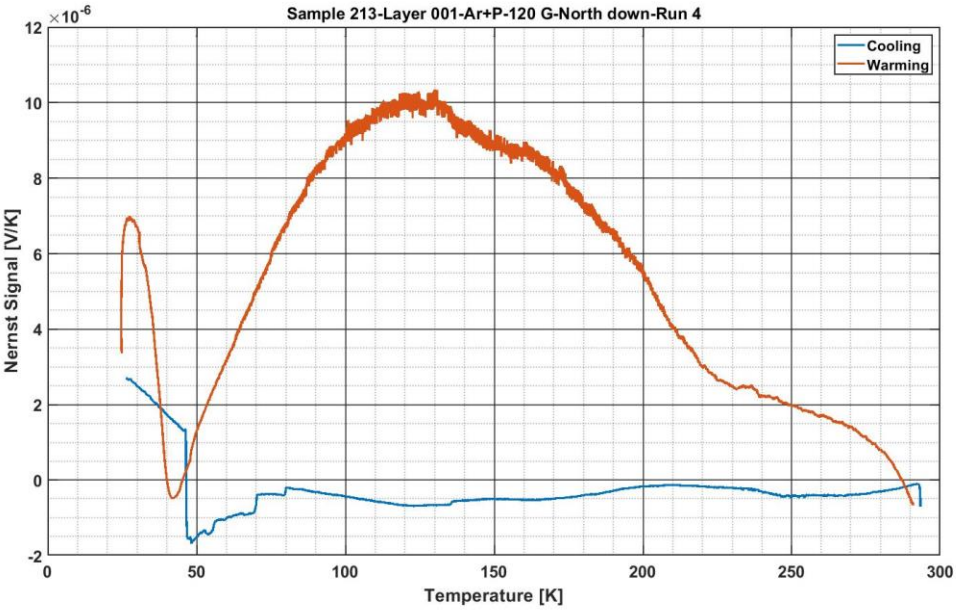
Sample 213-Layer 001-Ar+P-120 G-North down-Run 4
×10^-6
Cooling
Warming
Nernst Signal [V/K]
Temperature [K]
12
10
8
6
4
2
0
-2
0
50
100
150
200
250
300

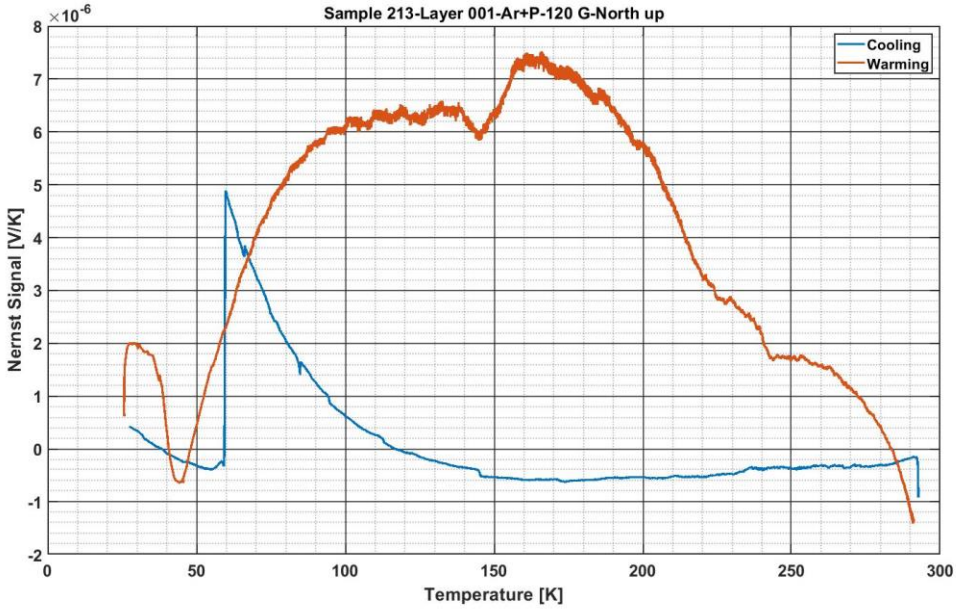
Sample 213-Layer 001-Ar+P-120 G-North up
×10^-6
Cooling
Warming
Nernst Signal [V/K]
Temperature [K]
8
7
6
5
4
3
2
1
0
-1
-2
0
50
100
150
200
250
300

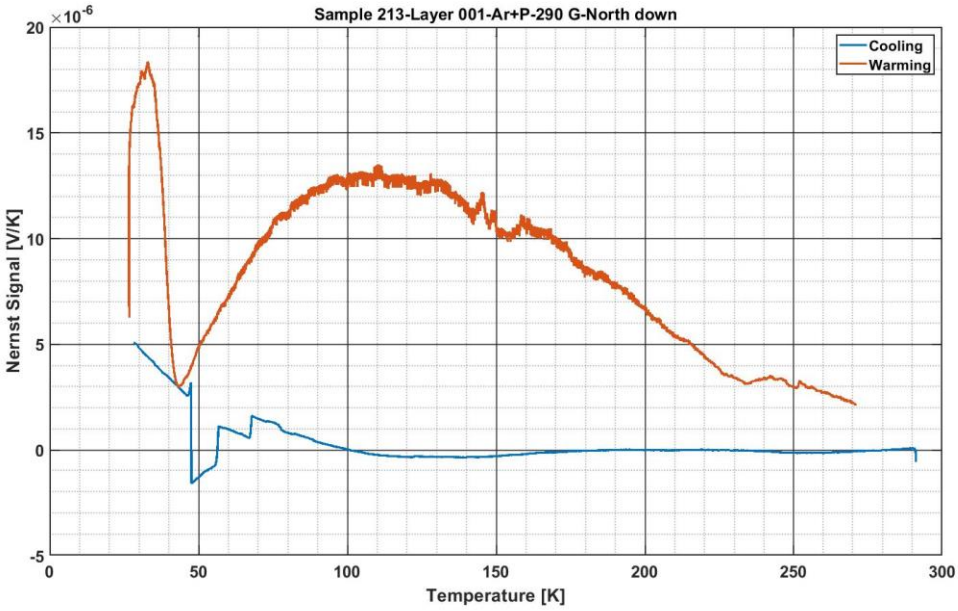
Sample 213-Layer 001-Ar+P-290 G-North down
×10^-6
Cooling
Warming
Nernst Signal [V/K]
Temperature [K]
20
15
10
5
0
-5
0
50
100
150
200
250
300

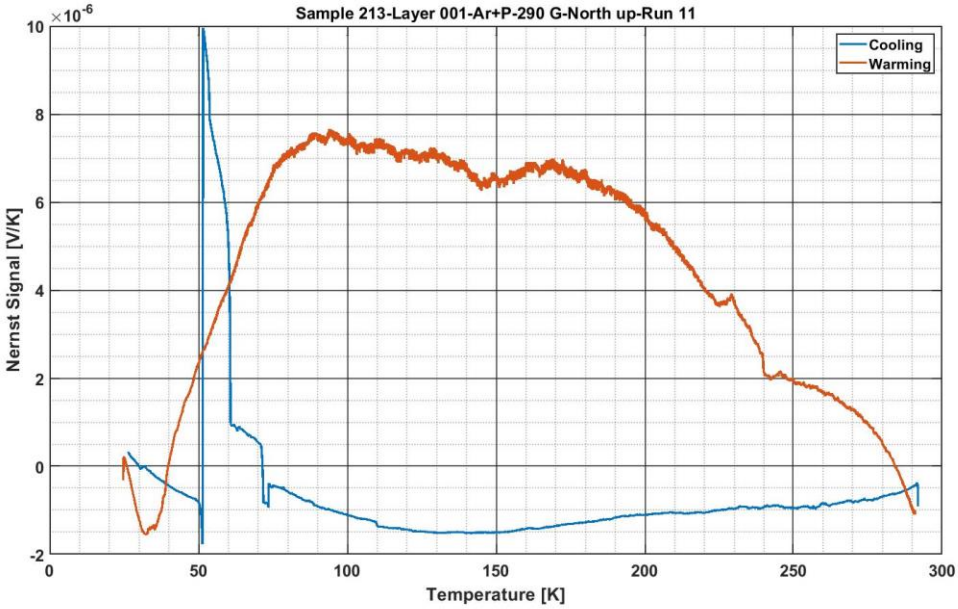
Sample 213-Layer 001-Ar+P-290 G-North up-Run 11
×10^-6
Cooling
Warming
Nernst Signal [V/K]
Temperature [K]
10
8
6
4
2
0
-2
0
50
100
150
200
250
300

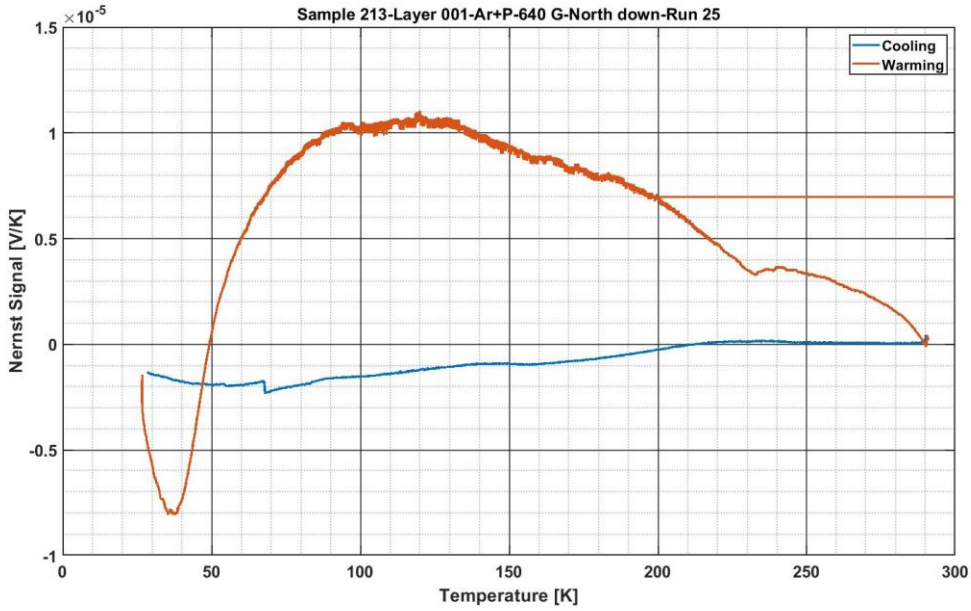
Sample 213-Layer 001-Ar+P-640 G-North down-Run 25
×10^-5
Cooling
Warming
Nernst Signal [V/K]
Temperature [K]
1.5
1
0.5
0
-0.5
-1
0
50
100
150
200
250
300

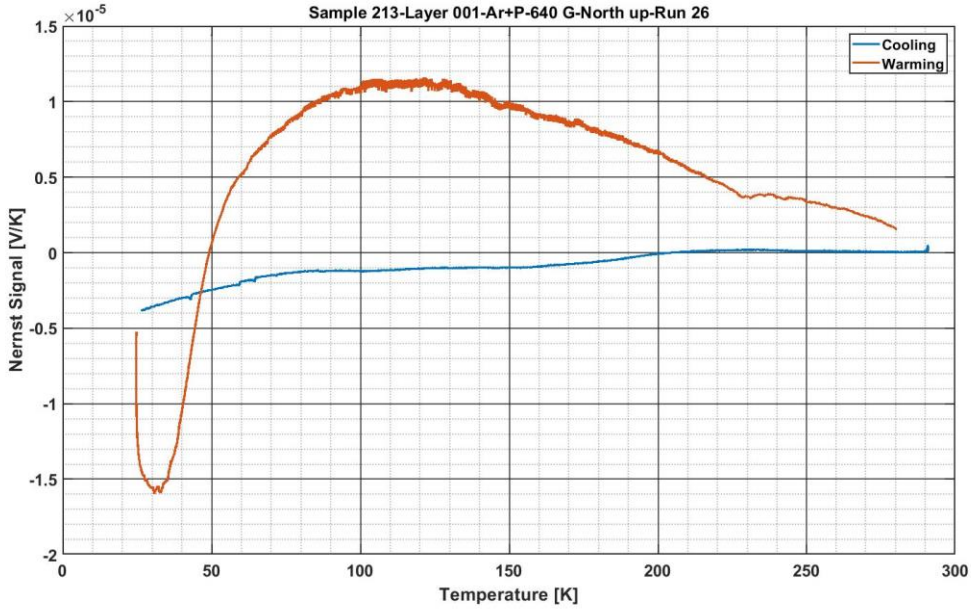
Sample 213-Layer 001-Ar+P-640 G-North up-Run 26
×10^-5
Cooling
Warming
Nernst Signal [V/K]
Temperature [K]
1.5
1
0.5
0
-0.5
-1
-1.5
-2
0
50
100
150
200
250
300

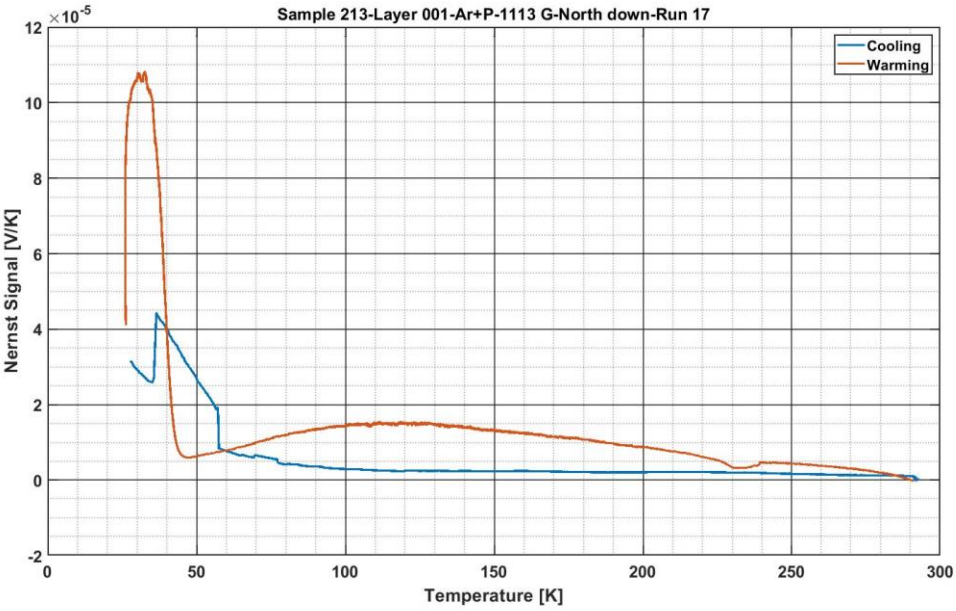
Sample 213-Layer 001-Ar+P-1113 G-North down-Run 17
×10^-5
Cooling
Warming
Nernst Signal [V/K]
Temperature [K]
12
10
8
6
4
2
0
-2
0
50
100
150
200
250
300

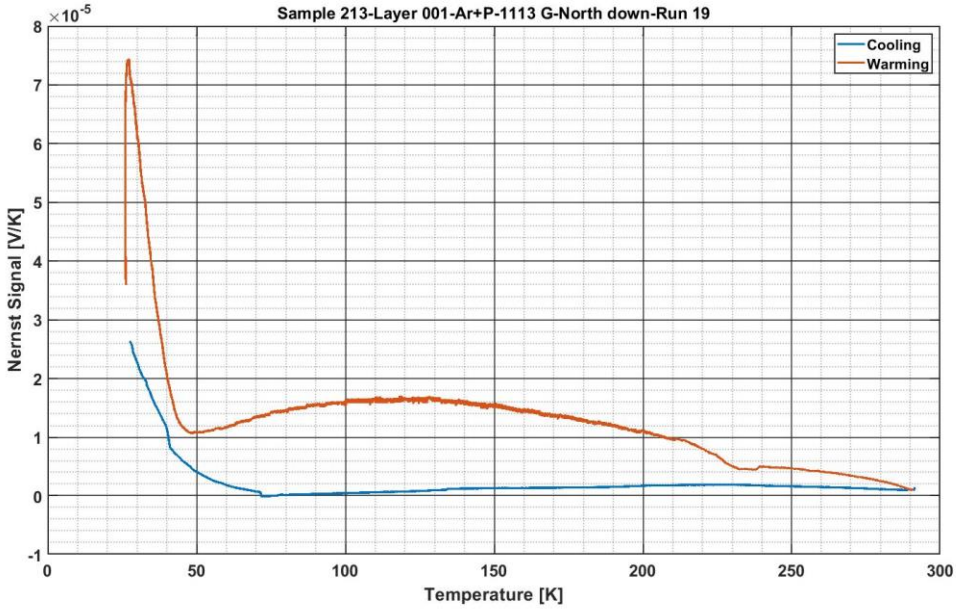
Sample 213-Layer 001-Ar+P-1113 G-North down-Run 19
×10^-5
Cooling
Warming
Nernst Signal [V/K]
Temperature [K]
8
7
6
5
4
3
2
1
0
-1
0
50
100
150
200
250
300

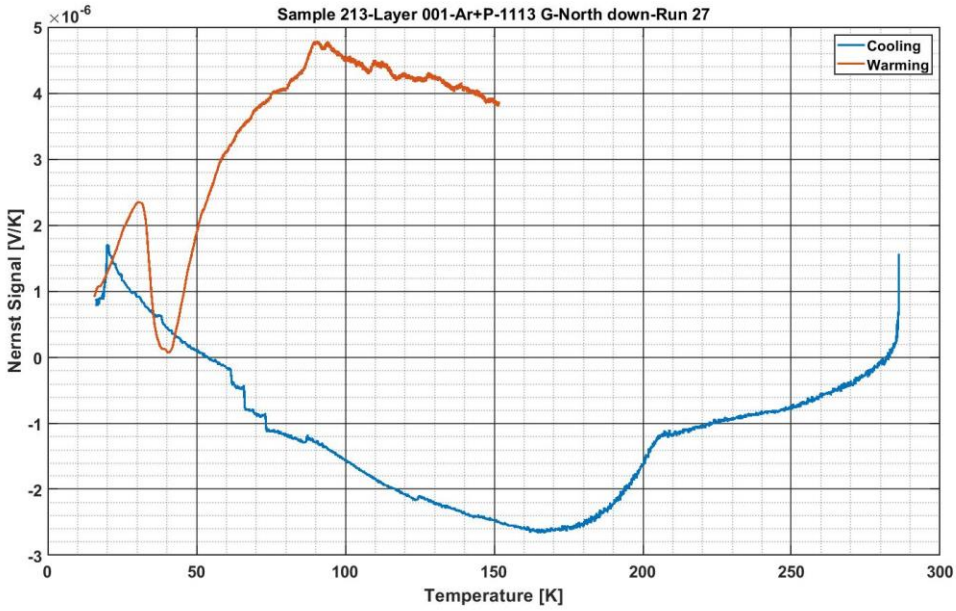
Sample 213-Layer 001-Ar+P-1113 G-North down-Run 27
×10^-6
Cooling
Warming
Nernst Signal [V/K]
Temperature [K]
5
4
3
2
1
0
-1
-2
-3
0
50
100
150
200
250
300

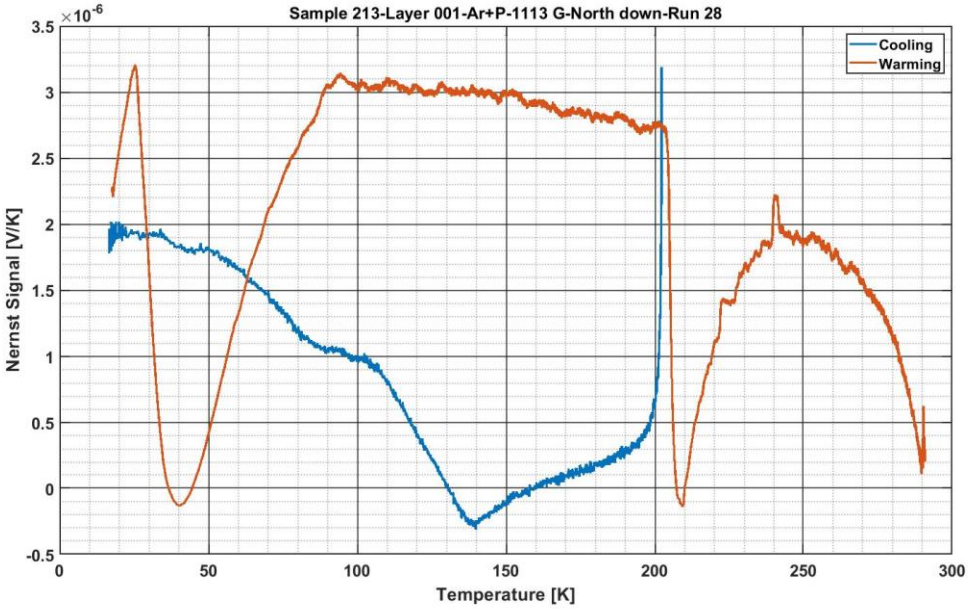
Sample 213-Layer 001-Ar+P-1113 G-North down-Run 28
×10^-6
Cooling
Warming
Nernst Signal [V/K]
Temperature [K]
3.5
3
2.5
2
1.5
1
0.5
0
-0.5
0
50
100
150
200
250
300

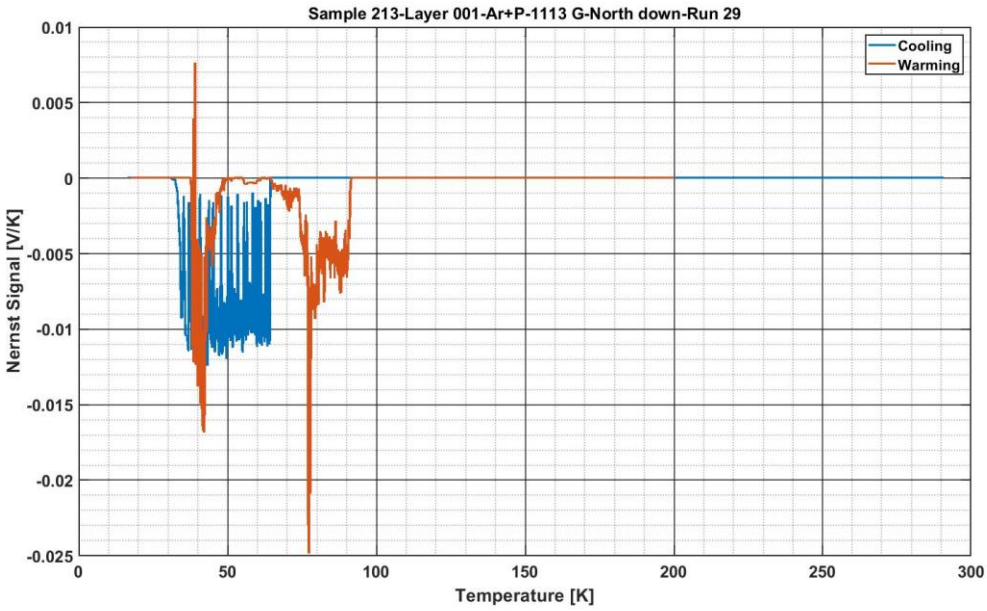
Sample 213-Layer 001-Ar+P-1113 G-North down-Run 29
Cooling
Warming
Nernst Signal [V/K]
Temperature [K]
0.01
0.005
0
-0.005
-0.01
-0.015
-0.02
-0.025
0
50
100
150
200
250
300

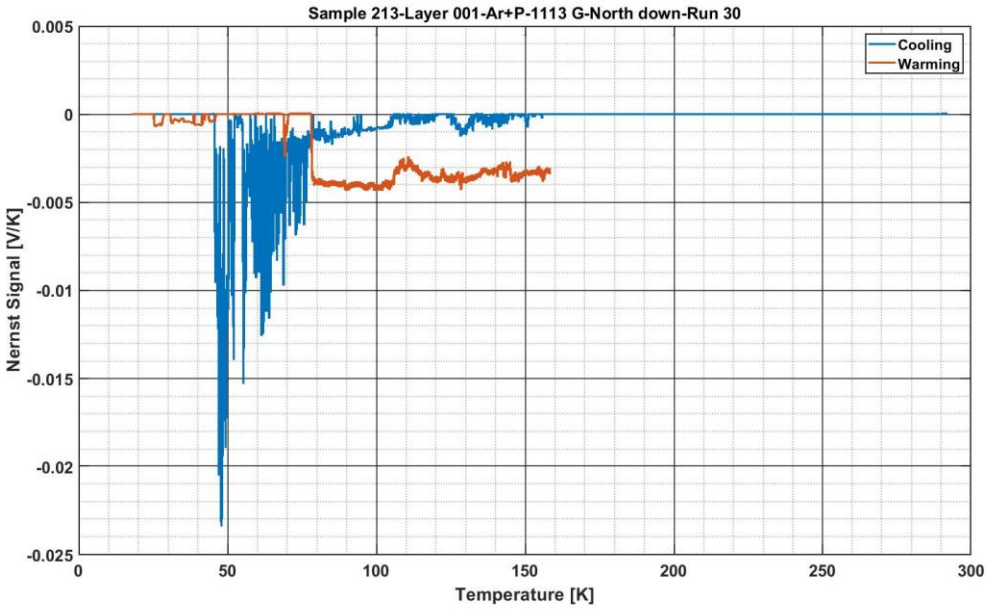
Sample 213-Layer 001-Ar+P-1113 G-North down-Run 30
Cooling
Warming
Nernst Signal [V/K]
Temperature [K]
0.005
0
-0.005
-0.01
-0.015
-0.02
-0.025
0
50
100
150
200
250
300

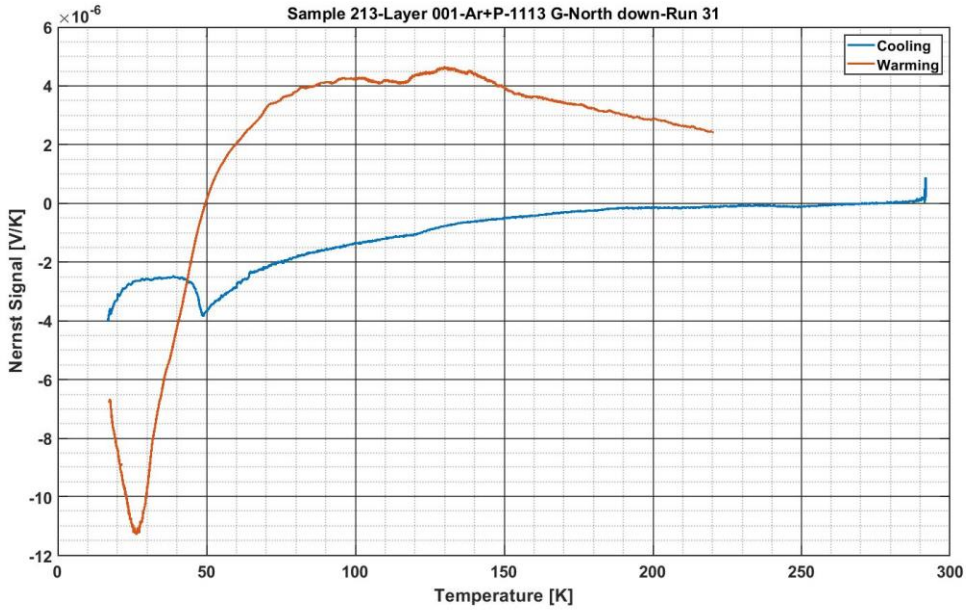
Sample 213-Layer 001-Ar+P-1113 G-North down-Run 31
×10^-6
Cooling
Warming
Nernst Signal [V/K]
Temperature [K]
6
4
2
0
-2
-4
-6
-8
-10
-12
0
50
100
150
200
250
300

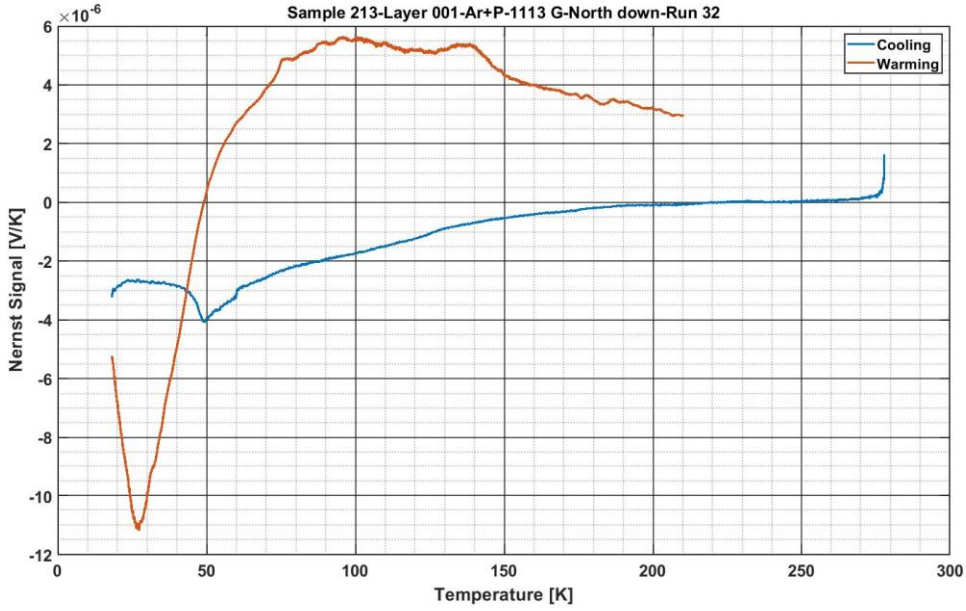
Sample 213-Layer 001-Ar+P-1113 G-North down-Run 32
×10^-6
Cooling
Warming
Nernst Signal [V/K]
Temperature [K]
6
4
2
0
-2
-4
-6
-8
-10
-12
0
50
100
150
200
250
300

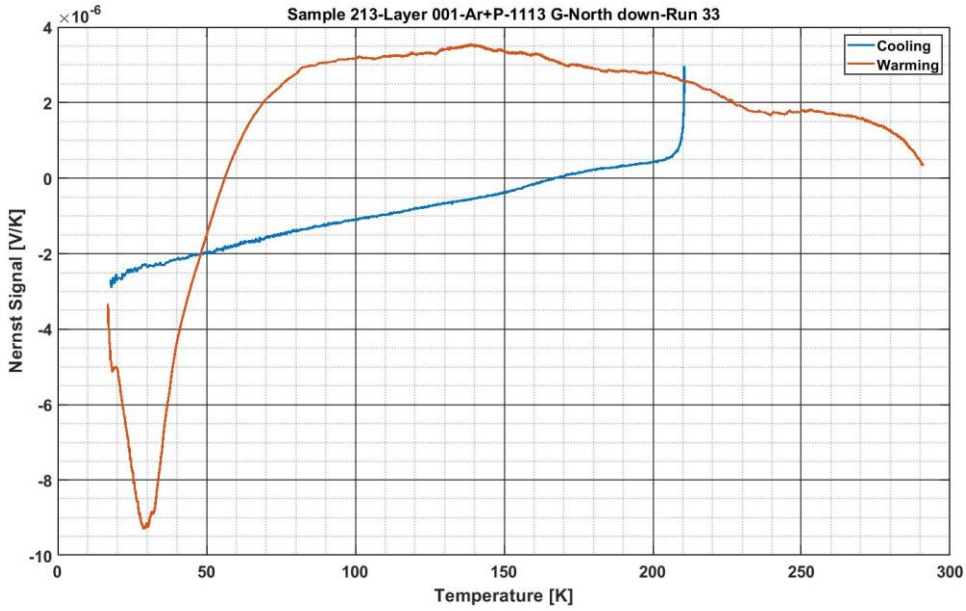
Sample 213-Layer 001-Ar+P-1113 G-North down-Run 33
×10^-6
Cooling
Warming
Nernst Signal [V/K]
Temperature [K]
4
2
0
-2
-4
-6
-8
-10
0
50
100
150
200
250
300

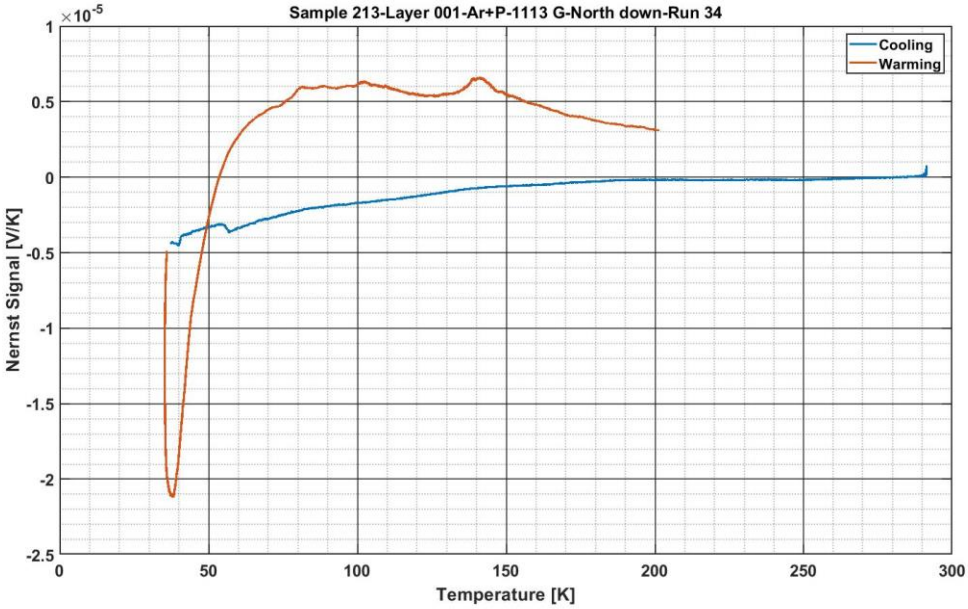
Sample 213-Layer 001-Ar+P-1113 G-North down-Run 34
×10^-5
Cooling
Warming
Nernst Signal [V/K]
Temperature [K]
1
0.5
0
-0.5
-1
-1.5
-2
-2.5
0
50
100
150
200
250
300

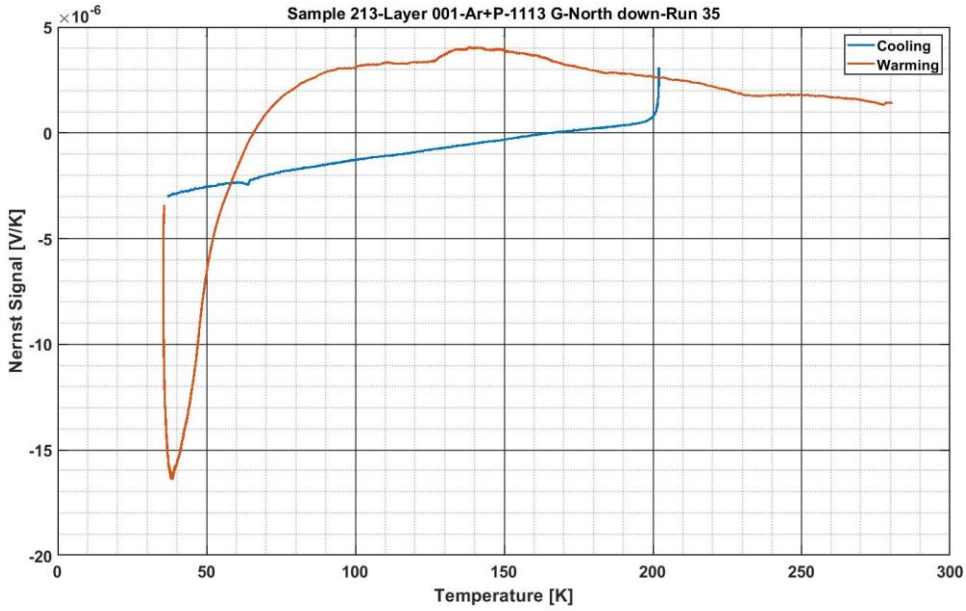
Sample 213-Layer 001-Ar+P-1113 G-North down-Run 35
×10^-6
Cooling
Warming
Nernst Signal [V/K]
Temperature [K]
5
0
-5
-10
-15
-20
0
50
100
150
200
250
300

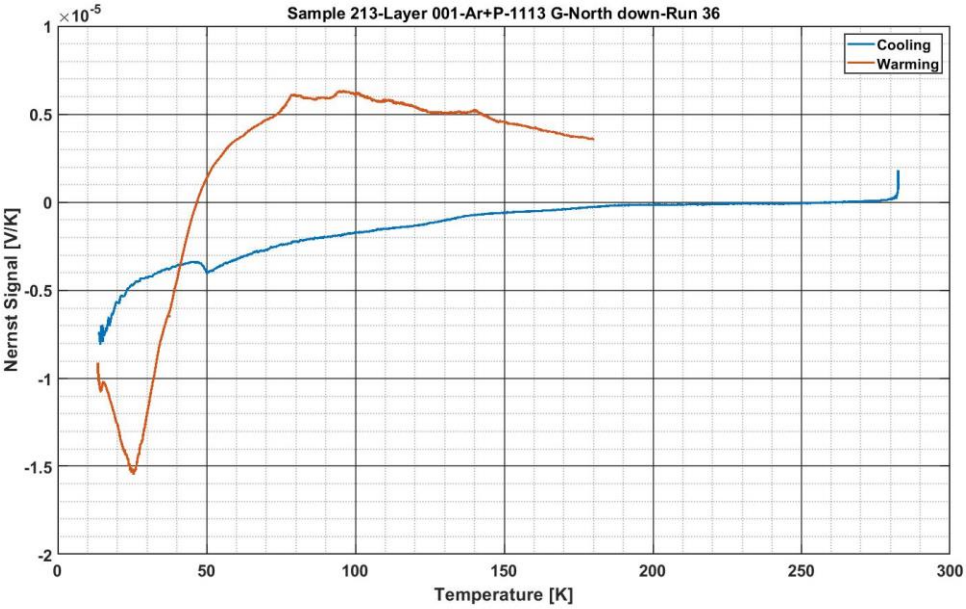
Sample 213-Layer 001-Ar+P-1113 G-North down-Run 36
×10^-5
Cooling
Warming
Nernst Signal [V/K]
Temperature [K]
1
0.5
0
-0.5
-1
-1.5
-2
0
50
100
150
200
250
300

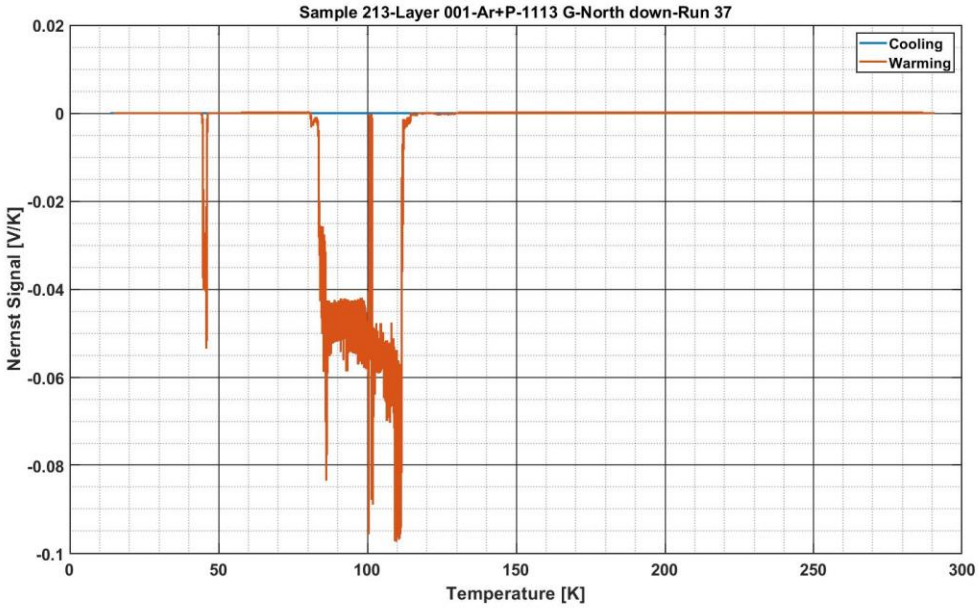
Sample 213-Layer 001-Ar+P-1113 G-North down-Run 37
Cooling
Warming
Nernst Signal [V/K]
Temperature [K]
0.02
0
-0.02
-0.04
-0.06
-0.08
-0.1
0
50
100
150
200
250
300

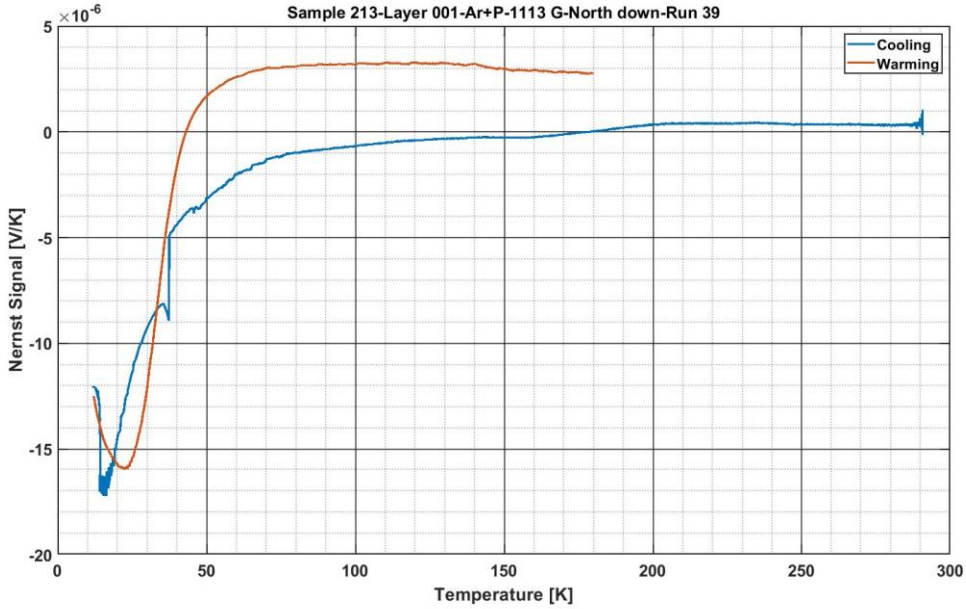
Sample 213-Layer 001-Ar+P-1113 G-North down-Run 39
×10^-6
Cooling
Warming
Nernst Signal [V/K]
Temperature [K]
5
0
-5
-10
-15
-20
0
50
100
150
200
250
300

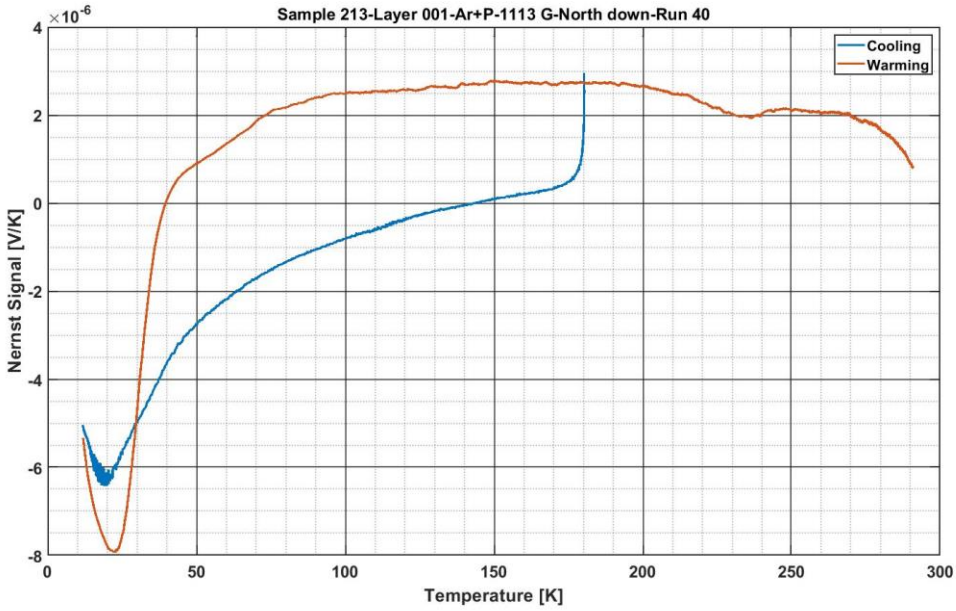
Sample 213-Layer 001-Ar+P-1113 G-North down-Run 40
×10^-6
Cooling
Warming
Nernst Signal [V/K]
Temperature [K]
4
2
0
-2
-4
-6
-8
0
50
100
150
200
250
300

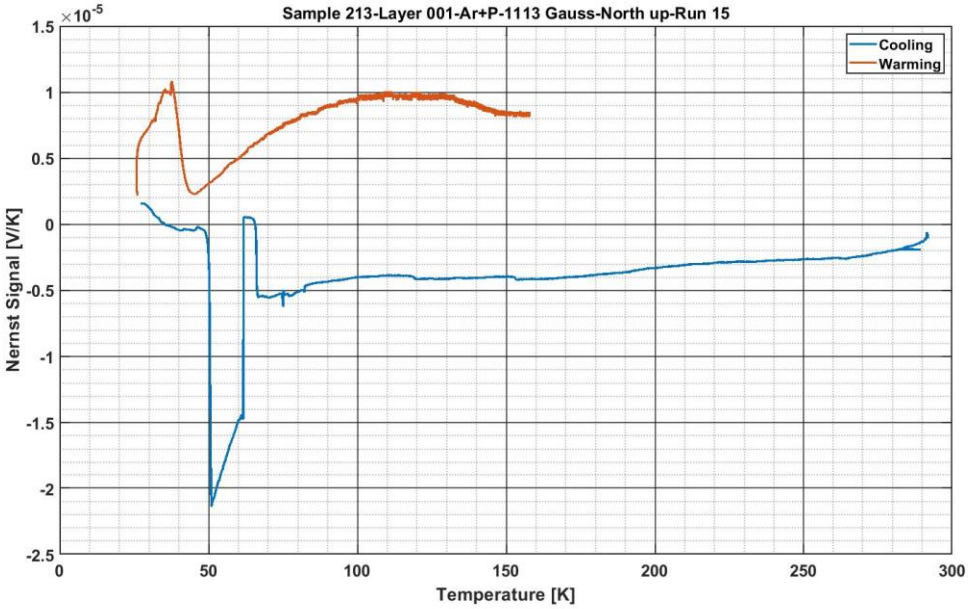
Sample 213-Layer 001-Ar+P-1113 Gauss-North up-Run 15
×10^-5
Cooling
Warming
Nernst Signal [V/K]
Temperature [K]
1.5
1
0.5
0
-0.5
-1
-1.5
-2
-2.5
0
50
100
150
200
250
300

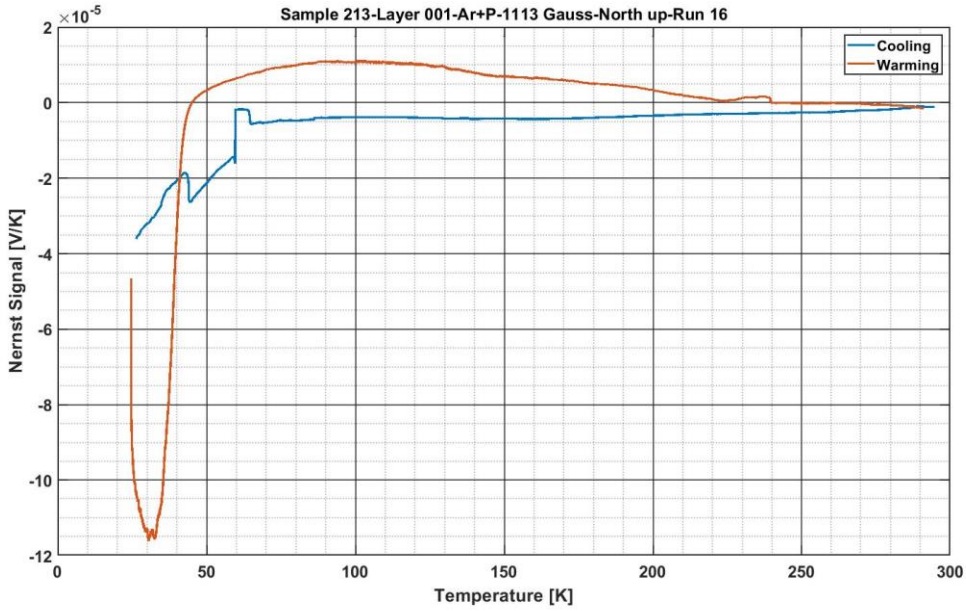
Sample 213-Layer 001-Ar+P-1113 Gauss-North up-Run 16
×10^-5
Cooling
Warming
Nernst Signal [V/K]
Temperature [K]
2
0
-2
-4
-6
-8
-10
-12
0
50
100
150
200
250
300

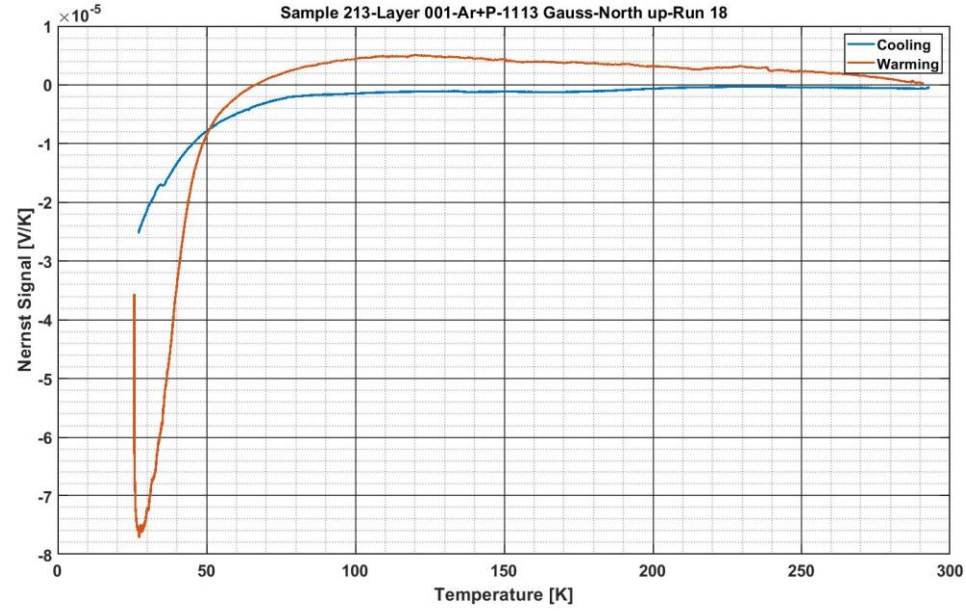
Sample 213-Layer 001-Ar+P-1113 Gauss-North up-Run 18
×10^-5
Cooling
Warming
Nernst Signal [V/K]
Temperature [K]
1
0
-1
-2
-3
-4
-5
-6
-7
-8
0
50
100
150
200
250
300

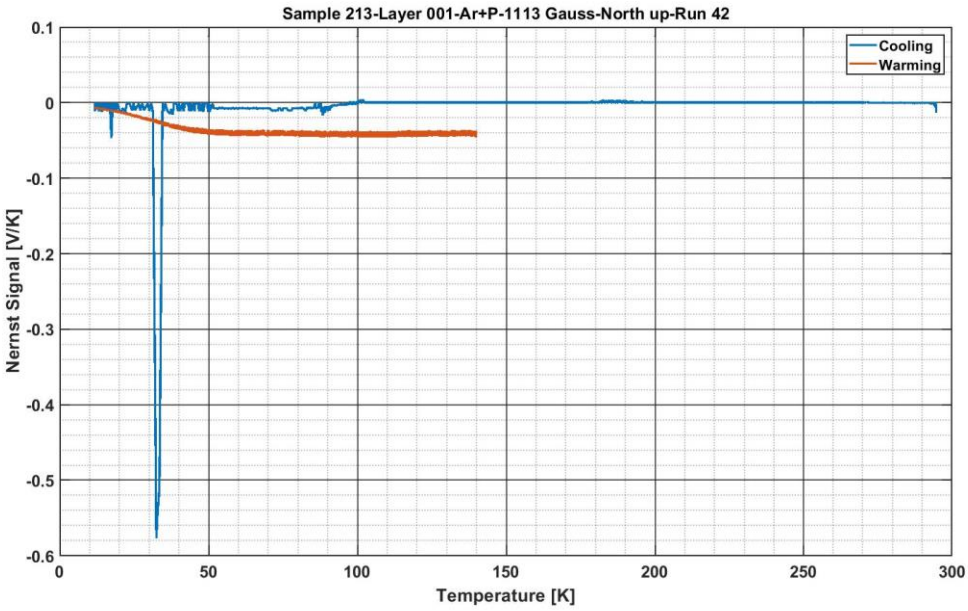
Sample 213-Layer 001-Ar+P-1113 Gauss-North up-Run 42
Cooling
Warming
Nernst Signal [V/K]
Temperature [K]
0.1
0
-0.1
-0.2
-0.3
-0.4
-0.5
-0.6
0
50
100
150
200
250
300

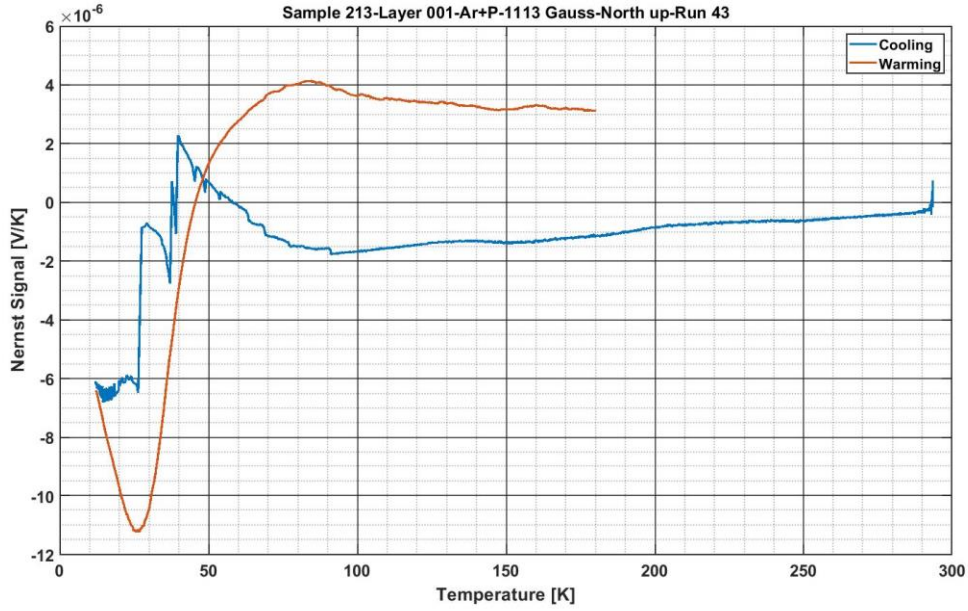
Sample 213-Layer 001-Ar+P-1113 Gauss-North up-Run 43
×10^-6
Cooling
Warming
Nernst Signal [V/K]
Temperature [K]
6
4
2
0
-2
-4
-6
-8
-10
-12
0
50
100
150
200
250
300

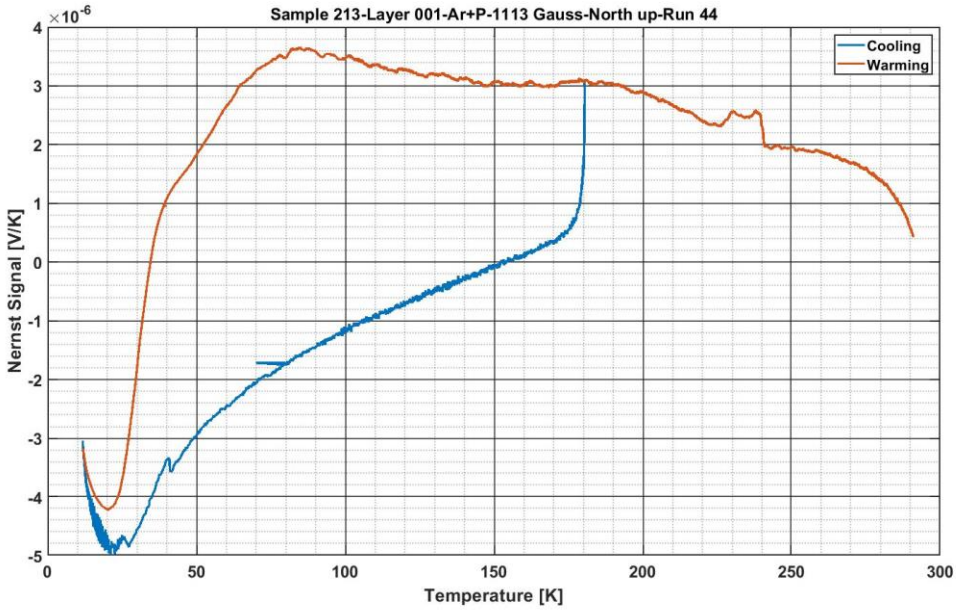
Sample 213-Layer 001-Ar+P-1113 Gauss-North up-Run 44
×10^-6
Nernst Signal [V/K]
Temperature [K]
Cooling
Warming
4
3
2
1
0
-1
-2
-3
-4
-5
0
50
100
150
200
250
300

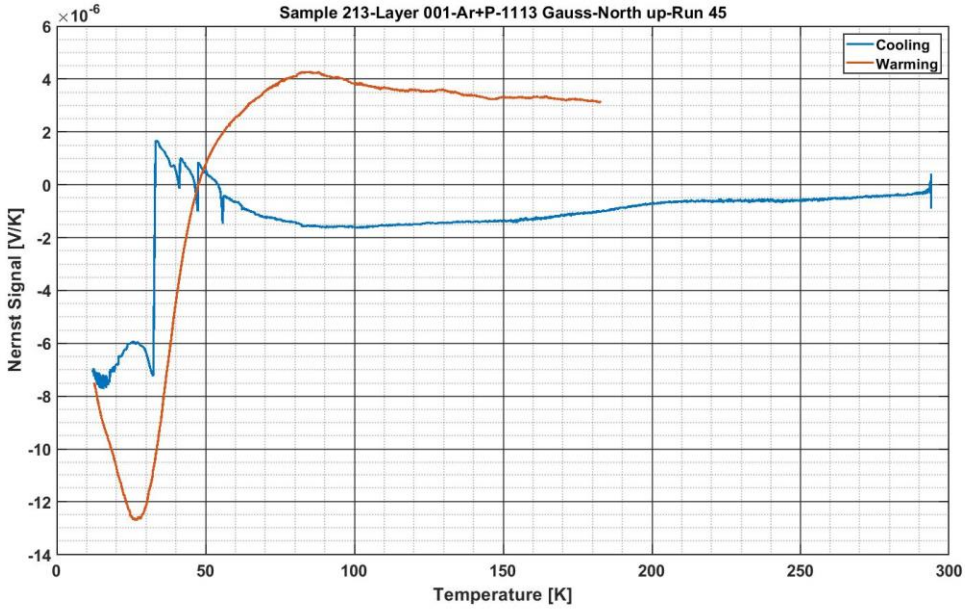
Sample 213-Layer 001-Ar+P-1113 Gauss-North up-Run 45
×10^-6
Nernst Signal [V/K]
Temperature [K]
Cooling
Warming
6
4
2
0
-2
-4
-6
-8
-10
-12
-14
0
50
100
150
200
250
300

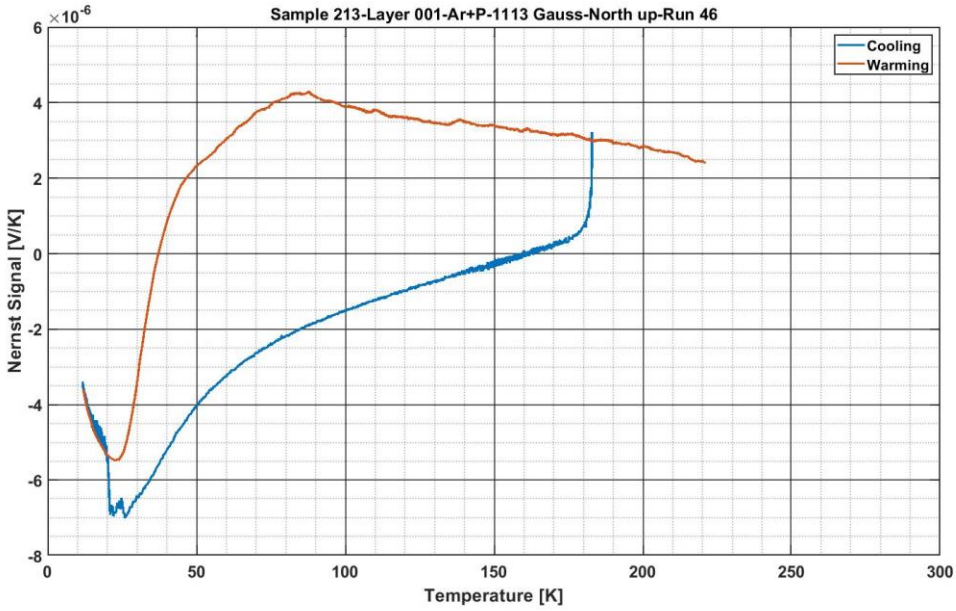
Sample 213-Layer 001-Ar+P-1113 Gauss-North up-Run 46
×10^-6
Cooling
Warming
Nernst Signal [V/K]
Temperature [K]
6
4
2
0
-2
-4
-6
-8
0
50
100
150
200
250
300

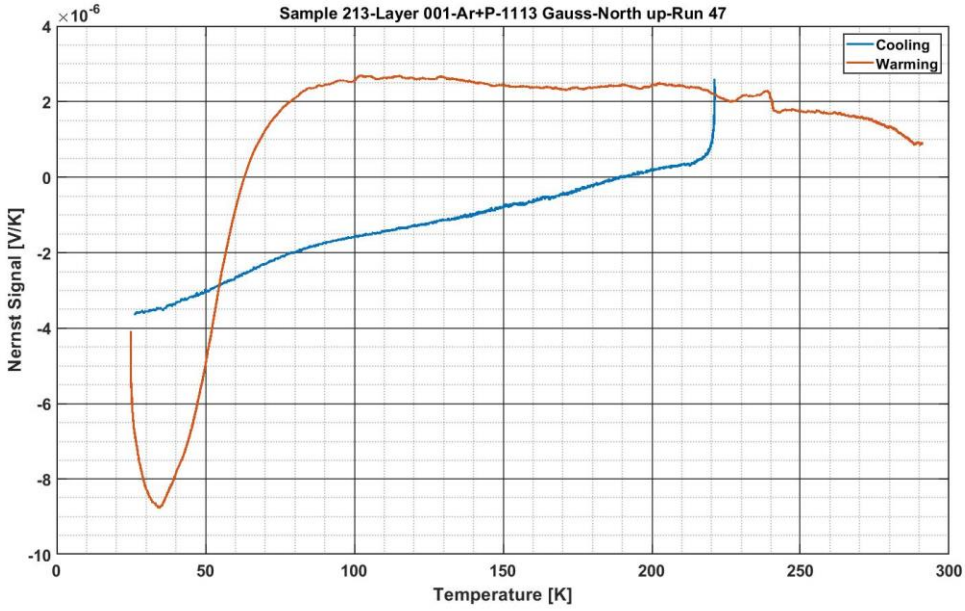
Sample 213-Layer 001-Ar+P-1113 Gauss-North up-Run 47
×10^-6
Cooling
Warming
Nernst Signal [V/K]
Temperature [K]
4
2
0
-2
-4
-6
-8
-10
0
50
100
150
200
250
300

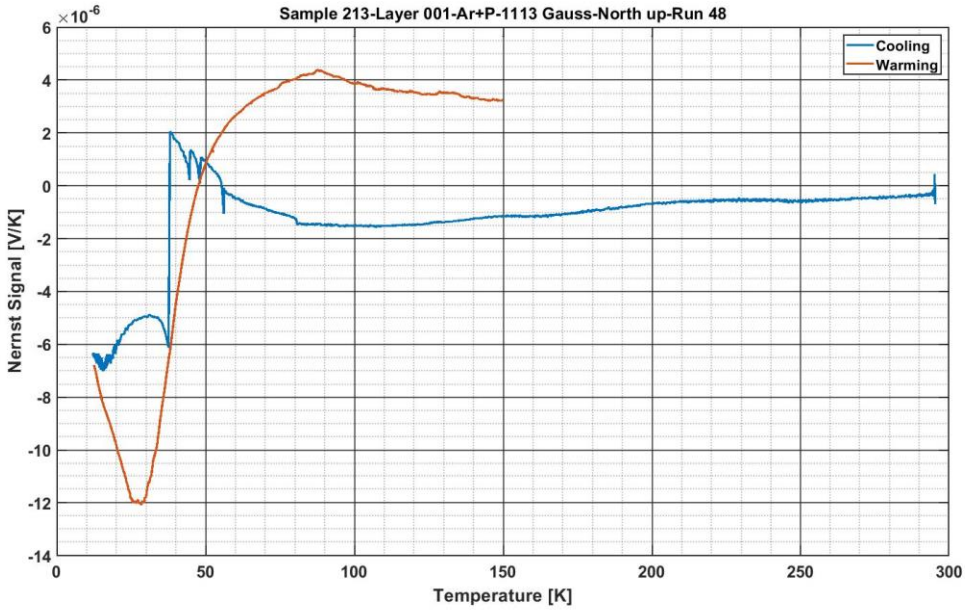
Sample 213-Layer 001-Ar+P-1113 Gauss-North up-Run 48
×10^-6
Cooling
Warming
Nernst Signal [V/K]
Temperature [K]
6
4
2
0
-2
-4
-6
-8
-10
-12
-14
0
50
100
150
200
250
300

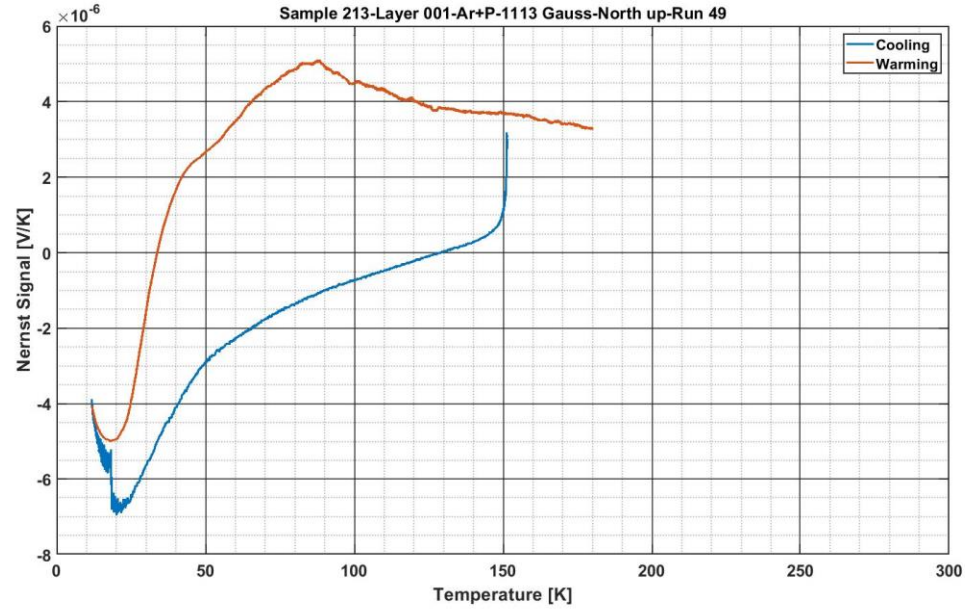
Sample 213-Layer 001-Ar+P-1113 Gauss-North up-Run 49
×10^-6
Cooling
Warming
Nernst Signal [V/K]
Temperature [K]
6
4
2
0
-2
-4
-6
-8
0
50
100
150
200
250
300

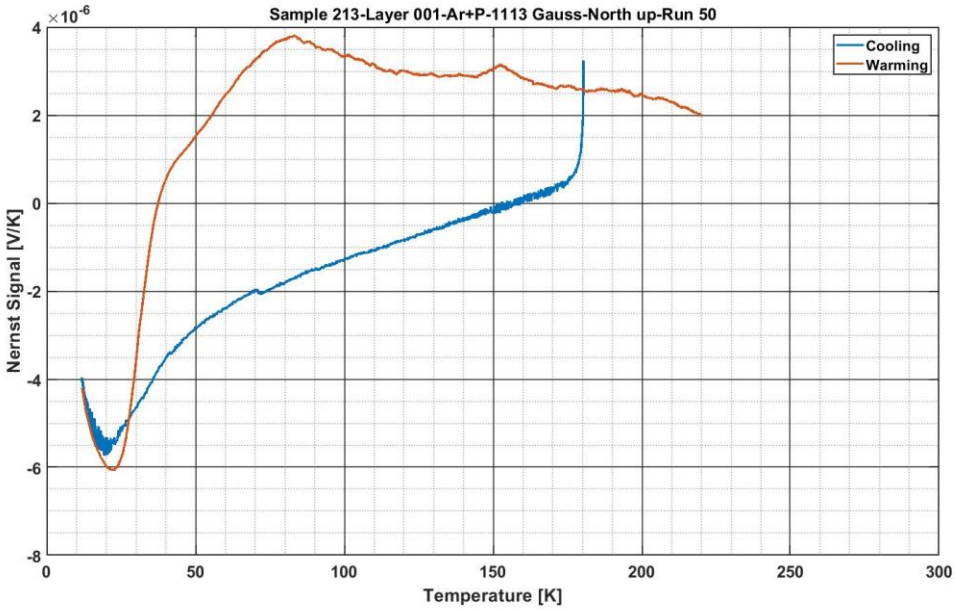
Sample 213-Layer 001-Ar+P-1113 Gauss-North up-Run 50
×10^-6
Cooling
Warming
Nernst Signal [V/K]
Temperature [K]
4
2
0
-2
-4
-6
-8
0
50
100
150
200
250
300

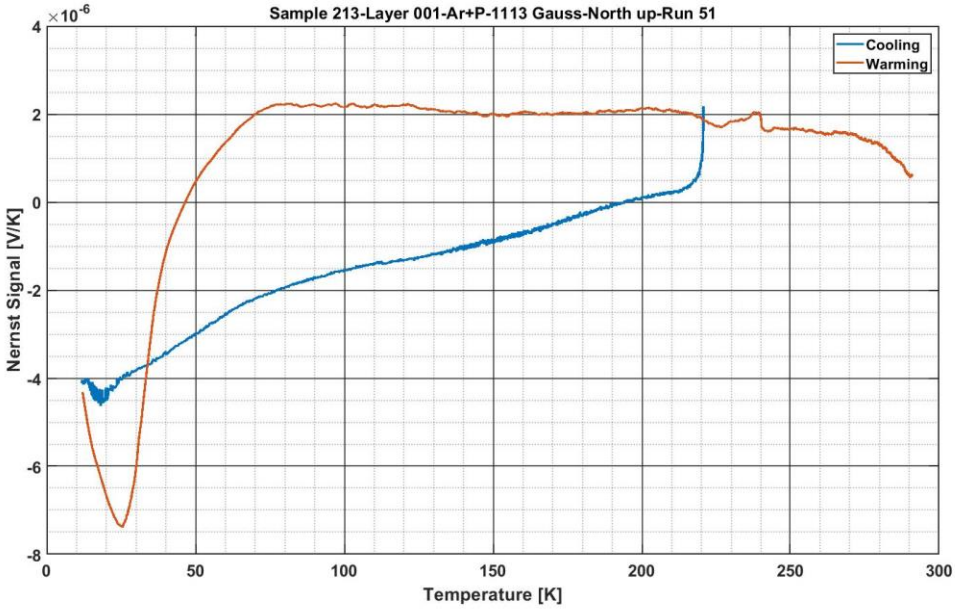
Sample 213-Layer 001-Ar+P-1113 Gauss-North up-Run 51
×10^-6
Cooling
Warming
Nernst Signal [V/K]
Temperature [K]
4
2
0
-2
-4
-6
-8
0
50
100
150
200
250
300

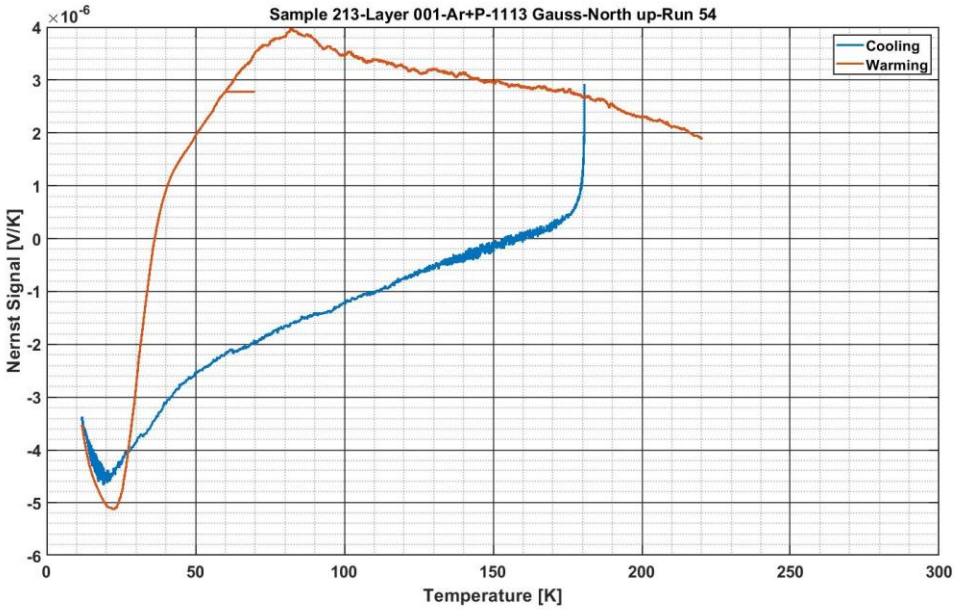
Sample 213-Layer 001-Ar+P-1113 Gauss-North up-Run 54
×10^-6
Cooling
Warming
Nernst Signal [V/K]
Temperature [K]
4
3
2
1
0
-1
-2
-3
-4
-5
-6
0
50
100
150
200
250
300

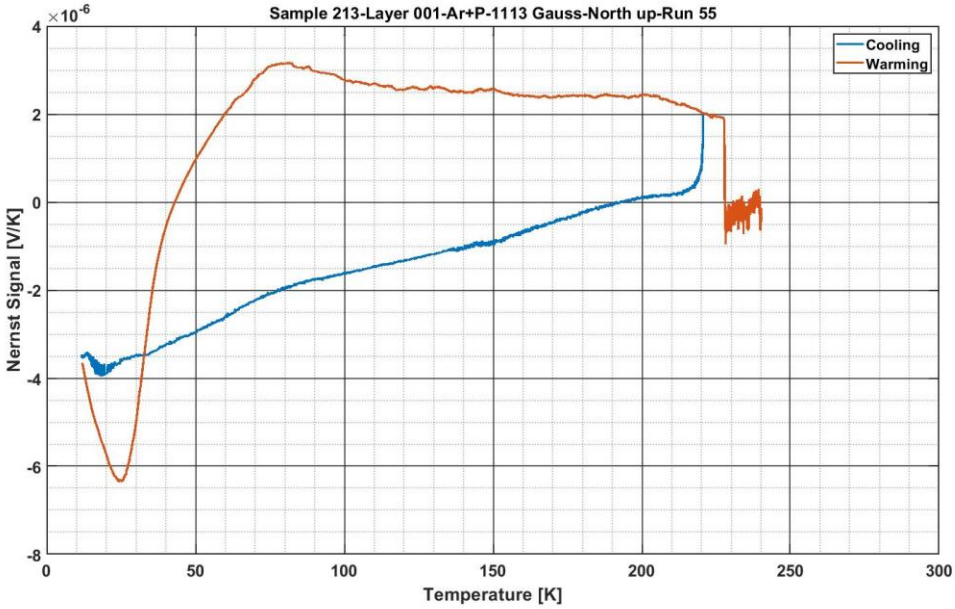
Sample 213-Layer 001-Ar+P-1113 Gauss-North up-Run 55
×10^-6
Cooling
Warming
Nernst Signal [V/K]
Temperature [K]
4
2
0
-2
-4
-6
-8
0
50
100
150
200
250
300

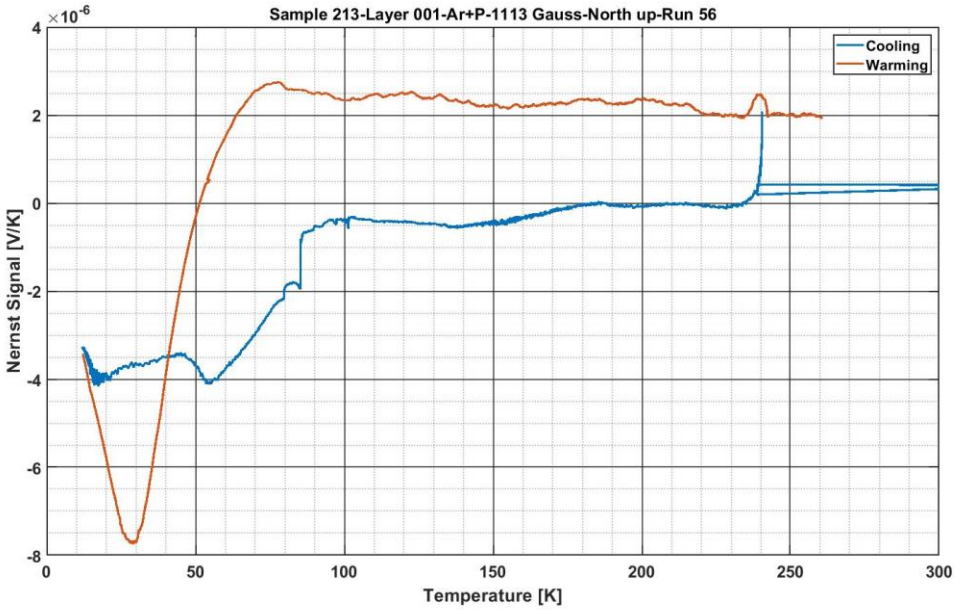
Sample 213-Layer 001-Ar+P-1113 Gauss-North up-Run 56
×10^-6
Cooling
Warming
Nernst Signal [V/K]
Temperature [K]
4
2
0
-2
-4
-6
-8
0
50
100
150
200
250
300

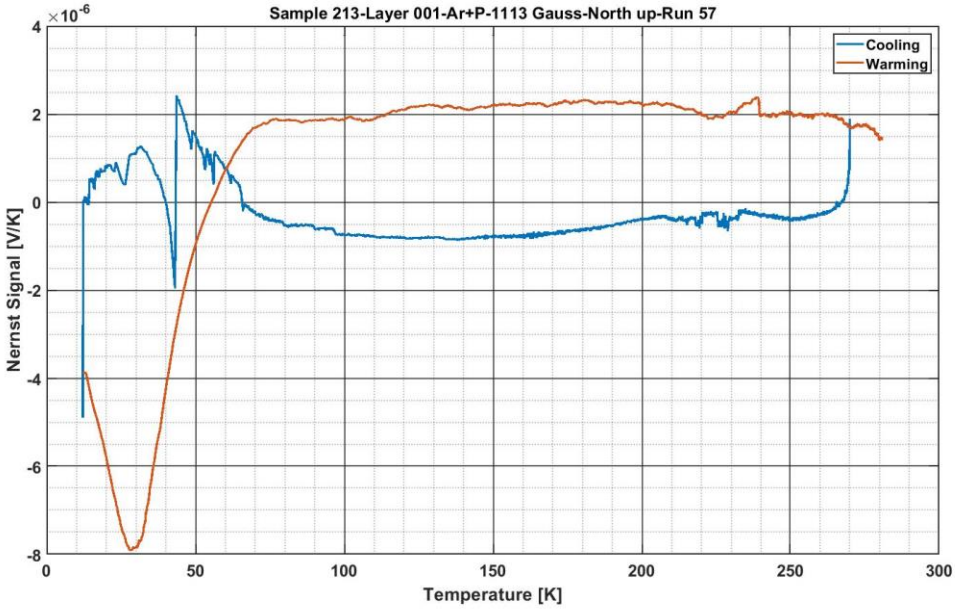
Sample 213-Layer 001-Ar+P-1113 Gauss-North up-Run 57
×10^-6
Cooling
Warming
Nernst Signal [V/K]
Temperature [K]
4
2
0
-2
-4
-6
-8
0
50
100
150
200
250
300

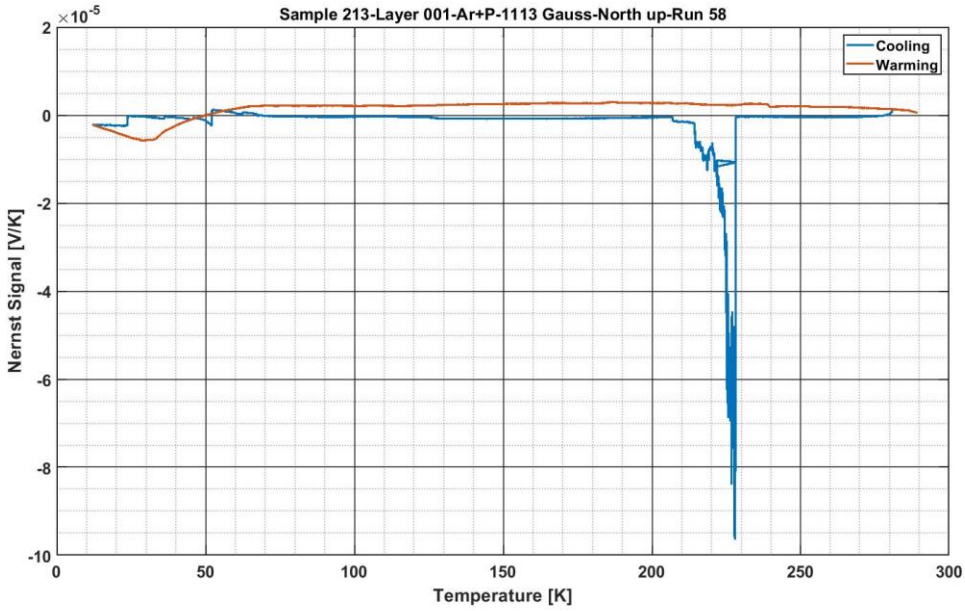
Sample 213-Layer 001-Ar+P-1113 Gauss-North up-Run 58
×10^-5
Cooling
Warming
Nernst Signal [V/K]
Temperature [K]
2
0
-2
-4
-6
-8
-10
0
50
100
150
200
250
300

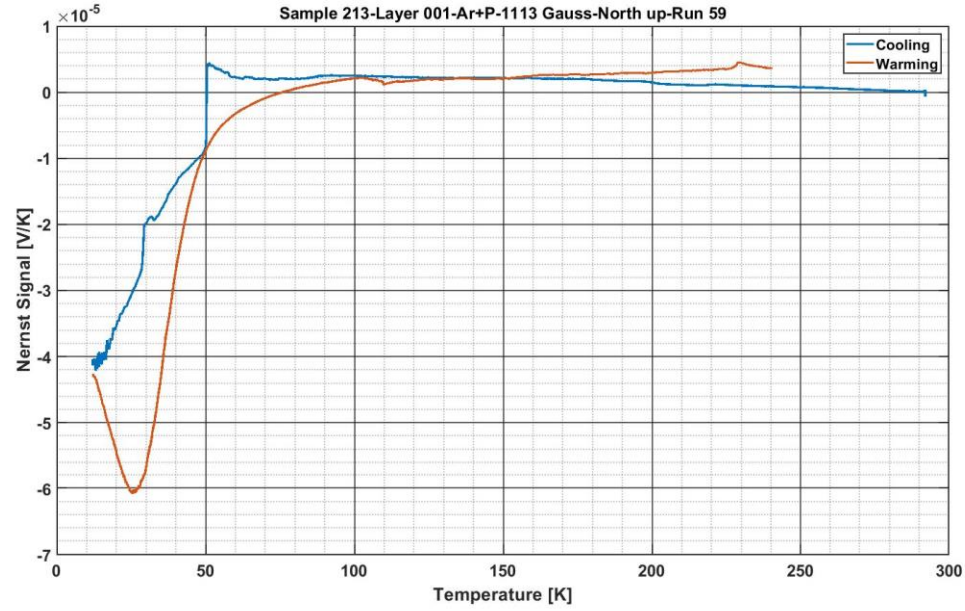
Sample 213-Layer 001-Ar+P-1113 Gauss-North up-Run 59
×10^-5
Cooling
Warming
Nernst Signal [V/K]
Temperature [K]
1
0
-1
-2
-3
-4
-5
-6
-7
0
50
100
150
200
250
300

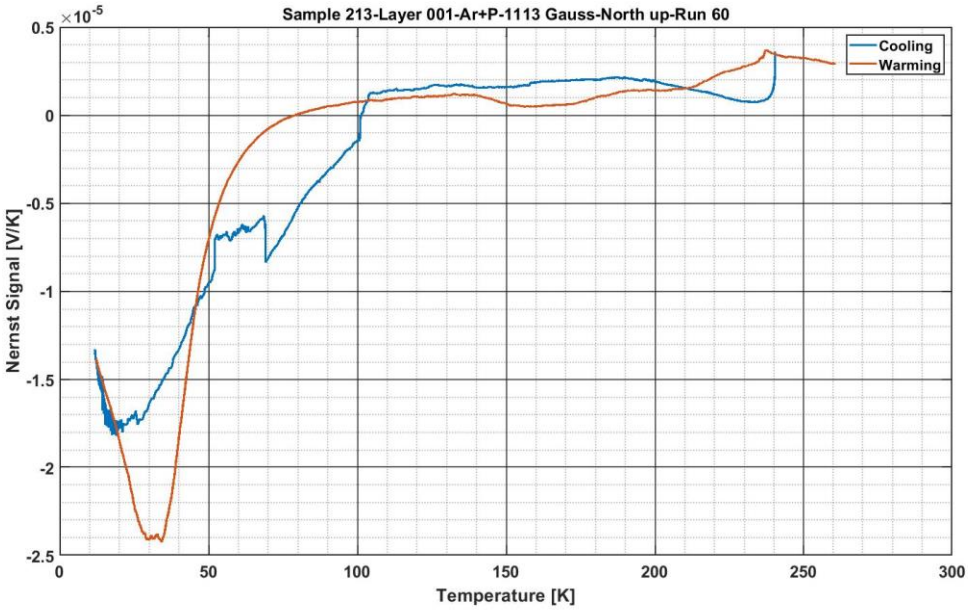
Sample 213-Layer 001-Ar+P-1113 Gauss-North up-Run 60
×10^-5
Cooling
Warming
Nernst Signal [V/K]
Temperature [K]
0.5
0
-0.5
-1
-1.5
-2
-2.5
0
50
100
150
200
250
300

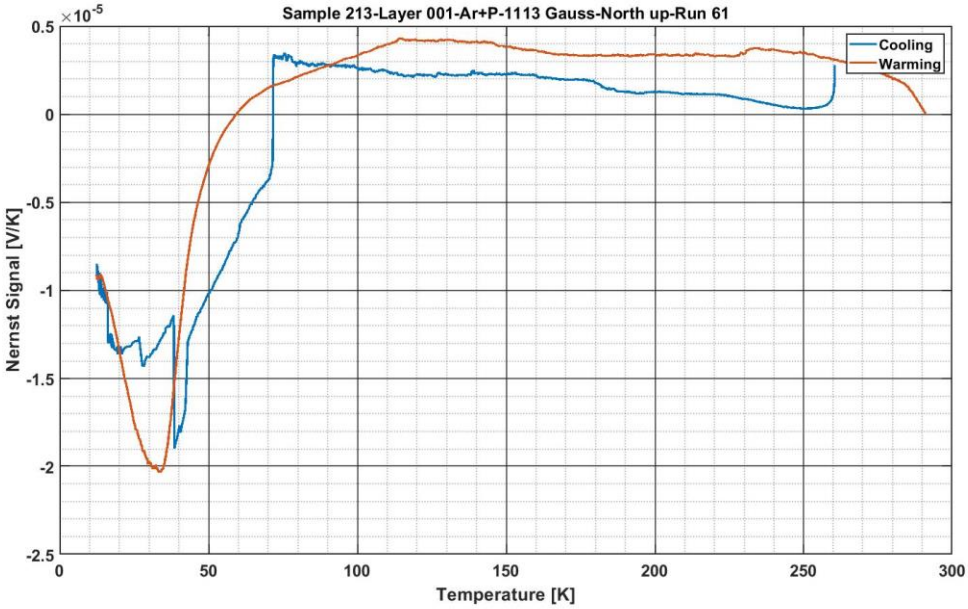
Sample 213-Layer 001-Ar+P-1113 Gauss-North up-Run 61
×10^-5
Cooling
Warming
Nernst Signal [V/K]
Temperature [K]
0.5
0
-0.5
-1
-1.5
-2
-2.5
0
50
100
150
200
250
300

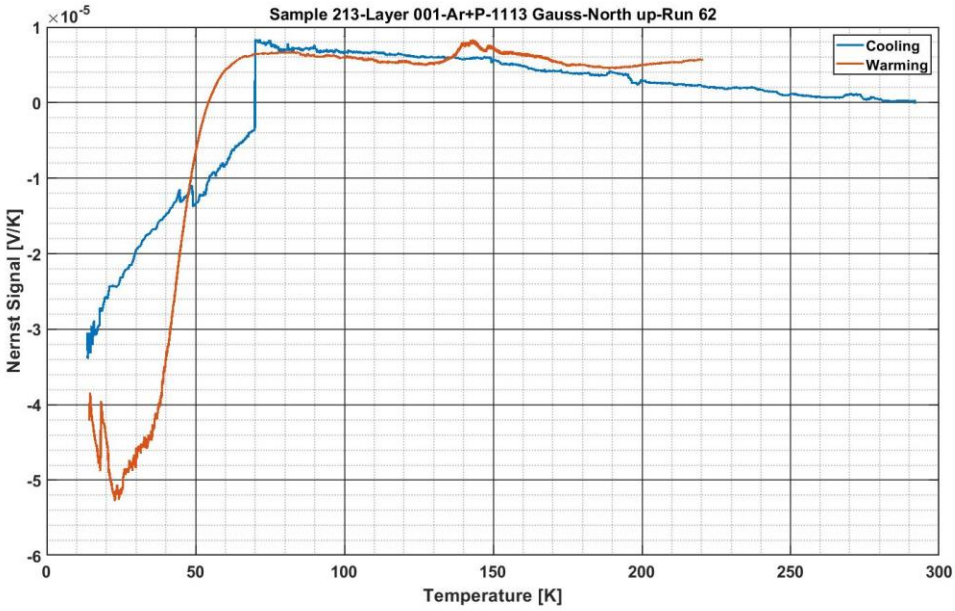
Sample 213-Layer 001-Ar+P-1113 Gauss-North up-Run 62
×10^-5
Cooling
Warming
Nernst Signal [V/K]
Temperature [K]
1
0
-1
-2
-3
-4
-5
-6
0
50
100
150
200
250
300

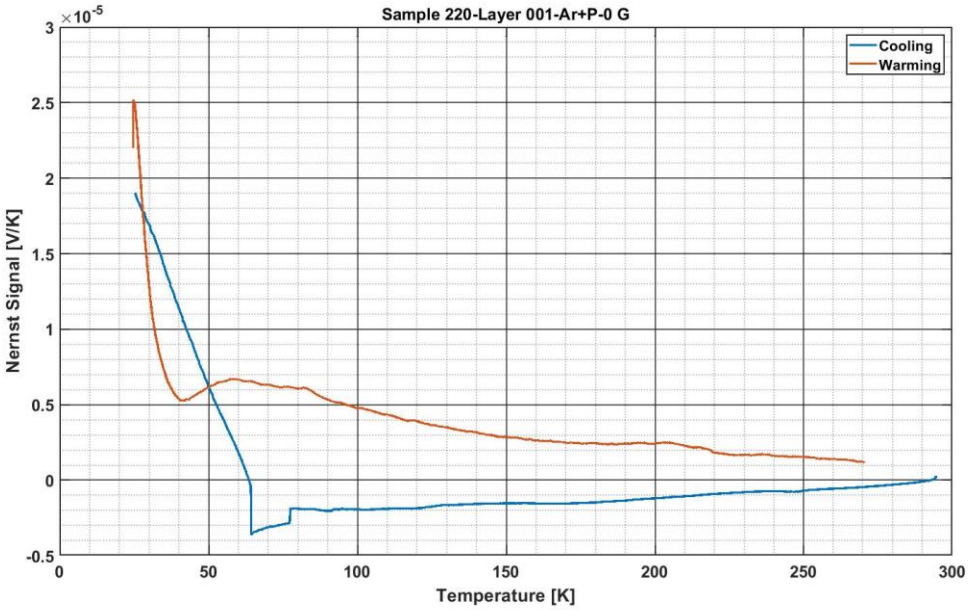
Sample 220-Layer 001-Ar+P-0 G
×10^-5
Cooling
Warming
Nernst Signal [V/K]
Temperature [K]
3
2.5
2
1.5
1
0.5
0
-0.5
0
50
100
150
200
250
300

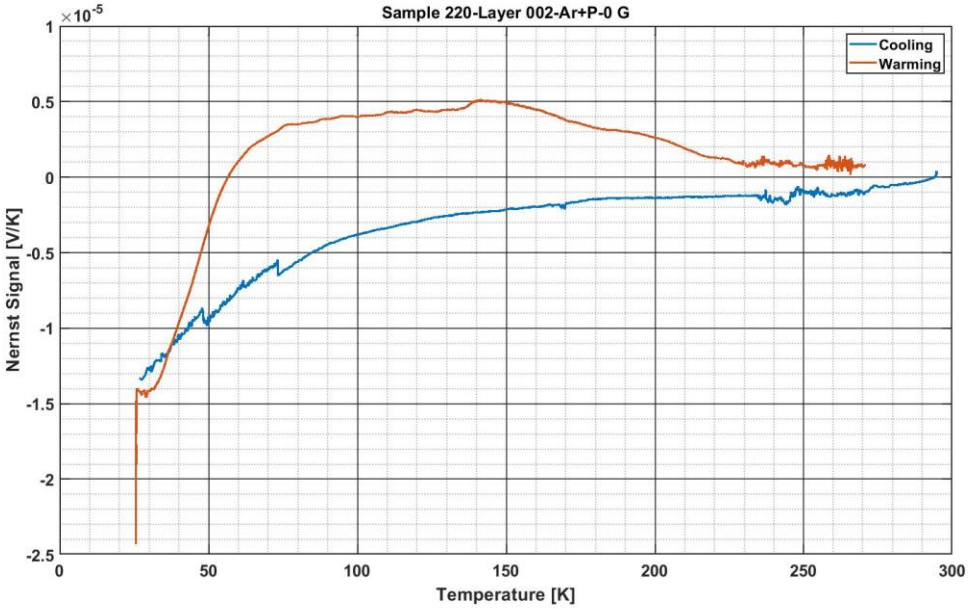
Sample 220-Layer 002-Ar+P-0 G
×10^-5
Cooling
Warming
Nernst Signal [V/K]
Temperature [K]
1
0.5
0
-0.5
-1
-1.5
-2
-2.5
0
50
100
150
200
250
300

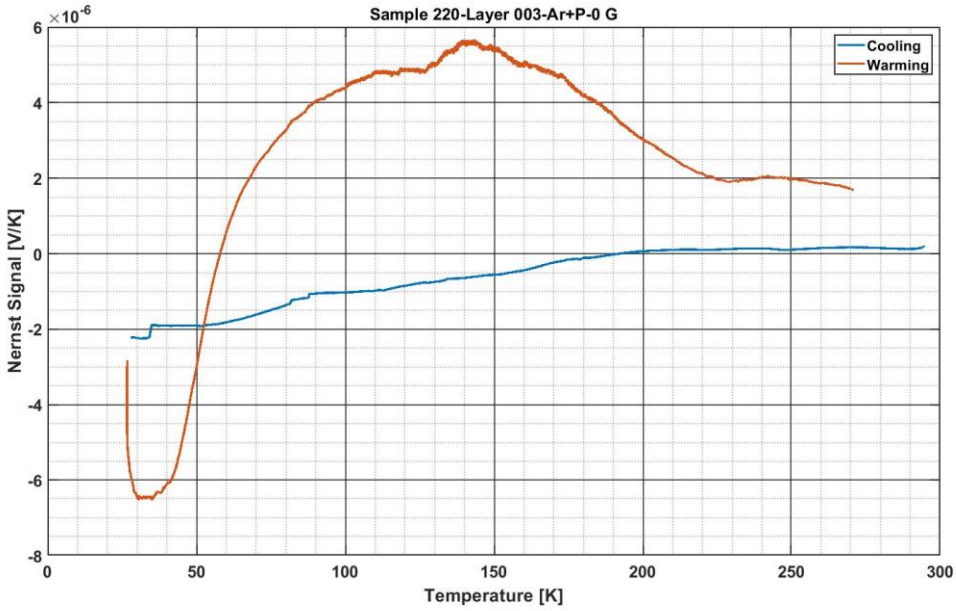
Sample 220-Layer 003-Ar+P-0 G
×10^-6
Cooling
Warming
Nernst Signal [V/K]
Temperature [K]
6
4
2
0
-2
-4
-6
-8
0
50
100
150
200
250
300

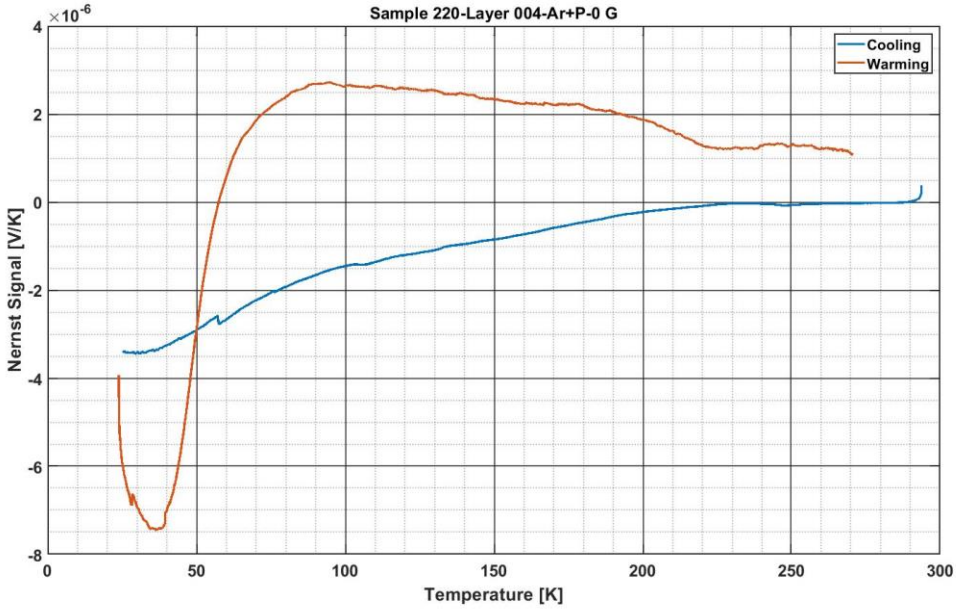
Sample 220-Layer 004-Ar+P-0 G
×10^-6
Cooling
Warming
Nernst Signal [V/K]
Temperature [K]
4
2
0
-2
-4
-6
-8
0
50
100
150
200
250
300

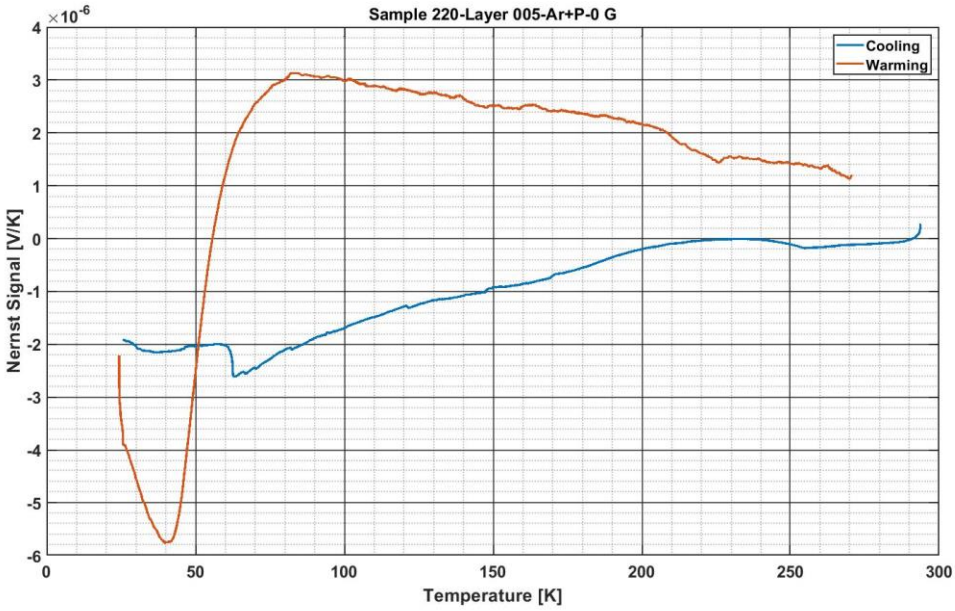
Sample 220-Layer 005-Ar+P-0 G
×10^-6
Nernst Signal [V/K]
Temperature [K]
Cooling
Warming
4
3
2
1
0
-1
-2
-3
-4
-5
-6
0
50
100
150
200
250
300

VITA

JULIAN ESTEBAN GIL PINZON

Born, Bogota, Colombia

2014-2016	B.S., Electrical Engineering Florida International University Miami, Florida
2017-2018	M.S., Electrical Engineering Florida International University Miami, Florida
2018 -2021	Ph.D., Electrical and Computer Engineering Florida International University Miami, Florida

PUBLICATIONS AND PRESENTATIONS

Sornkhampan N., Gil-Pinzon J., Ponce-Zuniga J., Woods A., Vlasov Y., Larkins G., (2021). *Evidence of vortices and mixed-state superconductivity in phosphorus-doped graphene. Part I (Nernst).* Superconductor Science and Technology 34 035022

Gil-Pinzon J., Sornkhampan N., Woods A., Vlasov Y., Larkins G., (2021). *Evidence of vortices and mixed-state superconductivity in phosphorus-doped graphene. Part II (Hysteresis).* Superconductor Science and Technology 34 035023

.